Monte Carlo Radiative Transfer in Accretion Disk Winds of Cataclysmic Variable Stars

Dissertation
zur Erlangung des Grades eines
Doktors der Naturwissenschaften
der Fakultät für Mathematik und Physik
der Eberhard-Karls-Universität Tübingen

vorgelegt von

Daniel-Jens Kusterer

aus Stuttgart
2008

Selbstverlegt von: D.-J. Kusterer
Hohewartstr.27A
70469 Stuttgart

Tag der mündlichen Prüfung: 16.06.2008

Dekan: Prof. Dr. N. Schopohl

1. Berichterstatter: Prof. Dr. K. Werner
2. Berichterstatter: Prof. Dr. W. Kley

Erweiterte deutsche Zusammenfassung

Daniel-Jens Kusterer

Monte Carlo Strahlungstransport in Akkretionsscheibenwinden von Kataklysmischen Variablen

Akkretion ist ein weitverbreiteter Prozess im Universum, der von aktiven Galaxienkernen (AGN) bis hin zu sehr jungen Sternen (sog. young stellar objects (YSO)) auftritt. Dennoch sind viele Aspekte dieses Prozesses und die Physik der damit zusammenhängenden Akkretionsscheiben noch nicht gut verstanden. Ein vorzügliches Beispiel in dieser Richtung ist der sogenannte „Wind“, der von leuchtkräftigen Scheiben abströmt. Die Beobachtung zeigt sehr klare Hinweise auf einen solchen Wind, jedoch sind weder der genaue Mechanismus, welcher diesen Wind treibt, noch die daraus resultierenden Massenverlustraten bis jetzt vollständing verstanden und erklärbar. Ideale Objekte um dieses Phänomen genauer zu studieren sind Kataklysmische Variable Sterne (CV). Bei diesen handelt es sich um enge Doppelsterne, die aus einem Weissen Zwerg als Primärstern und einem Roten Zwerg als Sekundärstern bestehen, wobei Masse vom Sekundärstern auf den Primärstern überfliesst. Verglichen mit der hohen Energieabstrahlung in AGN und der eher geringen Abstrahlung in YSOs sind CVs auf der mittleren Energieskala anzusiedeln und haben den klaren Vorteil der guten Beobachtbarkeit.

Im Rahmen dieser Arbeit werden erst CVs und die mit ihnen verbundenen Phänomene, welche von der Natur dieser Objekte als akkretionsgetrieben herrühren, eingeführt. Insbesondere sind die sog. Zwergnovae, in deren Ausbrüchen sich die Leuchtkraft der Akkretionsscheibe dramatisch erhöht, wichtig. In einem solchen Ausbruch, so zeigen Beobachtungen, ist die Scheibe in der Lage, Gas in einem Akkretionsscheibenwind von ihrer Oberfläche zu treiben. Der Wind ist aller Wahrscheinlichkeit nach strahlungsgetrieben vergleichbar dem Wind von O-Sternen. Die Signaturen, die ein solcher Wind in den Beobachtungen hinterlässt, hauptsächlich sog. P Cygni Linienprofile, sind im Ausbruch derart ausgeprägt, dass ein Modell, welches einen kompletten CV im Ausbruch beschreiben soll, auf jeden Fall den Akkretionsscheibenwind beinhalten muss. In der Tübinger Sternatmosphärengruppe existieren bereits Strahlungstransportmodelle für den Weissen Zwerg und die Akkretionsscheibe. Diese werden in Zukunft durch den Strahlungstransport durch den Wind ergänzt wie er in dieser Arbeit entwickelt wird. Für die Beschreibung des Strahlungstransportes ist, im Gegensatz zum Strahlungstransport in der Akkretionsscheibe für die ein eindimensionales Modell ausreicht, ein dreidi-

mensionales Modell erforderlich. Aus diesem Grund wird der Strahlungstransport im Wind mit einer Monte Carlo Methode implementiert, bei der Photonen, die ihren Ursprung in der Scheibe oder dem Weissen Zwerg haben, durch das dreidimensionale Modell des Windes propagiert werden. Als Vergleich und Referenz implementieren wir die schon existierenden Beschreibungen von Shlosman & Vitello (1993) und Knigge et al. (1995) eines Scheibenwindes, bevor wir dann unser eigenes Modell basierend auf den hydrodynamischen Rechnungen von Feldmeier & Shlosman (1999) entwickeln. Die Ergebnisse für diese Standardmodelle werden dann untereinander und mit Ergebnissen für diese Modelle aus einem bereits existierenden Code verglichen. Nach diesem Codetest rechnen wir Modelle für real existierende Sternsysteme. Die Zwergnovae SS Cygni und Z Camelopardalis werden ebenso betrachtet wie das spezielle Helium-Zwergnovasystem AM Canum Venaticorum. Allerdings werden keine intensiven Parameterstudien betrieben, daher sind nur erste Abschätzungen für Systemparameter zu gewinnen. Für AM CVn lässt sich abschätzen, dass Massenverlustraten höher als $1 \cdot 10^{-9} \mathrm{M}_{\odot}/\mathrm{yr}$ und sogar bis zu $5 \cdot 10^{-9} \mathrm{M}_{\odot}/\mathrm{yr}$ möglich sind. Eine genauere Einschränkung der Inklination über den Literaturwert hinaus ist nicht möglich. Es wird ein realistisches Akkretionsscheibenmodell als Grundlage für die Photonengenerierung benutzt. Die Kombination aus Akkretionsscheibe und Akkretionsscheibenwind ergibt eine gute Beschreibung der Beobachtung. P Cygni Profile, z.B. N V 1240 Å, werden von unseren Windmodellen wiedergegeben. Andererseits werden Linien, die hauptsächlich in der Scheibe entstehen, wie Ly α, in Windmodellen mit einer Schwarzkörperscheibe als Grundlage nicht wiedergegeben. In dieser Arbeit wird ein solches Schwarzkörperscheibenmodell für Z Cam verwendet. In diesem Fall werden dann nur Windlinien zur Analyse verwendet, allerdings führen die Ergebnisse für N V und C IV zu unterschiedlichen Ergebnissen für Z Cam. Daher können weder der Inklinationswinkel noch die Massenverlustrate genauer eingeschränkt werden. Allerdings scheint eine Massenverlustrate zwischen $1 \cdot 10^{-10} \mathrm{M}_{\odot}/\mathrm{yr}$ und $5 \cdot 10^{-10} \mathrm{M}_{\odot}/\mathrm{yr}$ möglich, wobei der abgeleitete Inklinationswinkel von der Massenverlustrate abhängt. Da wir für unser drittes System, SS Cyg, nur einen sehr eingeschränkten Parameterraum betrachten, lässt sich lediglich sagen, dass ein Inklinationswinkel von 32° für eine Massenverlustrate von $4.4 \cdot 10^{-10} \mathrm{M}_{\odot}/\mathrm{yr}$ am wahrscheinlichsten ist.

Im Rahmen von Akkretionsscheibenwinden ist es mit dieser Arbeit zum ersten Mal möglich, sowohl Doppler- als auch Stark-Verbreiterung in der Berechnung der Linienopazitäten anzunehmen. Wir erhalten als Ergebnis, dass die Dopplerverbreiterung, so wie sie bisher üblicherweise verwendet wurde, zu geringe Massenverlustraten ergibt.

Abstract

Daniel-Jens Kusterer

Monte Carlo Radiative Transfer in Accretion Disk Winds of Cataclysmic Variable Stars

Accretion is a very common and important process in the universe from powerful active galactic nuclei (AGN) to young stellar objects (YSO). Yet many aspects of accretion and the physics of the accretion disks involved in the process are not fully understood. A prime example is the “wind” driven off a luminous accretion disk, clear signatures of its presence are seen in observations, however neither the driving mechanism nor the resulting mass loss rates are determined in a satisfying manner. Ideal objects for a closer analysis of the accretion phenomenon are so called cataclysmic variable stars (CV). These are close binary systems formed by a white dwarf primary and a red dwarf secondary with mass flow from the Roche lobe filling secondary onto the primary. Compared to the high energies involved in AGN and the rather low energy output of YSOs, CVs are in the intermediate energy range and they also have the clear advantage of being easily observable.

In this work we first introduce CVs and the phenomena observed in these systems which are connected to their nature as accretion powered objects. Especially important for our work is the so-called dwarf nova phenomenon where the accretion disk increases its brightness dramatically. In such a high state observations show that the disk is able to drive gas off in an accretion disk wind presumably by radiative driving as in winds of O stars. The observable signatures of an outflow, mostly so-called P Cygni profiles, are, in outburst situations, this prominent that a model which aims to describe the complete CV system necessarily has to include such an outflow. The Tübingen group had up till now working radiative transfer models for white dwarfs and accretion disks and these are supplemented by a radiative transfer model for an accretion disk wind developed in this work. A three-dimensional description of the wind and of the radiative transfer in the wind is necessary compared to the disk where a one-dimensional approximation can be used. Therefore a Monte Carlo radiative transfer method is implemented where photon packets from the disk and from the white dwarf are transported through a three-dimensional model of an accretion disk wind. For comparison and reference we implemented the two kinematical disk wind models of Shlosman & Vitello (1993) and of Knigge et al. (1995), before we develop our own model based on the hydrodynamical calculations of Feldmeier & Shlosman (1999). Results for standard implementations of these models are compared to each other and to the results of an already existing code. After this verification of our code we step further and calculate models for real systems. The dwarf novae SS Cygni and Z Camelopardalis as well as the special helium dwarf nova AM Canum Venaticorum are considered. No intensive parameter studies are performed, but first impressions for possible mass-loss rates and inclination angles of the systems are found. For AM CVn we can conclude that a mass-loss rate of higher than $1 \cdot 10^{-9}\mathrm{M}_{\odot}/\mathrm{yr}$, even as high as $5 \cdot 10^{-9}\mathrm{M}_{\odot}/\mathrm{yr}$ is probable, but a further refinement of the inclination angle beyond the literature value is not possible. Our calculations use a realistic accretion disk model as input for photons, the combination of accretion disk and wind yield, especially for AM CVn in this work, a very good description of observations. P Cygni profiles, e.g. N V 1240 Å, are resembled with our wind models, but are not present in disk only models. On the other hand lines originating in the disk, e.g. Ly α, are not resembled by a wind model with a blackbody accretion disk as photon input, which we used for Z Cam. Here only wind lines can be considered and the results from N V and C IV are inconclusive, where neither the mass-loss rate nor the inclination angle can be narrowed with any definiteness, but mass-loss rates between $1.1 \cdot 10^{-10}\mathrm{M}_{\odot}/\mathrm{yr}$ and $5.1 \cdot 10^{-10}\mathrm{M}_{\odot}/\mathrm{yr}$ seem possible, with the resulting inclination angle depending on the mass-loss rate. Our very limited set of parameters used in the calculations for SS Cyg does not allow us to refine the inclination or mass-loss of the system any more as compared to the literature values, however an inclination close to 32° seems most likely for a mass-loss rate of $\dot{M} = 4.44 \cdot 10^{-10}\mathrm{M}_{\odot}/\mathrm{yr}$.

For the first time in radiative transfer codes for accretion disk wind we have the possibility to use Stark or Doppler broadening functions and we find that Doppler broadening might underestimate the mass-loss rates. For the real systems and comparisons with observations we find first constraints on mass-loss rates, but are not able to improve estimations for the inclination angles further than they are already known.

To my parents

To Katrin

Contents

1 Introductory thoughts **1**
- 1.1 Structure 5

2 Cataclysmic Variable Stars **6**
- 2.1 Overview 6
- 2.2 Components of a CV via light curve decomposition 8
- 2.3 Roche Geometry 11
- 2.4 Mass transfer and accretion disk 13
  - 2.4.1 Magnetic CVs 18
- 2.5 Evolution of cataclysmic variables 22
- 2.6 AM CVn stars 25
- Cataclysmic Variables - summary 27

3 Disks, outflow and dwarf novae **28**
- 3.1 Accretion disks – a more theoretical introduction 28
- 3.2 The α-disk model 33
- 3.3 Spectral signatures of accretion disks 35
  - 3.3.1 Origin of emission and absorption lines 35
  - 3.3.2 Double peaked lines 36
- 3.4 Dwarf novae 37
  - 3.4.1 Outburst mechanism 39
- 3.5 Outflow in cataclysmic variable systems 48
  - 3.5.1 Spectral signatures of outflows 48
  - 3.5.2 Observational evidence of outflows in CVs 49
- 3.6 Hydrodynamics of accretion disk winds 51
  - 3.6.1 The line force 52
  - 3.6.2 Flow nozzle analogy 56
  - 3.6.3 Critical point of Euler equation 57
  - 3.6.4 Nozzle function for g_s and F_s of a disk wind 60
- Disk, Outflow and Dwarf Novae – summary 63

4 Techniques **64**
4.1 Radiative transfer 64
4.1.1 The radiation field 64
4.1.2 Transfer equations 66
4.1.3 Opacity and emissivity 67
4.1.4 Occupation numbers 68
4.1.5 Remarks on LTE 69
4.1.6 Opacities in moving media 69
4.2 Wind Models 71
4.2.1 Shlosman & Vitello Model 71
4.2.2 Knigge, Woods & Drew Model 76
4.2.3 Hydrodynamical wind model 81
4.2.4 Radiation sources 82
4.3 Monte Carlo methods 84
4.3.1 General definitions 84
4.3.2 Radiative transfer in a Monte Carlo context 86
4.3.3 Monte Carlo radiative transfer in this work 87
4.4 Code 89
4.4.1 WOMPAT - the code flow overview 89
4.4.2 Monte Carlo radiation field estimators and temperatures 92
4.4.3 Comparison with existing codes 93
Techniques – summary 99

5 Results **101**
5.1 The standard models 101
5.1.1 Comparison of densities 101
5.1.2 Standard SV model 105
5.1.3 Standard hydrodynamical model 111
5.1.4 Standard KWD model 114
5.2 AM Canum Venaticorum 116
5.3 SS Cygni 121
5.4 Z Camelopardalis 125

6 Conclusions **130**

A Constants and other mathematical symbols used **133**

B Abbreviations used **134**

List of figures **134**

List of tables 136

Bibliography 138

Index 144

Curriculum vitae 150

CHAPTER 1

Introductory thoughts

“All that we see or seem
is but a dream within a dream”
[Edgar Allan Poe]

Space – still the final frontier. Anyone who has ever been watching a dark night sky with all those bright dots and maybe a glance of the milky way probably wondered what is out there. What are those bright dots and how are they working? How would it be to travel out there?

We have not even explored all of our backyard, the solar system, but we have a good clue how it looks like out there on the larger scales. It is a vast emptiness dominated by the weakest of the four fundamental forces – gravity. Only where matter clumps under the influence of gravity the really interesting and bright phenomena start. Clouds of gas and dust, stars, black holes, galaxies are all created by clumping matter. A massive clump forms a so called gravitational well, a low point in the local gravitational potential. Further matter falls ”down” that gravitational well, a process called accretion. It is abundant in the universe, found from protostellar clouds collapsing and forming young stellar objects (YSO) to interacting binaries and on to active galactic nuclei (AGN) making it a very important process to understand in detail. Accretion is not only important because of its abundance in the universe, but also because of the high luminosity of accretion powered objects.
Where does this high luminosity come from? The answer is twofold. Mass falling towards the center of the gravitational well needs to obey angular momentum conservation, it can only be transported further down the well if angular momentum is somehow transported up the well. This transport is done via friction and the matter spreads out into a disk. It works very much like the swirl when water flows out of a bathtub. The disk is one part of the answer.

Its large surface area leads to a large output of light. Part two of the answer is the source of the energy radiated away. Gravitational potential energy is converted into heat and radiation via friction as the matter falls further down the gravitational well. This is one of the most effective processes for generating radiation in the universe.

But if we take a closer look at such an accretion powered object it turns out that not all of the matter falling down the gravitational well actually finds its way to the center of the well. A part of the matter is driven off – by some processes not yet fully understood – and forms an outflow. Such an outflow manifests itself in the form of a jet or an accretion disk wind or in both forms. YSOs and AGN are known to have jets as well as wind outflows. In some of these objects the jets can even be resolved with imaging telescopes. Three especially nice examples of YSOs with jets, so called Herbig-Haro objects, are shown in Fig. 1.1, one YSO with a dust disk and disk wind like outflow in Fig. 1.2. On the other end of the energy scale you find AGN which also show

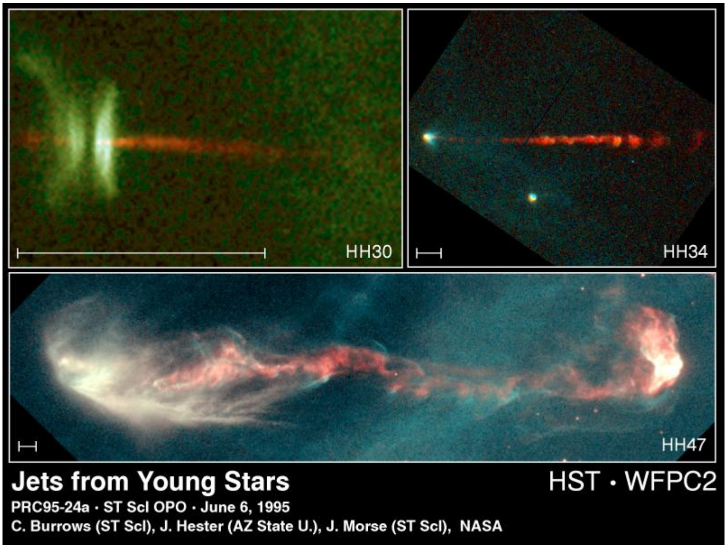
HH30
HH34
HH47
Jets from Young Stars
HST • WFPC2
PRC95-24a • ST ScI OPO • June 6, 1995
C. Burrows (ST ScI), J. Hester (AZ State U.), J. Morse (ST ScI), NASA

Figure 1.1: HST/WFPC2 images of three Herbig-Haro objects. The scale for each image represents 10^3 AU[2].

---

[2] One astronomical unit (AU) is the mean distance earth - sun. Find explanations and values for this and other units and symbols used throughout this work in the appendix.

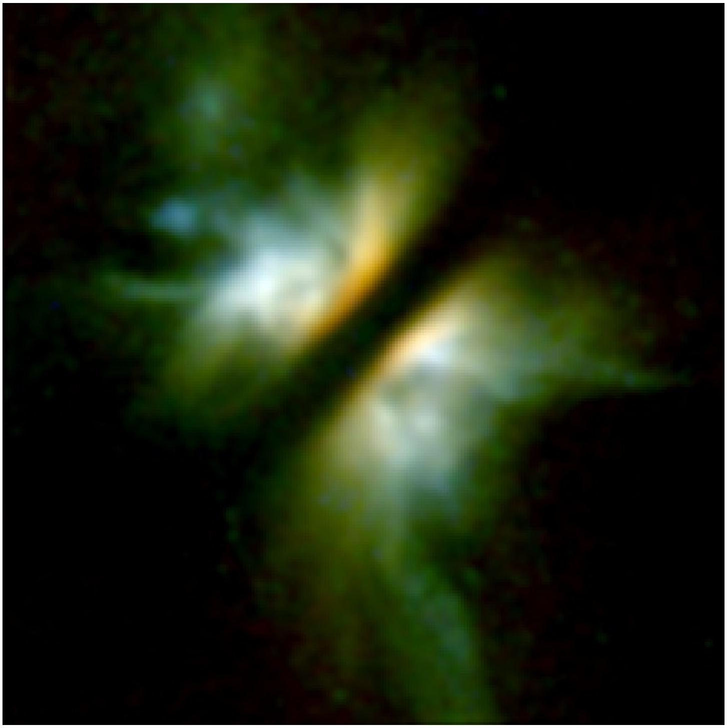

Figure 1.2: HST/NICMOS image of IRAS 04302+2247. The object itself is hidden behind a dust disk, but a bipolar outflow structure is clearly visible.

outflows. A remarkable example is the Hubble Space Telescope (HST) image of Messier 87, a giant elliptical galaxy in the close-by Virgo galaxy cluster, shown in Fig. 1.3. The jet of this active galaxy is more than 5.000 lightyears in length. Interestingly cataclysmic variable stars (CVs), which are accretion powered objects in the intermediate energy range and are more closely described in chapter 2, do not show jets, but they show disk wind like outflows. Nevertheless CVs are ideal objects to study the accretion phenomenon in greater detail. They are a lot closer than AGN and not as obscured as many YSOs. With this in mind it becomes clearer that cataclysmic variable stars are one of the best laboratories for accretion physics we have available.

The Tübingen optical/UV group therefore has the goal to develop a whole simulation package for cataclysmic variables which is targeted to enhance our

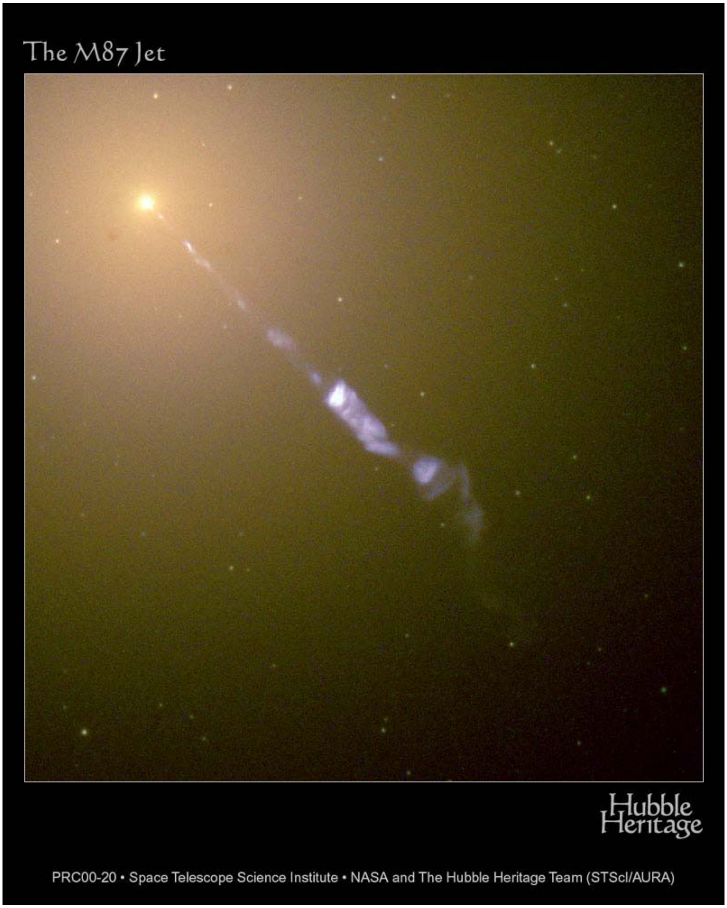
The M87 Jet
Hubble Heritage
PRC00-20 • Space Telescope Science Institute • NASA and The Hubble Heritage Team (STScI/AURA)

Figure 1.3: HST image of M87 shows one of the most prominent jets.

understanding of accretion powered objects. Based on the Tübingen Model Atmosphere Package (TMAP, Werner et al. 2003) the accretion disk code AcDc was developed by Nagel et al. (2004) and successfully used to model accretion disk spectra (e.g. Werner et al. 2006). So far only the accretion disk and the white dwarf but not the outflow from the disk can be modeled. To overcome this limitation is the aim of the work presented here.

1.1 Structure

This work is organised as follows. In the next section the accretion physics laboratories used in this work, namely cataclysmic variables, are introduced. A more thorough theoretical introduction into accretion physics itself is then given in chapter 3, where we show theoretical models of accretion disks and hydrodynamical calculations of the outflow. Chapter 4 is then used to lay the technical basis of this work by explaining radiative transfer in general, as well as in a Monte Carlo context. The wind models and the code developed for this work are also presented in this chapter. Finally we present our results and conclusions in chapters 5 and 6.

CHAPTER 2

Cataclysmic Variable Stars

"Poets say science takes away from the beauty of the stars - mere globs of gas atoms. I, too, can see the stars on a desert night, and feel them. But do I see less or more?"

[Richard P. Feynman]

In this chapter we present an introduction to cataclysmic variables and to phenomena associated with these objects. It is mainly based on the comprehensive textbooks of Hellier (2001) and Warner (1995).

2.1 Overview

Let us take a closer look at what cataclysmic variable stars are. As the name suggests, they are highly variable, changing their brightness in an unpredictable manner often by factors of tens to hundreds within a matter of minutes to hours. This variability is due to the accretion powered nature of these objects. CVs are close binary stars, so close indeed, that there is mass flow from one star to the other. Actually this mass overflow together with the unpredictable outbursts is the reason for the name cataclysmic. It descends from the greek noun κατακλυσμὸς which translates as *flooding* or *catastrophe*. The two partners in the binary are a white dwarf and a late type main sequence star. Such late type main sequence stars are also known as red dwarfs, as they are reddish in colour and have a mass much lower than one solar mass. The white dwarf is more massive than the red dwarf and is therefore called primary (star) and quantities for it are denoted by a subscript 1. Consequently the red dwarf is called secondary (star) and is denoted by a subscript 2.

Variability of CVs can be put into two categories. Regular and predictable variability due to the orbital motion of the binary star components and irregular, unpredictable variability. The latter one being due to the mass overflow and the nature of CVs as accretion powered objects. How the former can help us in understanding those objects will be demonstrated in the next section. Matter accreted onto the white dwarf surface can reach a critical density at which the hydrogen in this accreted surface layer starts a fusion process – a thermonuclear runaway sets in. This triggers a so called *nova* eruption. A rapid and huge rise in luminosity ($\Delta m = 6 \ldots 19\,\mathrm{mag}$ or up to 10^5 solar luminosities ($\mathrm{L}_\odot$)) happens. Lasting between 10 and 100 days and followed by a steady decline in brightness during the following months the eruption sheds the outer shell off the white dwarf. Roughly one thousand days after the eruption the shell becomes visible as a ring like nebula. Distinctions are made between *classical novae* for which only one such eruption has been observed and the slightly fainter ($\Delta m = 6 \ldots 9\,\mathrm{mag}$) *recurrent novae* for which at least two outbursts have been observed. Recurrence times in these cases are of the order of decades and correlate with the eruption brightness. The mechanism for classical novae and recurrent novae is the same, therefore all novae might be recurrent. Only with the recurrence times for classical novae being much larger than the lifespan of an average astronomer.

A second type of irregular variability are *dwarf novae outbursts* with a smaller increase in brightness of $\Delta m = 2 \ldots 6\,\mathrm{mag}$ or a factor of 100. Those outbursts typically last a few days with quiescence periods of a few tens to several hundred days in-between. Contrary to the nova outburst mechanism a dwarf nova outburst is not a thermonuclear explosion, but the increase in luminosity is due to an increased mass flux through the disk. As all the additional luminosity of a dwarf nova in outburst originates from the accretion disk it becomes increasingly important to model and understand the disk properly. Only then the whole dwarf nova picture will reveal itself. There is another important phenomenon connected to a luminous disk, an outflow of gas, a so called disk wind, is triggered by such a disk. A detailed discussion of dwarf novae follows in Sec. 3.4.

The class of *nova-like systems* consists of all the CVs that do not show eruptions. Spectroscopic similar to novae they are commonly explained as pre- or post-novae systems. Some of these systems might be the long sought supernova Ia progenitors. A type Ia supernova occurs when a white dwarf is pushed over the Chandrasekhar limit of $1.4\,\mathrm{M}_\odot$. Electron Fermi pressure, which normally balances the gravitational pressure in a white dwarf, cannot withstand gravity anymore, a thermonuclear runaway sets in. A huge explosion disrupts the whole white dwarf releasing an energy of about $10^{51}\mathrm{erg}$. In a CV enough mass to push the white dwarf over the Chandrasekhar limit can only be accumulated at certain conditions. A steady supply of hydrogen rich material through the disk for the white dwarf's outer shell with a rate that can sustain hydrogen burning in that shell is ideal. In this case a violent eruption as in a nova does not occur, instead the ashes of the hydrogen burning accumulate and can bring the white dwarf over the Chandrasekhar limit. If there is no steady burning in the outer shell of the white dwarf, the hydrogen accumulates until there is enough to trigger a nova eruption. A nova then ejects roughly the same or even slightly more mass into space than has been accumulated on the white dwarf previously. Therefore the nova-like scenario with just the right mass transfer rate is able to serve as a type Ia supernova progenitor.

2.2 Components of a CV via light curve decomposition

Let us come back to the structure and components of a cataclysmic variable system. They can be deduced from lightcurve analysis of eclipsing CVs. One nice example is Z Cha, for which a classical lightcurve analysis was done by Wood et al. (1986). A mean lightcurve with data from 17 eclipses folded into one orbital period is shown in Fig. 2.1. The orbital period for this system is found to be $P_{\mathrm{orb}} \approx 107\,\mathrm{min}$. Remember now the law by Johannes Kepler, that the orbital period is related to the orbital radius. The shorter the period, the smaller the radius. Comparing the 107 minutes orbital period of Z Cha with an orbital period of one year for the earth's orbit around the sun, or with the 88 days orbit of Mercury it becomes obvious that Z Cha must be a very compact system. With Kepler's law

$$P_{\mathrm{orb}}^2 = \frac{4\pi^2 a^3}{G(M_1 + M_2)} \tag{2.1}$$

one can calculate a binary separation a. In the case of Z Cha, assuming a white dwarf primary with $M_1 = 0.85\,\mathrm{M}_\odot$, where $\mathrm{M}_\odot$ is the solar mass, and a secondary with $M_2 = 0.15\,\mathrm{M}_\odot$, both of which are plausible values, a separation $a \approx 5.1 \cdot 10^8\,\mathrm{m}$ is obtained. This is less than the solar radius $\mathrm{R}_\odot = 7 \cdot 10^8\,\mathrm{m}$. The whole Z Cha system would fit into the sun.

Besides the short period the second obvious feature of the lightcurve is the very sharp and deep eclipse marking phase 0 in Fig. 2.1. Obviously the main

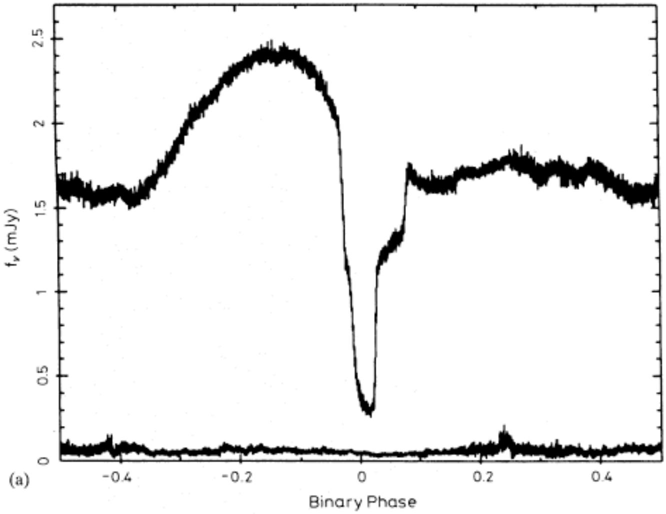

Figure 2.1: Mean lightcurve of Z Cha in quiescence. Data from 17 eclipses folded into one orbital phase. Taken from Wood et al. (1986).

part of the system's light must come from a compact object. With the knowledge of the orbital velocity the size of the compact object can be calculated out of the time it takes to come in and out of the eclipse. The size is roughly that of the earth. A bright object with such a size can only be a white dwarf. A white dwarf is the burnt out core of a star at the end of its life consisting only of the ashes from the burning cycles throughout the star's life. White dwarfs cannot be more massive than the Chandrasekhar limit, $1.4\,\mathrm{M}_\odot$, and are generally found in mass ranges from 0.3 to $1.3\,\mathrm{M}_\odot$. Although in a white dwarf no more active burning is happening and it is only cooling down, it still can have a high temperature depending on its age. Very young white dwarfs can reach surface temperatures of about 100,000 K. The most common temperatures for white dwarfs in CV systems are found to be in the range of 13,500 to 50,000 K, which is higher than the median for field white dwarfs of 10,000 K (Warner, 1995).

The mean lightcurve can be decomposed to gain more insight into the components of the CV system Z Cha. Such a decomposition is shown in Fig. 2.2. In much the same way as the size of the primary can be deduced from the rise and fall times of the eclipse, the size of the secondary can be deduced from the duration of the eclipse. It is found that the secondary has a radius of roughly 15 to 20 percent of a solar radius. A very small star, but still a lot larger than the white dwarf. Because of its faintness and size the only conclusion is that it has to be a red dwarf. Due to the low mass fusion processes in a red dwarf take place at a slower rate compared to more massive stars. The rate is only about a thousandth that of the sun. Consequently the surface temperature of a red dwarf is only a few thousand K ($\sim$ 2,500 K) compared to the 5,800 K of the sun's surface. True to its name the red dwarf's low surface temperature gives the star a red appearance. Only in the redder and infrared parts of the spectrum contributions of the red dwarf are expected. Intense radiation from the white dwarf, however, blasts the side of the red dwarf facing the white dwarf and can lead to a significant increase in the surface temperature of this side. A slight hump feature in the lightcurve when the heated side is seen is the consequence.

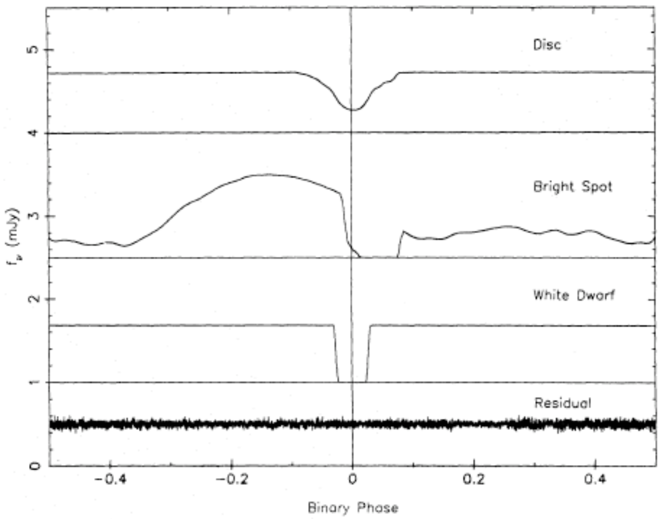

Figure 2.2: Decomposition of mean lightcurve from Fig. 2.1. Offsets are for better distinguishability, but zero levels are shown for each component. For orientation, the fluxes of the white dwarf and the disk are about equal, the mean of the bright spot flux is about half that. Taken from Wood et al. (1986).

Two other components are shown in Fig. 2.2. Both are due to mass flowing from the secondary to the primary. Why and how this mass overflow happens will be explained in more detail in the following sections, but a few words about the lightcurve features right away. The uppermost panel of Fig. 2.2 shows the disk component of the system. It is not completely eclipsed, a fact that leads to the conclusion that the disk is larger than the secondary. When more material flows from the red dwarf into the gravitational well of the white dwarf it has to hit the material already accumulated in the disk at some place. This place is called the bright spot because a large part of the kinetic energy of the material stream is converted into heat and radiated away brightening the impact spot. The movement of the bright spot gives rise to the hump like feature of the lightcurve called orbital hump. It gets brighter as it moves towards the observer and dimmer as it moves away. Due to its relatively small size the bright spot gets completely covered by the secondary. A closer look reveals that it is slightly larger in size as the white dwarf, but – of course – smaller than the accretion disk.

2.3 Roche Geometry

A lone, non-rotating, star is just spherical, pulled into this most compact configuration by gravity. If two stars are close together, however, there is also the gravitational pull of the two stars, which distorts the “normal” spherical shape of the stars. In order to gain more insight why this is happening, why and how the mass flow works, we have to look at the gravitational potential of a close binary system. The two components orbit their common center of mass with the angular velocity

$$\vec{\omega} = \sqrt{\frac{G(M_1 + M_2)}{a^3}} \cdot \vec{e_z} \, . \tag{2.2}$$

For simplicity the assumptions of circular orbits and point masses for M_1 and M_2 are taken. One can then follow the route of Edouard Roche, a 19th century French astronomer, and write down the gravitational potential ϕ which a test particle with negligible mass at position $\vec{r}$ in a co-rotating coordinate system feels:

$$\phi = -\frac{GM_1}{|\vec{r} - \vec{r_1}|} - \frac{GM_2}{|\vec{r} - \vec{r_2}|} - \frac{1}{2} \left(\vec{\omega} \times \vec{r}\right)^2 \, . \tag{2.3}$$

It consists of the potentials of the two stars located at $\vec{r_1}$ and $\vec{r_2}$ and a term due to the centrifugal force. Some equipotential surfaces are plotted in Fig. 2.3. Close to the stars the surfaces are separated and circular in shape only to get distorted towards one another until they touch at the so called inner Lagrange point (L_1). The shapes for the two surfaces touching the point L_1 are called *Roche lobes*. In binary systems these are especially important, because if

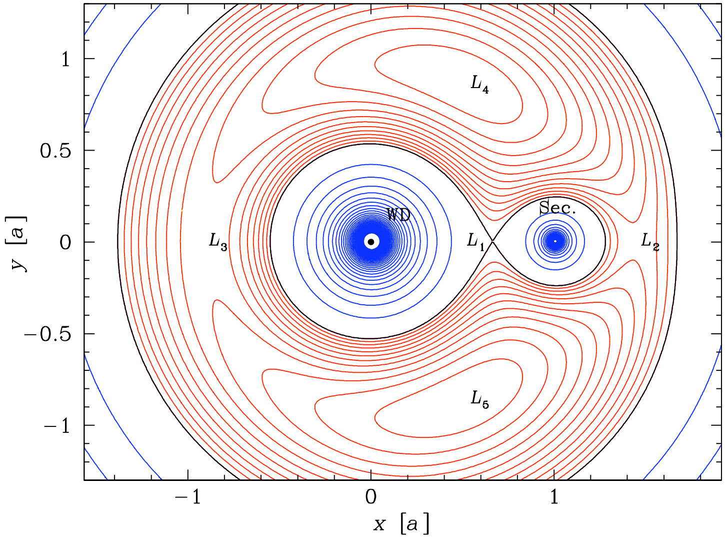

Figure 2.3: Equipotential contours of the Roche potential in a binary system. Note that the Roche lobe of the more massive star is the larger one. White dwarf (WD) and secondary (Sec.) are marked, as well as the Lagrange points of the system. Taken from Kube (2002).

one partner fills its Roche lobe mass transfer sets in. To stay in the picture of a gravitational well one can think of the two lobes as two lakes with a ridge between them. If the upper lake fills up to the ridge, water starts to flow down into the lower lying lake. A cartoon of this is shown in Fig. 2.4. An interesting point to note is that the shape of the Roche lobe is solely determined by the mass ratio $q = M_2/M_1$ of the two components. Whereas the scale of the lobes is set by the size of the orbit.

If one partner fills its Roche lobe and mass is transfered, the system is called semi-detached binary. Stable mass flow is only possible if $q < 1$, in other words if the secondary fills its Roche lobe, otherwise a runaway effect would occur. More details about this below in Sec. 2.5. All CVs are such systems with stable mass flow. The case where none of the two stars fills its Roche lobe is called a detached binary system, where NN Ser is a prime example. If both components fill their lobes the system is called a contact binary, examples would here be the W UMa stars. Even more extreme is the case where the Roche lobe is overfilled and the secondary orbits inside the

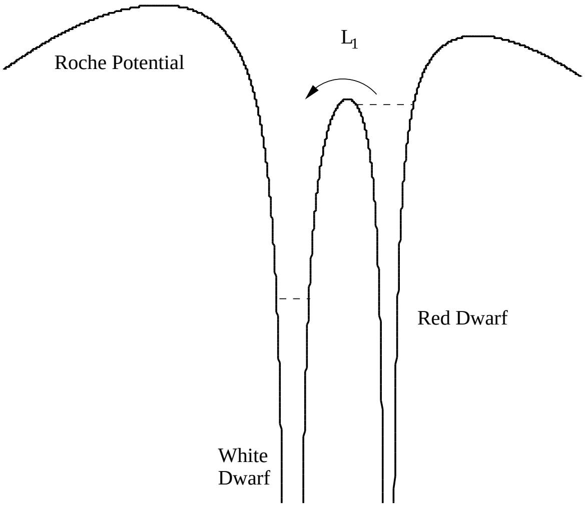

Figure 2.4: Cartoon of the Roche lobes as two lakes with a ridge between them. If the red dwarf fills its “lake” mass flows downhill into the white dwarf’s “lake”.

outer atmosphere of the primary, this is called a common-envelope system.

2.4 Mass transfer and accretion disk

Contrary to what one might think in the first place, the mass transfer from the secondary towards the primary does not take place from a large area of the red dwarf directly towards the white dwarf. Only from a very small patch, about a thousandth of the red dwarf’s surface, at the Lagrange point L_1, matter is pushed from the stellar atmosphere and forms a thin accretion stream. Matter is injected into the primary’s Roche lobe roughly with the sound speed in the atmosphere of the secondary. This is because the particles escape the atmosphere at the inner Lagrange point due to pressure and it can be shown that pressure changes travel roughly with the speed of sound, as a sound wave is a pressure wave. One might be tempted to think those escaped particles are now on their way directly to the white dwarf, but this is not the case. Seen from the outside the particles not only have the thermal velocity ($\sim$ 10 km/s) but also the velocity with which L_1 orbits around the center of mass. This velocity is of the order of 100 km/s. With this orbital motion the mass stream swings by the white dwarf passing at a minimal distance r_{min} and then settles as a ring with the radius r_{circ}, see Fig. 2.5 a & b. Shocks and turbulences in the stream help dissipate energy and allow the settling of the stream as a ring.

A conservation law now governs the further development of the stream – the angular momentum conservation. Particles in the stream had no possibility yet to lose angular momentum. As such the ring forms at a radius that ensures the particles in the ring still have the same angular momentum they had at the inner Lagrange point. This radius is called the circularisation radius. From the ring of matter at the circularisation radius it is only a small step towards a disk. The ring is slightly spread out, there are some matter blobs orbiting a little bit further inward and therefore faster and some blobs further out and therefore slower. Thus there is friction heating up the material. Energy is radiated away. Only the release of gravitational energy as parts of the gas decrease their orbital radii can provide this energy. But a decreasing orbit also means these parts of the gas lose angular momentum. Due to the conservation law it cannot just vanish, which leads to other parts of gas in the ring gaining angular momentum and increasing their orbital radii. The ring spreads out, Fig. 2.5 c. As angular momentum can be transported outward in the disk material can be transported inward and gravitational energy can be released. For non-magnetic white dwarfs[1] the disk spreads as far in as the white dwarf surface and as far out as the so called tidal radius. This is the radius where tidal interactions of the disk with the secondary transfer angular momentum back to the orbital motion of the secondary. Now the disk is fully formed and in a stationary state, see Fig. 2.5 d & d', as long as there is steady mass flux from the secondary. The disk that formed is called an accretion disk. A complete view of a cataclysmic variable system with annotations is also shown in Fig. 2.6.

The rate of the mass flux from the secondary through the accretion disk onto the white dwarf is called (mass) accretion rate and is commonly denoted by $\dot{M}$ throughout this work. One point worth noting is that the mean flux of the white dwarf and the mean flux of the accretion disk are roughly the same in a steady state with low $\dot{M}$. This can change dramatically if the accretion rate increases. More details about this is to be found when the dwarf nova phenomenon is discussed in Sec. 3.4.

---

[1] all white dwarfs with $B \lesssim 10^5$ G are seen as non-magnetic (Warner, 1995)

As noted above, the Roche geometry is solely dependent on the mass ratio q and the separation a of the two binary components. Thus also the circularisation and tidal radii depend only on q. However, the exact solution is too complicated to evaluate, only approximations or evaluation with computer programs is possible. Following Warner (1995) approximate formulae can be found for the circularisation radius

$$r_{\rm circ} = 0.0859 \cdot a \cdot q^{-0.426} \qquad \text{for } 0.05 < q < 1\,, \tag{2.4}$$

for the tidal radius

$$r_{\rm tidal} = \frac{0.60 \cdot a}{1+q} \qquad \text{for } 0.03 < q < 1\,, \tag{2.5}$$

and for the radius of the closest approach of a free-fall stream to the primary

$$r_{\rm min} = 0.0488 \cdot a \cdot q^{-0.464} \qquad \text{for } 0.05 < q < 1\,. \tag{2.6}$$

A physically more insightful but less accurate estimate for the circularisation radius is gained from the conservation of angular momentum for the gas stream. Particles start with the specific angular momentum at L_1 being

$$R_{L_1} v_{L_1} = R_{L_1} \cdot 2\pi R_{L_1} / P_{\rm orb}$$

and end up with the specific angular momentum at the circularisation radius

$$r_{\rm circ} v_{\rm Kepler}(r_{\rm circ}) = r_{\rm circ} \cdot \sqrt{\frac{GM_1}{r_{\rm circ}}}\,.$$

Equating this and using Kepler's law for the orbital period one obtains

$$r_{\rm circ} = (1+q)\frac{R_{L_1}^4}{a^3}\,. \tag{2.7}$$

One might wonder what happens as the disk reaches the white dwarf. The innermost parts of the disk rotate with Keplerian velocities of roughly 3,000 km/s, but the average white dwarf spinning with a rotational velocity of $\sim$ 300 km/s is almost stationary compared to that. Therefore some kind

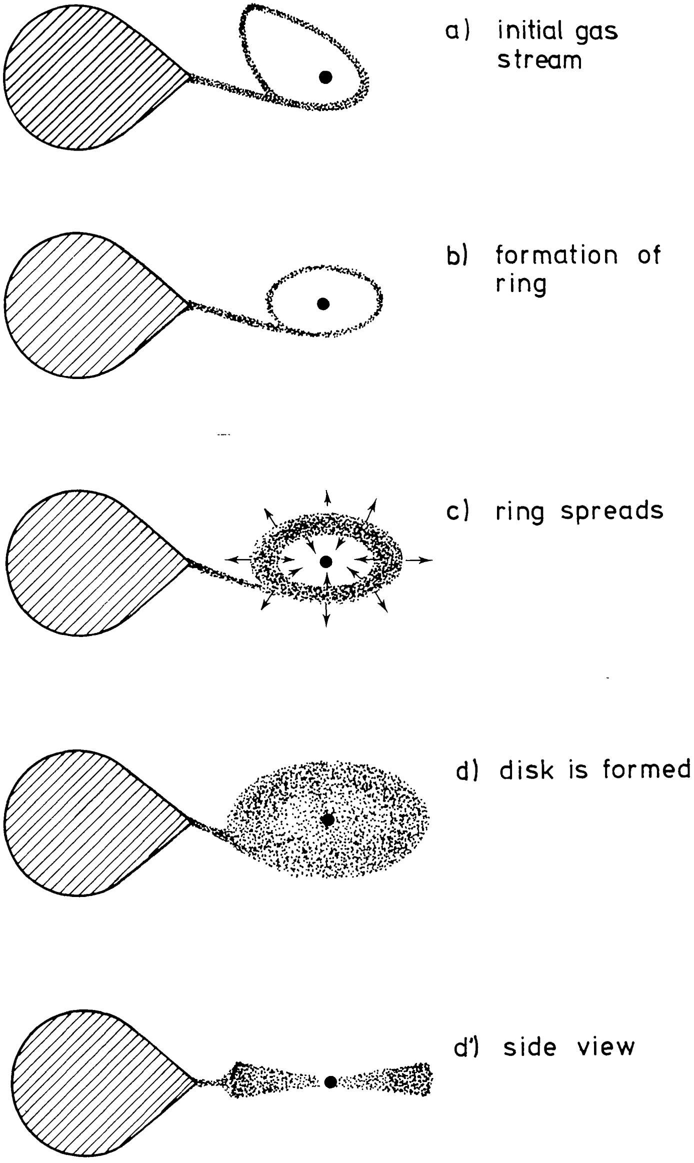
a) initial gas stream
b) formation of ring
c) ring spreads
d) disk is formed
d') side view

Figure 2.5: Schematic figure of the disk formation steps. Taken from Verbunt (1982).

of transition region – called *boundary layer* – must be between the disk and the white dwarf surface. All the excess kinetic energy is converted into heat and radiated away, this might make up to half the system luminosity. If the accretion rate is high enough, higher than $5 \cdot 10^{-10} \mathrm{M}_{\odot}/\mathrm{yr}$, there is enough material to make the boundary layer optically thick. It heats up and emits, to a first approximation, as a blackbody with roughly 200,000 K, which is about six times hotter than the hottest parts of the disk. Such a blackbody peaks in the soft X-ray and extreme ultraviolet (EUV) bands. For accretion rates less than $5 \cdot 10^{-10} \mathrm{M}_{\odot}/\mathrm{yr}$ this picture changes. Cooling rates are dominated by bremsstrahlung, but the densities are not high enough that this is very effective. The gas expands to compensate and forms a hot, diffuse and optically thin corona with a temperature of $\sim 10^{8}$ K. Mainly hard X-rays are emitted in such a state.

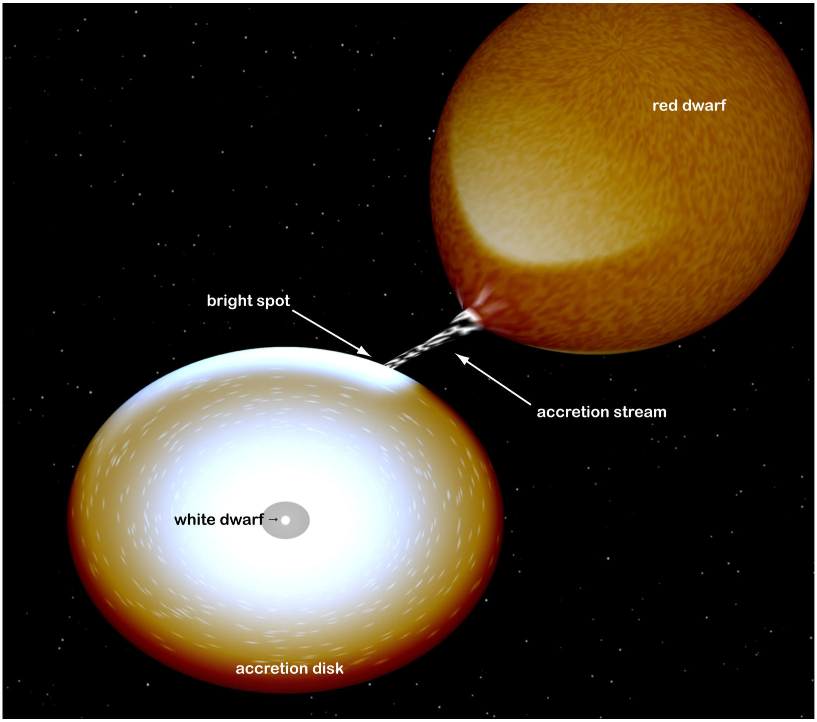

Figure 2.6: Still from a simulation of SS Cyg made with Rob Hynes *binsim* program. The main parts of a CV are labeled.

2.4.1 Magnetic CVs

So far we have only shown the building of an accretion disk and the accretion process in non-magnetic CVs. How do these things change if the white dwarf has a magnetic field? Keep in mind that the gas flowing from the atmosphere of the secondary is partially ionised. As such it consists of charged particles. Now the movement of charged particles in a magnetic field can be quite complicated, but for our purposes here the particle-field interaction can be boiled down to two principles. The first one is that for the motion of the gas there are only two cases to consider. One can either completely ignore the field to deduct the motion or completely ignore everything but the field. The second principle is that the field lines and the material flow are frozen together. Ionised gas can easily move along field lines but it cannot cross field lines. On the other hand the motion of the gas drags along the field lines.

For magnetic CVs the energy of the matter-field interaction close to the white dwarf is always larger than the kinetic energy of the accretion stream. Thus the material always follows the field lines and is funneled towards the magnetic poles of the white dwarf. Along the field lines the material is in free-fall and reaches supersonic velocities. The potential energy is completely converted to kinetic energy and not dissipated in viscous interactions as in an accretion disk. The material slams into tiny accretion spots at the magnetic poles with a radius of roughly one-hundredth of the white dwarf radius. A so called accretion shock forms above the accretion spot. In this shock the kinetic energy of the material is converted into X-rays and radiated away. Below the accretion shock there is an accretion column where radiative cooling due to bremsstrahlung and cyclotron emission happens. The accretion column consists of very hot plasma with temperatures of $10^7 - 10^8$ K and is a source of hard X-rays. The surroundings of the white dwarf pole are heated by this radiation and become a source of soft X-rays and extreme ultraviolet radiation. Compared to non-magnetic CVs, magnetic CVs thus emit most of their energy in X-rays and the far ultraviolet. The exact accretion geometry depends strongly on the magnetospheric radius r_{m} of the white dwarf. Inside this radius the magnetic field dominates, the accretion stream follows the field lines. A third principle applies here. Just outside the magnetospheric radius the material orbits with a Keplerian velocity. The magnetic field is in rigid rotation with the white dwarf rotation. The period of this rotation is called the spin period. Nature does like smooth transitions and the spin period adjusts itself in a way that in equilibrium it resembles the Keplerian motion at r_{m} avoiding a velocity jump for the material at this boundary. The direct result of this being that the spin period for white dwarfs with a low magnetic field is lower than that for white dwarfs with a high magnetic field. The higher the magnetic field, the further out the magnetospheric radius. For the highest magnetic fields in CVs this even leads to a coupling of the white dwarf magnetic field to the secondary – the secondary and the primary are forced to corotate.

Polars

Typical field strengths for highly magnetic CVs are in the range 10 - 100 MGauss. For these field strengths the magnetospheric radius r_m is larger than the circularisation radius r_circ. The angular momentum of the infalling gas is too low to form a disk with an inner radius larger than r_circ, which is obvious considering the definition of r_circ. For the part from L_1 to r_m the accretion stream takes the ballistic trajectory it would take in a non-magnetic CV just to snap to a field line at r_m and follow that to the magnetic poles. See Fig. 2.7 for a schematic picture. This class of CVs is called AM Her stars after the prototype star[2].

Besides the synchronism between the spin and orbital period a defining attribute is the large fraction of polarised (both linearly and circularly) radiation observed from these systems. Polarised light from these systems is mainly observed in optical and infrared and stems from the cyclotron emission in the accretion column. This polarisation is the reason why AM Her stars are also called polars. In general polars are strong sources of soft X-rays rather than sources of hard X-rays. Most likely the reason is that the gas in the stream is clumped, the clumps are not stopped by the shock and column but dissipate their energy deeper inside the atmosphere.

Extreme cases of AM Her stars exist with a magnetic field higher than 100 MGauss. For those systems the magnetosphere of the white dwarf extends further out than L_1. There is no ballistic stream, but the gas is channeled along the field lines directly from L_1. The most extreme case known is AR UMa with a magnetic field strength of 230 MGauss, which is thousands of times stronger than any field we can create on earth (Hellier, 2001).

Intermediate Polars

Let us take a look at lower magnetic fields. The situation gets more complicated here. As it turns out that for this case the system can be put together from a non-magnetic CV in the outer parts and the inner region of an AM Her

---

[2] It is common in astronomy to name classes after the first star discovered with the characterising attributes.

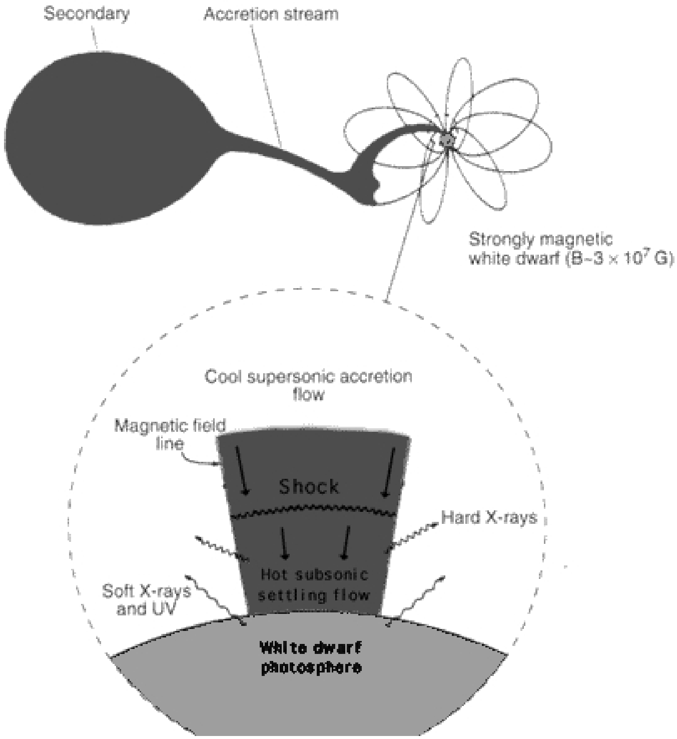
Secondary
Accretion stream
Strongly magnetic white dwarf (B~3 × 10⁷ G)
Cool supersonic accretion flow
Magnetic field line
Shock
Hard X-rays
Hot subsonic settling flow
Soft X-rays and UV
White dwarf photosphere

Figure 2.7: Schematic figure of a Polar or AM Her system. Mass from the secondary follows a ballistic trajectory until the energy density of the magnetic field is strong enough to funnel the flow along the field lines. A blow-up of the accretion region near the magnetic pole shows the shock and accretion column. Courtesy of NASA HEASARC.

star. Simplified speaking for r_m being smaller than the circularisation radius an accretion disk builds up just like it does in a non-magnetic CV, but with the inner parts of the disk ($r < r_\mathrm{r}$) cut out by the magnetic field. See Fig. 2.8 for a schematic view. One little subtlety occurs when the magnetospheric radius is smaller than the circularisation radius, but larger than the minimal distance r_min, then the first accretion stream is picked up by the field before a disk can form and a situation similar to a polar occurs. Because these systems are somewhere in between non-magnetic CVs and polars they are called intermediate polars or, after the prototype system, DQ Her stars[3]. It is interesting to note that despite their name almost no polarised radiation is seen from intermediate polars, mainly a result from their lower field strength of only 1 - 10 MGauss. Another difference to polars is that intermediate polars emit more hard X-rays than soft X-rays. The idea is here that the mass flux onto the poles is smoother as the material is taken from a smooth disk and then funneled along the field lines. Thus its energy is dissipated at the shock and in the accretion column, it does not punch through to the atmosphere. One of the most important points for DQ Her systems however is the spin of their white dwarfs. As mentioned above the spin of the white dwarf adjusts itself according to the mass flux and magnetospheric radius. This means that the white dwarf can be spun up or down by the mass flux which leads to white dwarfs in DQ Her stars being – with spin periods between thirty seconds and two hours – some of the fastest rotators known.

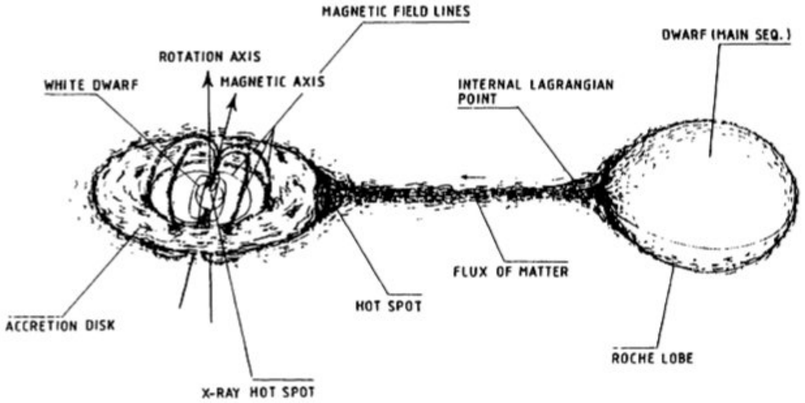
MAGNETIC FIELD LINES
DWARF (MAIN SEQ.)
ROTATION AXIS
WHITE DWARF
MAGNETIC AXIS
INTERNAL LAGRANGIAN POINT
FLUX OF MATTER
HOT SPOT
ACCRETION DISK
ROCHE LOBE
X-RAY HOT SPOT

Figure 2.8: Schematic figure of an intermediate polar or DQ Her system. A disk forms in the outer regions which is then truncated by the magnetic field. Taken from Giovannelli & Martinez-Pais (1991).

If the spin period is faster than the equilibrium period for the momentary mass flux and magnetospheric radius, for example because the white dwarf has been spun up by earlier stronger mass flux, the magnetic field can act as a propeller accelerating parts of the infalling gas and propelling it out of the system.

---

[3] Some authors distinguish between intermediate polars and DQ Her stars due to a difference in the spin period of the white dwarf. We will follow Hellier (2001) with the more modern viewpoint to see them as one class.

2.5 Evolution of cataclysmic variables

After the last section where we introduced cataclysmic variables, we are going to address the question how such a system forms and evolves during time, in this section. It all starts with the formation of a binary system, a likely process, only a minority of stars are single like our sun. A binary which will end up as a CV starts with one component in a mass range of $1\,\mathrm{M}_\odot < M_1 \lesssim 8\,\mathrm{M}_\odot$ and with a less massive component with $M_2 < M_1$ being separated by a few hundred solar radii, orbiting roughly every ten years. The more massive partner develops faster[4], expanding and becoming a red giant towards the end of its life. The red giant fills its Roche lobe and mass transfer onto the less massive companion sets in. This situation, the reverse of that in a cataclysmic variable, is unstable and produces a runaway effect. Mass transfered from the more massive partner onto the less massive one moves away from the center of mass of this system increasing its angular momentum. To compensate that and to obey angular momentum conservation the separation between the two components decreases. But this decrease in separation decreases the Roche lobe size, the red giant overfills its Roche lobe even more and even more material is transfered. The whole envelope of the red giant is dumped onto the secondary in this way and the time this takes is only limited by the flow speed of the transfered material. Indeed the process can only take a few years, extraordinary quick compared to the usual timescales in stellar evolution and astronomy in general. Due to all the dumped envelope of the red giant the companion star fills its Roche lobe too, a so called *common-envelope* phase with both components orbiting inside one common envelope begins. Inside the envelope movement is hampered by a huge drag force. Orbital energy is drained, the two components spiral inward reducing their separation from about $100\,\mathrm{R}_\odot$ to roughly $1\,\mathrm{R}_\odot$ in a timescale of around 1,000 years. The rotation of the binary inside the envelope acts like a propeller on the envelope expelling it to interstellar space. A planetary nebula is then formed by this expelled material.

What happens after the common-envelope phase ended? If the secondary fills its Roche lobe we start right away with a CV, if not we have a detached white dwarf - red dwarf binary system, called a pre-CV. For this case the separation needs to be reduced further by magnetic braking until the secondary fills its Roche lobe and mass transfer sets in. Magnetic braking works as the ionised particles in the stellar wind of the secondary follow the field lines of its magnetic field and are shot off to space like in a slingshot taking angular momentum with them. Important here is that the secondary is bound to corotate with its orbital motion due to tidal forces, very much like the moon shows always the same face towards the earth. This corotation ensures fast rotation rates, in the order of hours, for the secondary creating the strong field with a dynamo like effect. By this slingshot mechanism the angular momentum drained brakes the rotation of the secondary, but as this rotation is bound to the orbital motion in the end the angular momentum is supplied by the orbit, which shrinks in consequence.

---

[4] Luminosity scales with M^3, fuel reserves with M, thus the lifetime scales with M^{-2} (Hellier, 2001).

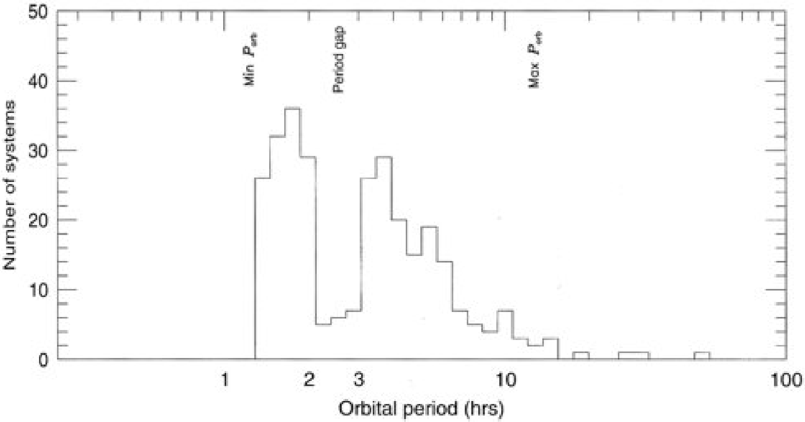

Figure 2.9: Distribution of orbital periods for cataclysmic variables. Logarithmic scaling on the time axis. Note the gap between 2 and 3 hours. Taken from Hellier (2001).

Magnetic braking is also important for the evolution of a CV after the mass transfer sets in, more on this in the next paragraph. To gain more insight into CV evolution the orbital period distribution (Fig. 2.9) is a helpful tool. The longest periods are in the range of 12 hours, this results from the requirement of the secondary to be less massive than the primary to avoid the runaway mass transfer as described above for the common-envelope phase. As a white dwarf the primary itself has an upper mass limit of the Chandrasekhar limit ($\approx 1.4\,\mathrm{M}_\odot$). A longer period thus a larger binary separation means a larger Roche lobe for the secondary to be filled. Larger Roche lobes are only filled by more massive stars thus a natural upper limit exists for CVs. The few systems with larger periods have an evolved secondary with an expanding envelope. Only very few white dwarfs with masses close to the Chandrasekhar limit exist, thus this criterium starts to reduce the number of systems already from periods around 6 hours onwards.

This upper limit is understood, but why are almost no systems found with a period between 2 and 3 hours? The key for this so called *period gap* is in the way how steady mass transfer in a CV is achieved. Gas flowing from the secondary onto the primary loses angular momentum, to keep that conserved the secondary gains angular momentum and the separation increases a little. This detaches it from its Roche lobe and some mechanism has to take away angular momentum from the whole system to reduce the separation again or the secondary has to evolve and fill its Roche lobe via expansion of the outer shell. Above the period gap magnetic braking provides the mechanism to keep the secondary attached to its Roche lobe. It is quite effective and can sustain a mass transfer rate $\dot{M} \sim 10^{-9}\mathrm{M}_\odot\mathrm{yr}^{-1}$, which is indeed observed for systems with longer periods. However, magnetic braking stops being effective around the 3 hour period mark, why is not yet fully understood. A second mechanism is therefore needed to sustain a stable mass overflow. This second mechanism is braking by gravitational wave emission. Close binaries cause spacetime ripples which drain energy from the binary systems' orbit. This way of losing angular momentum from the system is not as effective as magnetic braking and can only sustain a mass transfer rate of $\dot{M} \sim 10^{-10}\mathrm{M}_\odot\mathrm{yr}^{-1}$, rates indeed observed for systems below the period gap. The reason why mass transfer driven by gravitational wave radiation does not set in directly at the 3 hour period is that the red dwarf secondary has been pushed out of its equilibrium by losing mass from its outer shell and contracts back to an equilibrium as soon as the magnetic braking stops being effective. This contraction detaches it from the Roche lobe and it takes all the time until the system reaches the 2 hour period by gravitational wave radiation until it gets reattached to the lobe and mass transfer can set in again. The few systems which are observed with periods between 2 and 3 hours began their life as a CV just in the period gap therefore the secondary is not out of equilibrium.

The third feature in Fig. 2.9 important to mention is the sharp cutoff at a minimum period of roughly 80 minutes. This minimum occurs when the mass of the secondary reaches about $0.06\,\mathrm{M}_{\odot}$ and it becomes degenerate like the white dwarf. Such degenerate stars are not supported by gas pressure but by the quantum-mechanical Pauli exclusion principle that two particles cannot be at the same place in the same state. Peculiar about them is the resulting mass-radius relation, more massive degenerate stars are smaller than less massive degenerate stars. For white dwarfs this relation is $R \propto M^{-1/3}$. This means that once the secondary is degenerate it reacts with expansion towards further mass loss which increases the separation and the orbital period again. Model calculations show that the final fate of a CV would be a white dwarf with a Jupiter-like companion. No systems evolving from the minimum to larger periods have been detected so far, but the low mass transfer rates expected in those systems make them almost impossible to detect.

2.6 AM CVn stars

Despite the sharp drop in the number of systems below the 80 minutes period there are a few systems with lower periods. Such systems do not have a normal red dwarf as a secondary, but those secondaries are composed almost of pure helium and no hydrogen. Quite contrary to normal stars which consist of 92% hydrogen and 8% helium in number fraction. The special composition makes them more compact for the same mass as normal stars, because helium is heavier than hydrogen. For them a smaller orbital separation is necessary to be in contact with their Roche lobes. Such helium-rich cataclysmic variables are called AM CVn stars again after the first system found of this class. The evolution for AM CVn stars is similar to the evolution of normal CVs but shifted to shorter periods. Only gravitational wave radiation is more effective due to the small orbits and can sustain larger mass transfer rates.

Similarly to “normal” CVs the class of AM CVn stars can be divided in three subcategories depending on the mass accretion rate of the system. As the mass transfer rate in those systems depends on the effectivity of angular momentum loss via gravitational wave radiation, which in turn depends on the binary separation, this classification is also a classification in binary separation.

On the low mass transfer end, systems with, for AM CVns, longer periods ($40\,\mathrm{min} \lesssim P_{\mathrm{orb}} \lesssim 70\,\mathrm{min}$) are in a permanent low state. An accreting white dwarf and signs of an accretion disk are observed, but all is in a steady state and no large variabilities, e.g. outbursts, are observed.

Systems with orbital periods in the 20 to 40 minutes range have a higher

mass transfer rate and show dwarf nova-like outbursts. Consequently they are called outbursting systems.
The third subcategory contains those systems with the shortest orbital periods ($P_{\mathrm{orb}} \lesssim 20\,\mathrm{min}$, where the shortest period known so far with $P_{\mathrm{orb}} = 321\mathrm{s}$ is for RXJ0806). They support such high mass transfer rates that a constant outburst is observed as for nova-like CVs. Amongst these high state systems is the prototype AM CVn itself.

AM CVn stars are rare objects, only about twenty are known, because only particular initial conditions in a binary lead to those characteristics. Both partners have to go through a red giant phase with the second red giant phase being the common-envelope phase that reduces the orbital periods sufficiently enough to allow mass transfer between the two helium cores that remained from the red giants.
AM CVn stars are important objects to test our understanding of accretion physics in CVs. Do the almost pure helium disks in AM CVn systems behave differently than the hydrogen rich disks in normal CVs? Investigating such questions further enhances our ideas of what is going on in CVs and accretion disks in general. Important for this work are the outbursting and high state systems. Both – outbursting systems only in outburst – show spectral features typical for accretion disk wind outflow, see e.g. Wade et al. (2007). Comparing those outflows to “normal” CV outflows and getting more constraints on accretion rates are two goals of this work. Additionally AM CVn systems are ideal test candidates for gravitational wave detectors. It is expected that those systems have the best signal-to-noise ratio of all gravitational wave sources so far which makes them suitable targets after the launch of LISA (Laser Interferometer Space Antenna) in 2018 (Hils & Bender, 2000). For more detailed information about AM CVn systems see also Nelemans (2005) and references therein.

Cataclysmic Variables - summary

- semi-detached binary system
  - white dwarf primary ($T_{\rm eff} \approx 10{\rm kK} - 50{\rm kK}$)
  - red dwarf secondary ($T_{\rm eff} \approx 2{\rm kK} - 4{\rm kK}$)
- mass overflow
  - formation of an accretion disk (non-magnetic white dwarfs)
  - direct accretion or inner disk cut out (magnetic white dwarf)
- whole systems would fit in our sun
- time-evolution driven by different mechanisms
  - magnetic braking dominates above gap
  - gravitational wave radiation below the gap
- orbital periods from 12 hours to 80 minutes with a period gap between 2 and 3 hours
- AM CVn systems with even lower periods (down to a few minute
- “cataclysmic” outburst events – nova and dwarf nova eruptions

CHAPTER 3

Disks, outflow and dwarf novae

“Sometimes attaining the deepest familiarity with a question is our best substitute for actually having the answer.”
[Brian Greene]

Now after this general introduction to cataclysmic variables we are going to venture on into the details which will be important for our work with and understanding of these systems. We are going to start with accretion disk physics, put that to use in a closer look at the dwarf nova phenomenon and finish this chapter with the first thorough look at outflows in CVs. The complexity of the physics involved demands that only the most important results are presented in this introduction. For a fuller account see the detailed and comprehensive textbooks by Frank et al. (1985) and Hellier (2001), or the review by Smak (2001).

3.1 Accretion disks – a more theoretical introduction

How a disk develops from the first mass stream is something that we have shown from a schematic viewpoint in Sec. 2.4. For a closer look at the stream and the disk we have to describe the gas flow as a viscous fluid. That is because the mean free path of particles in the stream is $\sim$ 10 km which is very small compared to the scale of the binary (Prendergast, 1960). These basic equations of hydrodynamics and their derivations can be found in many textbooks, e.g. Landau & Lifshitz (1959). The gas has a velocity field $\vec{v}$, a density ρ and a temperature T, which are all given as a function of position $\vec{r}$ and time t. Mass conservation is then ensured by the *continuity equation*

$$\frac{\partial \rho}{\partial t} + \vec{\nabla} \cdot (\rho \vec{v}) = 0\,. \tag{3.1}$$

Conservation of momentum leads to the so called *Euler equation*

$$\rho\frac{\partial\vec{v}}{\partial t}+(\rho\vec{v}\cdot\vec{\nabla})\vec{v}=-\vec{\nabla}P-\rho\vec{\nabla}\Phi-\vec{\nabla}\cdot w\,, \tag{3.2}$$

with P being the total pressure, Φ the gravitational potential and w the viscous stress tensor. Equation (3.2) has the form (mass density) $\cdot$ (acceleration) $=$ (force density) and is just an expression of Newton's second law for a continuous flow (under the influence of a gravitational potential in this special case). The third conservation law is the conservation of energy which leads to an *energy equation*

$$\rho\frac{\partial\epsilon}{\partial t}+\rho\vec{v}\cdot\vec{\nabla}\epsilon=-P\vec{\nabla}\cdot\vec{v}-(w\cdot\vec{\nabla})\vec{v}-\vec{\nabla}\cdot\vec{q}, \tag{3.3}$$

with ϵ being the internal energy per unit mass and $\vec{q}$ the conductive flux of heat.

For an accretion disk in a CV several assumptions can be made in order to develop a theoretical model. The first and probably most important and successful point is to assume the disk to be geometrically "thin", which means the vertical height of the disk $H(r)$ at a radius r from the center of the white dwarf is much smaller than this radius,

$$H/r \ll 1\,. \tag{3.4}$$

This assumption can be justified; the accretion stream lies in the orbital plane and the impact of the stream material at the bright spot does not raise a significant part of it to larger heights above the disk plane, thus the infalling gas has momentum predominantly in the disk plane. The thickness of the disk is therefore only determined by hydrostatic equilibrium, which leads to a thin disk structure. In first order the disk can be taken as a two-dimensional flow, velocities in z-direction can be neglected ($v_{\mathrm{z}} \ll v_{\mathrm{r}}$).

Secondly, the gravitational influence of the secondary onto the disk can be neglected, which leads to an axially symmetric disk. This assumption holds for most parts of the accretion disk, only in the outermost parts interactions of disk and secondary are responsible for angular momentum transport from the disk to the orbit of the secondary. A natural choice is then a cylindrical coordinate system (r,ϕ,z) with the disk in the ($z=0$)-plane. For this choice $\partial/\partial\phi=0$ holds for all disk quantities.

For most parts of the disk the angular velocity $\Omega(r)$ will not differ to a significant amount from the Keplerian value $\Omega_\mathrm{K}(r) = \left(\frac{GM_1}{r^3}\right)^{\frac{1}{2}}$, which yields a circular velocity of

$$v_\phi = r\Omega(r) = r\left(\frac{GM_1}{r^3}\right)^{\frac{1}{2}} . \tag{3.5}$$

In addition the gas in the disk must possess a small radial drift velocity v_r as the viscous shear in the disk leads to spreading of the disk and accretion of matter onto the primary. The disk can be characterised by its *surface density* Σ, which is the mass per unit surface area given by integrating the gas density ρ through the disk with height H,

$$\Sigma(r,t) = \int_{-H/2}^{+H/2} \rho(z)\,\mathrm{d}z\,. \tag{3.6}$$

We can now put these assumptions to use in the basic equations of hydrodynamics (Eq. 3.1–3.3) to determine the time dependent disk structure. The continuity equation yields

$$\frac{\partial}{\partial t}\Sigma(r,t) = \frac{1}{r}\frac{\partial}{\partial r}\left[r\Sigma(r,t)v_\mathrm{r}\right] \tag{3.7}$$

and the conservation of angular momentum can be expressed as

$$\frac{\partial}{\partial t}\left(\Sigma(r,t)r^2\Omega(r)\right) + \frac{1}{r}\frac{\partial}{\partial r}\left(r\Sigma(r,t)v_\mathrm{r}r^2\Omega(r)\right) = \frac{1}{r}\frac{\partial}{\partial r}\left[r^3\nu_\mathrm{k}\Sigma(r,t)\frac{\mathrm{d}\Omega(r)}{\mathrm{d}r}\right] , \tag{3.8}$$

with ν_k being the coefficient of effective kinematic viscosity of the gas. Equations 3.7 and 3.8 can be combined to eliminate v_r. Furthermore using circular Keplerian orbits ($\Omega(r) \propto r^{-3/2}$) leads to

$$\frac{\partial}{\partial t}\Sigma(r,t) = \frac{3}{r}\frac{\partial}{\partial r}\left[r^{1/2}\frac{\partial}{\partial r}\left(\nu_\mathrm{k}\Sigma(r,t)r^{1/2}\right)\right] , \tag{3.9}$$

which is a *non-linear diffusion equation*, matter diffuses inwards onto the primary and angular momentum diffuses outwards to the outer edge of the disk (where it then is transported to the orbital motion via tidal interactions, but this is of course not covered in this equation).

Some more evolved calculus can be used on this diffusion equation to extract a timescale on which Σ evolves. It can be written as

$$t_\mathrm{v} \sim \frac{r}{v_\mathrm{r}} \sim \frac{r^2}{\nu_\mathrm{k}} , \tag{3.10}$$

and is commonly called *viscous* or *radial drift timescale*, because it gives an estimate of the timescale for a density perturbation at r to move a radial distance r. With the help of Eq. (3.9) it can be shown that the disk spreads with most of the mass moving inward and all the angular momentum moving outward with a small part of the mass, see e.g. Frank et al. (1985).

If external conditions, of main concern is the mass transfer rate from the secondary $\dot{M}$, change on timescales longer than t_{v}, which is the case in many CVs, then the disk settles in a steady state with $\partial\Sigma/\partial t = 0$. Of course this means $r\Sigma(r)v_{\mathrm{r}} = \mathrm{const.}$ The mass conservation equation (3.7) can then be integrated to give the obvious result

$$\dot{M} = 2\pi r\Sigma(r)(-v_{\mathrm{r}})\,, \tag{3.11}$$

where we have to keep in mind that $v_{\mathrm{r}} < 0$ as this represents the inflow of mass. For a proper integration of Eq. (3.8) or Eq. (3.9) boundary conditions at the inner and outer edges of the disk are needed. We consider a non-magnetic CV where the disk extends to the white dwarf surface ($r_{\mathrm{inner}} = R_{\mathrm{WD}}$). The white dwarf will rotate with an angular velocity $\Omega_{\mathrm{WD}} < \Omega_{\mathrm{K}}(r_{\mathrm{inner}})$, thus there needs to be a *boundary layer* where the fast rotating material from the disk decelerates, see also Sec. 2.3. What is most important for the boundary condition is that the boundary layer is expected to be very thin and no torque is applied to the disk at r_{inner}. Thus we can assume $\Omega(r_{\mathrm{inner}}) = \Omega_{\mathrm{K}}(r_{\mathrm{inner}})$. Using these boundary conditions and Eq. (3.11) we can integrate Eq. (3.9) and get

$$\nu_{\mathrm{k}}\Sigma(r) = \frac{\dot{M}}{3\pi}\left[1 - \left(\frac{R_{\mathrm{WD}}}{r}\right)^{\frac{1}{2}}\right]\,. \tag{3.12}$$

The viscous torques which are responsible for the angular momentum and thus mass transport through the disk are also responsible for heating the gas of the disk as they cause *viscous dissipation* within the gas at a rate of $G(r)\Omega'\mathrm{d}r = 2\pi r\nu_{\mathrm{k}}\Sigma r^2(\Omega')^2\mathrm{d}r$ per annulus of width $\mathrm{d}r$ with $\Omega' = \partial/\partial\Omega$ (Frank et al., 1985). Eventually this energy will be transported to the disk surface and radiated away with a dissipation rate $D(r)$ per unit surface area. Of course this energy will be radiated away through both surfaces of the annulus which have a total surface area of $4\pi r\mathrm{d}r$. We then find

$$D(r) = \frac{G(r)\Omega'}{4\pi r} = \frac{1}{2}\nu_{\mathrm{k}}\Sigma(r)\left[r\Omega'\right]^2\,. \tag{3.13}$$

Note that it is always $D(r) \geq 0$, with $D(r) = 0$ only in the case of rigid rotation. Inserting $\Omega = \Omega_{\mathrm{K}}$ gives $D(r) = \dfrac{9}{8}\nu_{\mathrm{k}}\Sigma(r)(GM_{\mathrm{WD}}/r^3)$. Combining this with

Eq. (3.12) we get

$$D(r) = \frac{3GM_{\rm WD}\dot{M}}{8\pi r^3}\left[1-\left(\frac{R_{\rm WD}}{r}\right)^{\frac{1}{2}}\right] . \tag{3.14}$$

In case the disk is optically thick in z-direction, each disk surface element roughly radiates as a blackbody with a temperature $T_{\rm eff}(r)$ given by equating the dissipation rate per unit surface area to the blackbody flux:

$$\sigma T^4_{\rm eff}(r) = D(r) . \tag{3.15}$$

Using Eq. (3.14) we get

$$T_{\rm eff}(r) = T_* \left[\frac{r}{R_{\rm WD}}\right]^{-\frac{3}{4}}\left[1-\left(\frac{R_{\rm WD}}{r}\right)^{\frac{1}{2}}\right]^{\frac{1}{4}} , \tag{3.16}$$

where

$$T_* = \left[\frac{3GM_{\rm WD}\dot{M}}{8\pi\sigma R^3_{\rm WD}}\right]^{\frac{1}{4}} . \tag{3.17}$$

For $r \gg R_{\rm WD}$ the effective temperature (3.16) can be approximated as

$$T_{\rm eff} = T_* \left(r/R_{\rm WD}\right)^{-3/4} . \tag{3.18}$$

Using local blackbody emission a first estimate of an accretion disk spectrum can be calculated. This spectrum and the temperature stratification in the disk with its peak close to the inner boundary is clearly different from any stellar atmosphere. The temperature range covered by an accretion disk is quite large and thus disks in CVs are expected to be strong UV, or even FUV for higher accretion rates, emitters but can also radiate in IR on their outer edges.

So far we have completely neglected the vertical structure of the disk, which we show in the following. As mentioned above the disk height is governed by the hydrostatic equilibrium

$$\frac{1}{\rho}\frac{\partial P}{\partial z} = \frac{\partial}{\partial z}\left[\frac{GM_{\rm WD}}{(r^2+z^2)^{1/2}}\right] , \tag{3.19}$$

which is nothing else than the z-component of the Euler equation (3.2) with all velocity terms neglected. For our thin disk assumption $z \ll r$ this simplifies to

$$\frac{1}{\rho}\frac{\partial P}{\partial z} = -\frac{GM_{\rm WD}z}{r^3} . \tag{3.20}$$

With H being the scale height of the disk, for which the thin disk requires $H \ll r$, we can write $\partial P/\partial z \sim P/H$. With the pressure $P \sim \rho c_{\mathrm{s}}^2$, where c_{s} is the sound speed, we can derive the relation

$$c_{\mathrm{s}} \approx \frac{H}{r}\left(\frac{GM_{\mathrm{WD}}}{r}\right)^{\frac{1}{2}} \ll v_{\mathrm{Kepler}} \,. \tag{3.21}$$

For a thin disk the local Keplerian velocity is highly supersonic. As a last part of this more theoretical introduction to thin accretion disks we show that the Keplerian velocity is not just an assumption, but follows from the thin disk approximation. Starting from the radial component of the Euler equation (3.2)

$$v_{\mathrm{r}}\frac{\partial}{\partial r}v_{\mathrm{r}} - \frac{v_\theta^2}{r} + \frac{1}{\rho}\frac{\partial}{\partial r}P + \frac{GM_{\mathrm{WD}}}{r^2} = 0\,, \tag{3.22}$$

where the pressure term $\partial P/\partial r$ can be neglected because of (3.21) by comparison with the gravity term. Using equations 3.11 and 3.12 the r-derivative can be evaluated to yield

$$v_{\mathrm{r}} = -\frac{3\nu_{\mathrm{k}}}{2r}\left[1 - \left(\frac{R_{\mathrm{WD}}}{r}\right)^{\frac{1}{2}}\right]^{-1} \,. \tag{3.23}$$

If we use the α-parametrisation, see next section, for the viscosity $\nu_{\mathrm{k}} = \alpha c_s H$ we get

$$v_{\mathrm{r}} \sim \nu_{\mathrm{k}}/r = \alpha c_s \frac{H}{r} \ll c_s\,, \tag{3.24}$$

and see that v_{r} is highly subsonic. Obviously the $v_{\mathrm{r}}\partial v_{\mathrm{r}}/\partial r$ term in Eq. (3.22) is thus even smaller than the pressure term. Those terms are therefore only a small perturbation and can be neglected. Equation (3.22) can then be rewritten as

$$v_\phi = \left(\frac{GM_{\mathrm{WD}}}{r}\right)^{\frac{1}{2}}\left[1 + \mathcal{O}((c_s/v_\phi)^2)\right]\,, \tag{3.25}$$

which is the Keplerian velocity up to small perturbations.

3.2 The α-disk model

There was – and there still is – no completely satisfying theory of viscosity in accretion disks. To overcome this limitation Shakura & Sunyaev (1973) started with the idea that the viscosity somehow has to be caused by turbulence in the gas flow of the disk and introduced the famous α*-parametrisation*

$$\nu_{\mathrm{k}} = \alpha c_s H \,. \tag{3.26}$$

The eddies[1] responsible for the turbulent viscosity are smaller than the disk height H and the turbulent velocity is subsonic. A second possible source for viscosity are small and chaotic magnetic fields, which are in the disk due to the moving gas being partly ionised. For this source of viscosity the same α-prescription can be derived. For both assumed sources of viscosity the expectation is $\alpha \lesssim 1$ and indeed observations (see e.g. Verbunt (1982) and references therein) support $\alpha \approx 0.01 - 1$. It is very important to note that we cannot learn about the physics of the underlying viscosity mechanism by looking at α. It is merely a parameter[2] which helps us doing calculations and learning about disk systems without worrying about the viscosity.

Using this so-called *alpha disk*[3] prescription self-consistent models of stationary thin accretion disks can be calculated. The most important features are the large area of the disk (it almost fills the entire Roche volume of the primary), its concavity ($H \propto r^{9/8}$, although not necessarily so if α varies with r) and its small mass ($M_{\mathrm{disk}} \approx 10^{-9} \cdot M_{\mathrm{WD}}$). Gas pressure dominates the disk for a white dwarf primary, whereas most opacity is due to free-free scattering. We can also get some numbers on the speed estimates of the previous subsection. The Keplerian motion of the gas is of order $v_\phi \approx 1000\,\mathrm{km\,s^{-1}}$ exceeding the sound speed $c_{\mathrm{s}} \approx 10\,\mathrm{km\,s^{-1}}$ in the gas, which in turn is much faster than the drift speed of the gas in r-direction ($v_{\mathrm{r}} \approx 0.3\,\mathrm{km\,s^{-1}}$).

The most promising theoretical approach to overcome the limitations of the α-parametrisation is a magnetohydrodynamic (MHD) turbulence called magneto-rotational instability (MRI) rediscovered by Balbus & Hawley (1991). It works in the following way: A solely vertical magnetic field line might have some smaller deviations to larger and smaller radii. Two opposing forces now act on these kinks in the field line, the influence of gravity and rotation tries to increase the kink whereas the magnetic tension tries to smoothen out the kink. Let us assume for simplicity that the bulges of the perturbed field line rotate with the same velocity as the unperturbed field line. Then the outward bulge rotates faster than the Keplerian value requires and it is thus pulled further out, whereas the inward bulge rotates slower than required and it is thus pulled further in. If the field lines get stretched too far they ultimately “snap” and reconnect at their new radii taking bubbles of gas with them. This MRI can therefore transport material to different radii in a way that provides the turbulence needed for a viscous flow in the disk. It is intuitive that the effect only works for small field strength as a strong field would not allow the kinks to grow. For a review see Balbus & Hawley (1998).

---

[1] An “eddy” is a circular movement of gas, very much like a small whirlpool.

[2] α has not even to be constant throughout the disk.

[3] Synonymously used is the term SHS disk (SHakura-Sunyaev disk)

3.3 Spectral signatures of accretion disks

After the more theoretical introductions to accretion disks let us now see some observational signatures of accretion disk spectra. Lightcurves with evidence of an accretion disk are shown in Fig. 3.6 and 2.2, but what are the spectral signatures of accretion disks?

3.3.1 Origin of emission and absorption lines

Quite contrary to most stellar spectra where absorption lines are dominant, accretion disk spectra are often dominated by emission lines. Spectral lines are created when an atom absorbs a photon with just the fitting energy to jump up to another energy level[4]. Following such an absorption event it is very likely that the atom emits a photon with the same wavelength as the absorbed one to de-excitate again. Indeed in “local thermodynamic equilibrium” (LTE) the number of absorptions equals the number of emissions.

This is the case for *optically thick* media (in our case gas clouds), where the mean free path photons travel before the next interaction is very small. If the whole area is isothermal absorption and emission cancel and only a featureless blackbody spectrum is seen. However, stellar atmospheres and accretion disk atmospheres are not isothermal, but are hotter inside than outside. Photons we observe on the outside of a gas cloud come in average from a depth equal to the mean free path, or in other words from an optical depth $\tau = 1$. As the mean free path is larger for continuum photons than for line photons, line photons originate closer to the media’s surface than continuum photons. If the surface is cooler than the inside then there is more flux in the continuum than in the lines which results in the lines appearing as absorption features.

---

[4] Energy levels might be energy levels of electrons, but also energy levels in the nucleus, although in the optical and ultra-violet wavelength range only different levels for electron energies are relevant.

In the case when a gas cloud is *optically thin*, which means that the mean free path is longer than the extend of the cloud, the optical depth of the cloud is $\tau < 1$ and photons pass it practically unscathed. This also means that all line photons which are emitted in the cloud, e.g. due to collisional excitation or photo-ionisation, escape and the resulting spectrum consists of the continuum from behind the cloud plus the line photons emitted in the cloud. Therefore we observe an emission line spectrum.

3.3.2 Double peaked lines

Whether a disk spectrum appears with emission or absorption features, or maybe even both, depends on the state of the system and on the area in the disk where the features are produced. Figure 3.1 shows a time evolution for observed spectra of the dwarf nova SS Cyg. These observations suggest that in outburst most parts of the disk are optically thick and maybe surrounded by an optically thin corona responsible for the emission cores (lines in the centers of the absorption features). In quiescence the main features are in emission suggesting optically thin parts playing a crucial role.

A second important feature arises from the Keplerian rotation of the accretion disk. Emitted photons are Doppler shifted according to their motion with respect to the observer,

$$\nu(v) = \nu_0 \cdot \sqrt{\frac{1 - v/c}{1 + v/c}}\,, \tag{3.27}$$

where $v = v_{\mathrm{Kepler}} \sin i \sin \theta$ is the projected velocity in the observer's line-of-sight, with i being the inclination angle between the line-of-sight and the disk normal, and θ is the azimuth of the observer relative to the radius vector of the emitting material in the disk. In the top panel of Fig. 3.2 the loci of constant radial velocity for a observer located at the bottom of the panel are traced. These form a dipole field pattern. Different sizes for the areas of constant velocity for different velocities lead to different fluxes at the according Doppler shifted frequencies. Due to the rotational symmetry of an accretion disk the same emitting area moves away and towards the observer, a symmetric, double peaked emission feature is the result. The higher the inclination angle, which means the closer the system is seen edge on, the more prominent is such a double peaked emission line. Figure 3.3 shows an observation of the high inclination ($i = 82°$) dwarf nova Z Cha in quiescence (Horne & Marsh,

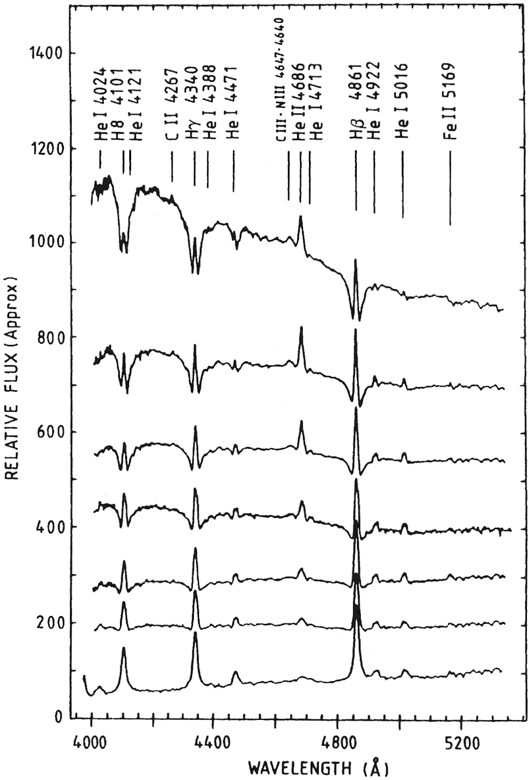

Figure 3.1: Spectral evolution of SS Cyg from maximum outburst (top) back to quiescence (bottom). Taken from Hessman et al. (1984). The system becomes cooler (the spectrum becomes flatter) and the absorption features disappear.

1986) where the Hα line beautifully resembles the theoretical predictions introduced in this subsection. Such a double peak structure is not only visible in emission, but is also found in some absorption lines.

3.4 *Dwarf novae*

In chapter 2 we presented different outburst phenomena in cataclysmic variables, now we take a closer look at dwarf novae. Why dwarf novae are especially important for understanding accretion disks and outflows from accretion

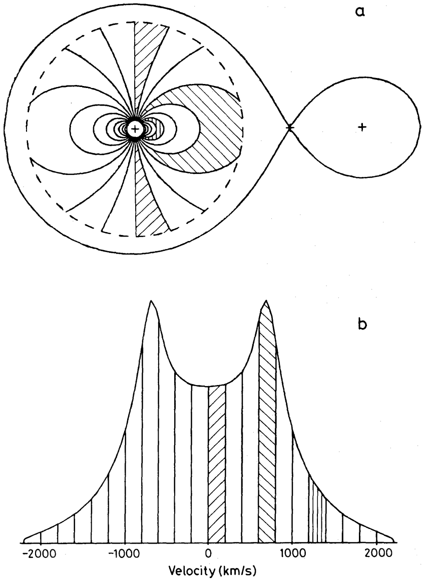

Figure 3.2: The top panel shows a Keplerian accretion disk in a binary (mass ratio $q = 0.15$). Loci of constant radial velocity form a dipole field pattern on the disk surface. The bottom panel shows the velocity profile of emission lines from the disk for an observer located at an edge on position below the white dwarf in the top panel. The shades in the velocity bins correspond to the disk regions. Taken from Horne & Marsh (1986).

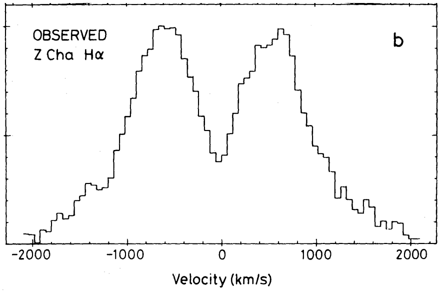

Figure 3.3: Hα line profile from the almost edge on ($i = 82°$) dwarf nova Z Cha in quiescence as observed with the Anglo-Australian Telescope by Horne & Marsh (1986).

disks, is illustrated in this section.

Dwarf novae are non-magnetic cataclysmic variables which show semi-regular outbursts with jumps in intensity by several magnitudes in a day or so, just to stay bright for about a week before declining back to a quiescence state again. Recurrence times range from weeks to months or even years. Even for one system the recurrence time and duration of an outburst can vary by a fair amount. A good example being the best studied dwarf nova, SS Cyg, which we will encounter in much greater detail again below (Sec. 5.3), with outburst cycles ranging from 15 to 95 days and outburst durations ranging from 2 to 22 days (Smak, 2001). The group of dwarf novae is not one homogeneous group within the CVs, but can be subdivided into three subgroups depending on their outburst behaviour.

Z Cam stars show the standard dwarf nova behaviour with outburst and quiescence, but from time to time the outburst persists with a constant brightness of about 0.7 mag below the peak outburst level before returning to quiescence. These so called *standstills* can last for days up to years. See the upper panel of Fig. 3.4 for a lightcurve of Z Cam itself. We are presenting Z Cam more thoroughly in the results section 5.4.

SU UMa stars show in addition to normal outbursts less frequent *superoutbursts* with slightly higher amplitudes $(+\sim 0.7\mathrm{mag})$ and much longer duration – up to 5 times a normal outburst duration. A characteristic feature of a superoutburst are superhumps, variations in the lightcurve which are a few percent longer than an orbital period. They appear shortly after the superoutburst maximum and persist from then on through its decline. A lightcurve of SU UMa is shown in Fig. 3.4 in the lower panel.

All dwarf novae which do not belong to one of these two subclasses are collected in the *U Gem stars* subclass. These show just the *normal* semi-periodic outburst-quiescence behaviour. An example of such a lightcurve is the one of U Gem itself shown in Fig. 3.5.

3.4.1 Outburst mechanism

Where do these dwarf novae outbursts come from? As we have seen earlier lightcurves of eclipsing systems tell us many things about what is happening in CVs. In Fig. 3.6 six eclipse profiles for OY Car (Rutten et al., 1992) are shown ranging from quiescence to the time of highest luminosity in outburst. The eclipse profile in quiescence is quite similar to the eclipse profile of Z

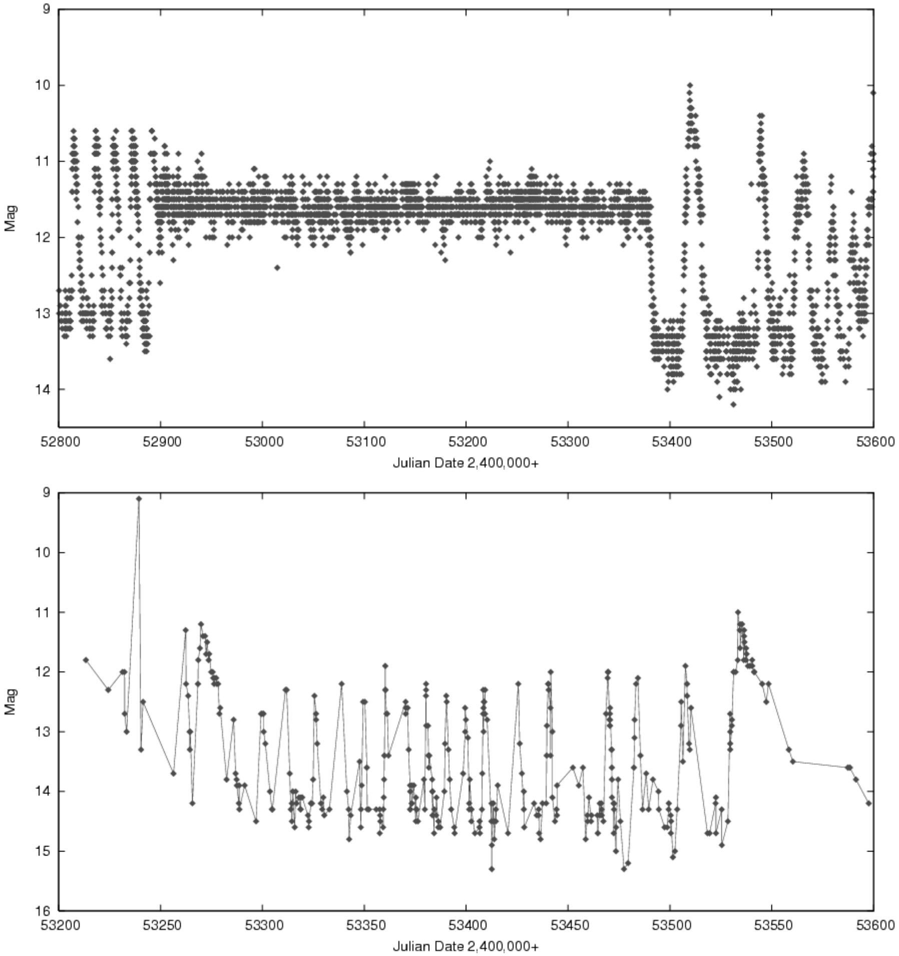

Figure 3.4: Lightcurve of Z Cam (top) and SU UMa (bottom). Data compiled by American Association of Variable Star Observers (AAVSO).

Cha shown in Fig. 2.1 where the different components of the system sum to an asymmetric lightcurve dominated by the white dwarf and a bright spot. The closer the system to the outburst peak the more the eclipse profile is dominated by and resembles the smooth symmetric and shallower eclipse of the accretion disk. Compare the upper panels in Fig. 3.6 with the disk component

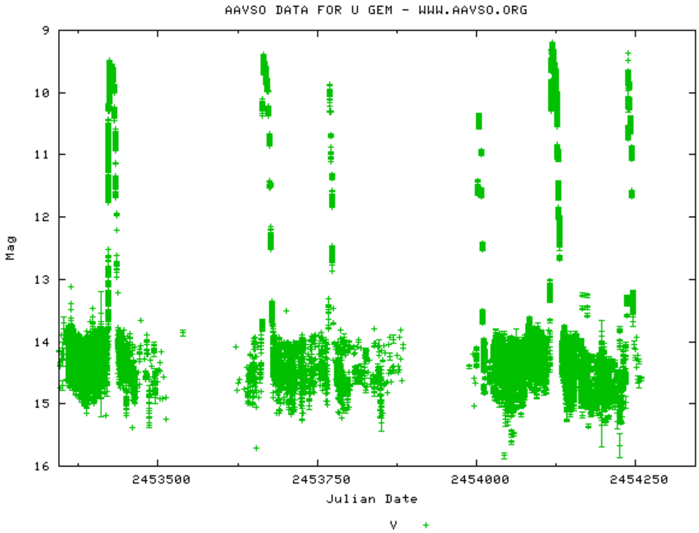

Figure 3.5: Lightcurve of U Gem, 1000 days in V band. Data compiled by American Association of Variable Star Observers (AAVSO).

in Fig. 2.2 to see the resemblance. These observations show clearly that a dwarf nova outburst is a sudden and dramatic brightening of the accretion disk.

Osaki (1974) proposed that the cause for an outburst is an instability in the accretion disk. The arc of reason for this so called *disk instability model (DIM)* starts with a constant mass transfer rate from the secondary which is higher than what could be transported through the disk by viscous interactions. If this is the case material piles up in the disk which eventually leads to an instability in the disk which greatly enhances the viscosity and thus the angular momentum transfer. With a more effective angular momentum transfer more material can be transported through the disk and the mass accretion onto the white dwarf is boosted. This boosts the luminosity of the disk and the whole system and drains the disk of material at the same time. The drained disk drops back into the low-viscosity quiescence state where it is slowly refueled by the accretion stream for the next outburst.

An alternative model was proposed by Bath (1975) in which the increased

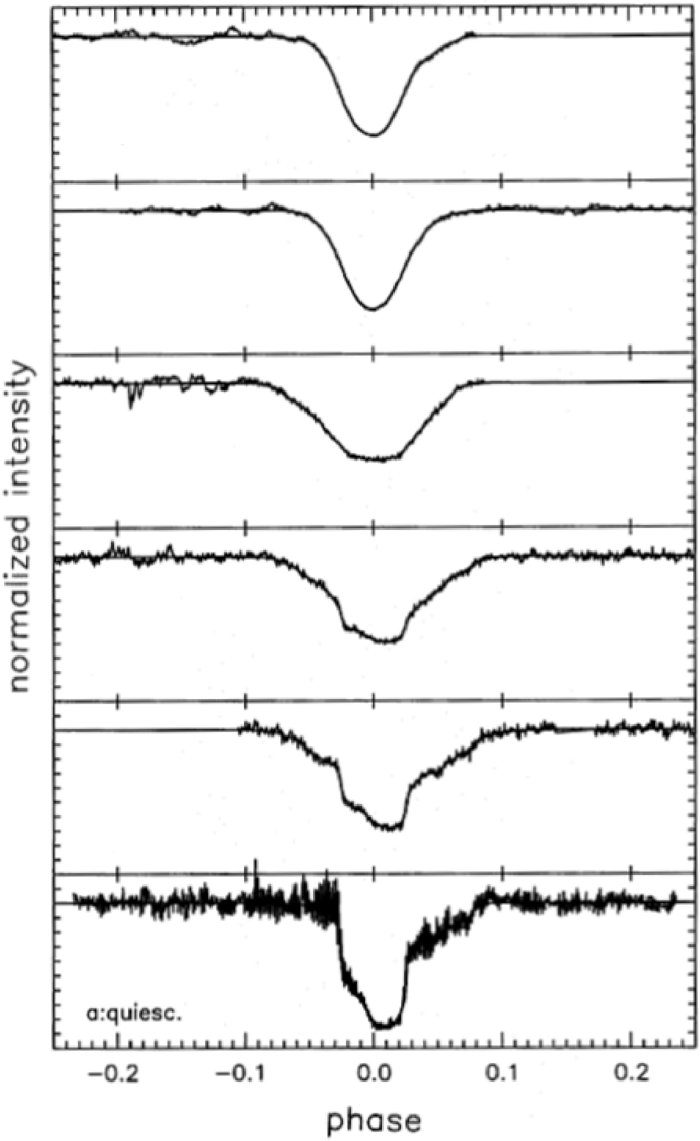

Figure 3.6: Eclipse profiles for OY Car stacked from quiescence (bottom) to brightest during outburst (top). Taken from Rutten et al. (1992).

mass transfer rate stems from mass burst from the secondary (*mass transfer instability, MTI*). Observations however do not show an increased luminosity of the bright spot during outburst, which strongly speaks in favour of the DIM. A second big point in favour of the DIM concerns the change of disk radius over an outburst cycle. In the disk instability model enhanced viscosity means enhanced angular momentum transport which spreads out the disk. It expands in- and outwards at the start of the outburst. During quiescence more material with angular momentum of the L_1 (corresponding to the angular momentum at $r_{\rm circ}$) gets added to the disk. As this is less angular momentum than material at the outer edge of the disk has it causes the disk to shrink. For the MTI model the disk would shrink in outburst due to the enhanced mass transfer and expand during quiescence. However, observations show that the disk expands during outburst. These observational results together with a working theoretical model for DIM developed in the early 80ies starting with the pioneering work of Meyer & Meyer-Hofmeister (1981) leads to an almost universal acceptance of the disk instability model.

The underlying mechanism of the DIM is a thermal instability of the disk, which can be linked to the MRI. For the MRI to work there need to be ions in the disk for creating a magnetic field and then coupling to it. This is, of course, the case if the disk is hot and ionised, but not if it is cool and unionised. Interestingly a flip between hot and cold states can be achieved with the help of changing the gas from neutral atoms to ionised plasma. Energy transport by radiation depends on the opacity κ. Low opacity means the radiation can propagate without large obstruction. With the propagating photons energy is also transported over larger distances. If the opacity is large however, radiation cannot propagate far, it is trapped and such is the energy of the photons. Neutral atoms, for example hydrogen at a few thousand K, have a low opacity, but if hydrogen is heated to $\sim$ 7.000 K it starts to ionise and the opacity grows[5]. The photons are trapped in the area with increasing opacity and their energy is used for further ionising the surrounding material rather than increasing the temperature. This leads to the fact that in a partially ionised medium the opacity is very sensitive to temperature, namely $\kappa \propto T^{10}$. An illustration of the instability is most easily done by looking at a plot of effective temperature $T_{\rm eff}$ versus surface density Σ as shown in Fig. 3.7.

A qualitative understanding of the $\Sigma - T$ relation can be gained when we use

---

[5] Particularly $\rm H^-$ ions are important for the opacity. They are created as free electrons from the ionised plasma attach to still existing H atoms.

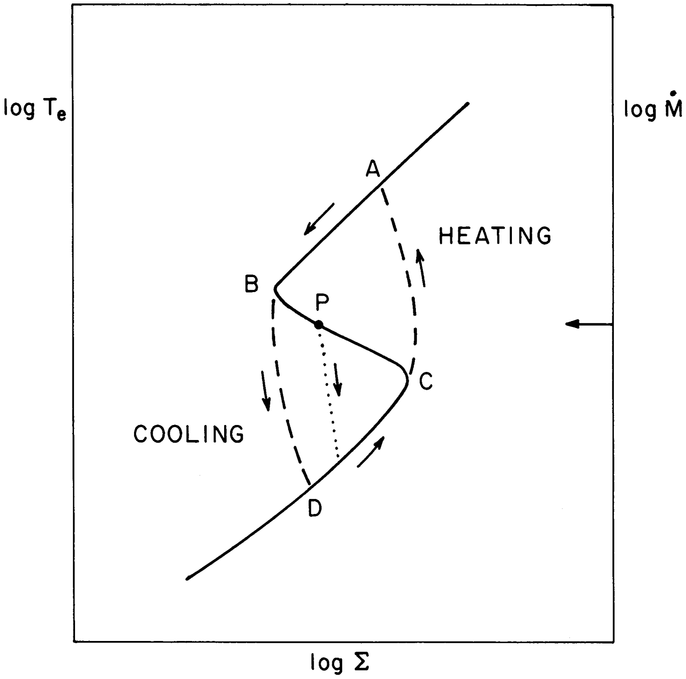

Figure 3.7: Dwarf nova cycle in surface density Σ versus disk temperature $T_{\rm eff}$. Taken from Smak (1984).

equations (3.12) and (3.16) to find

$$\dot{M} \propto T_{\rm eff}^4 \propto \nu_{\rm k}\Sigma\,. \tag{3.28}$$

This can be rewritten using the α-prescription (3.26) and the proportionalities $c_{\rm s} \propto \sqrt{T_{\rm mid}}$ and $H \propto \sqrt{T_{\rm mid}}$ to yield

$$T_{\rm eff}^4 \propto \alpha T_{\rm mid}\Sigma\,, \tag{3.29}$$

with the distinction between the effective temperature at the disk surface, $T_{\rm eff}$, and the temperature at the mid-plane of the disk, $T_{\rm mid}$, where most of the viscous energy dissipation occurs. A link between $T_{\rm eff}$ and $T_{\rm mid}$ is given by the opacity κ. In the case of κ being only a weak function of temperature the energy transport in z-direction is steady and thus $T_{\rm eff} \propto T_{\rm mid}$ which results in

$$\alpha\Sigma \propto T_{\rm eff}^3\,, \tag{3.30}$$

an increase in surface density leads to an increase in temperature. This is the case if the gas is either “fully” ionised (hot, corresponding to the BA branch in Fig. 3.7) or not ionised at all (cold, corresponding to the DC branch). Both of these branches are stable against small perturbations. In the partially ionised region, however, it is $\kappa \propto T^{10}$ and the effective surface temperature decouples from mid-plane temperature with $T_{\mathrm{mid}} \propto T_{\mathrm{eff}}^{10}$. Hence in this regime

$$\alpha\Sigma \propto T_{\mathrm{eff}}^{-6}, \tag{3.31}$$

from which a reduction of surface density with an increasing surface temperature can be deduced. This is the CB branch in Fig. 3.7 which is unstable against perturbations.
Let us now take a look at a complete limit cycle in Fig. 3.7. Suppose the disk gets fed with matter at a constant rate $\dot{M}$, as marked by the arrow on the right-hand side, from the secondary. The model that describes this situation would be at the point P located on the unstable branch. A random perturbation of $\Delta T_{\mathrm{eff}} < 0$ moves the model into the cooling area where it cools and moves down until it reaches the stable branch DC. It must be emphasised that the starting condition and the direction of the random perturbation are irrelevant as the model has to reach one of the stable branches eventually. On the DC branch the *local* accretion rate $\dot{M}_{\mathrm{loc}}$ is lower than $\dot{M}$, therefore the local surface density Σ increases which moves the model up and to the right on the DC branch. Σ still grows at the point C and this pushes the model over the critical surface density Σ_{C} at C and in the area where ionisation sets in. A runaway rise in temperature occurs. This heating happens on a much shorter timescale than the viscous timescale t_{visc} on which the surface density changes, thus Σ stays almost constant during the runaway. After hydrogen is completely ionised the model settles in a new equilibrium with increased T_{eff} and luminosity on the stable BA branch. Now $\dot{M}_{\mathrm{loc}}$ is *higher* than $\dot{M}$, the local surface density drops and the model moves to the left and down the BA branch until it reaches B. There hydrogen becomes partially ionised again, a small drop in surface density leads to a runaway drop in temperature and the model returns to the cold, low luminosity state on the DC branch. The cycle begins again.

The limit cycle just presented quite nicely resembles a dwarf nova outburst cycle as it is described by the disk instability model. In quiescence we are on the cold, low luminosity DC branch where the disk gets replenished until it reaches the instability at C with an outburst catapulting it to the hot, high luminosity state on the AB branch. Now more material is accreted onto the primary and a gradual drop back to the quiescence state follows. However, the limit cycle as presented above is a local phenomenon only valid for one disk ring at radius r. For a complete disk to reach an outburst state such an instability developed in one ring has to push adjacent rings into the hot state like in a domino game. How this "game" develops depends on the actual surface density distribution in the disk and on the radius where the outburst originates. The latter depends on the rate $\dot{M}$ at which material from the secondary is supplied to the disk. If this rate is low gas flows through the disk and the critical surface density $\Sigma_{\mathrm{C}}(r)$ is reached in the inner parts of the disk first. An inside-out outburst follows. For a high accretion rate the material is piled up faster than it can flow through the disk and $\Sigma_{\mathrm{C}}(r)$ is reached in the outer parts first and an outside-in outburst is the result.

Where $\Sigma_{\mathrm{C}}(r)$ is reached the limit cycle sets in, the first domino stone falls, and the heat produced there diffuses to the neighbouring rings. This heat pushes the surface density there over $\Sigma_{\mathrm{C}}(r)$, the next domino stones tumble and a heating wave travels through the whole disk. An example of an outside-in outburst as calculated by Mineshige & Osaki (1985) is shown in Fig. 3.8. With this heating wave picture the different rise-times for outside-in and inside-out outburst types can be understood. In the former case the heating wave travels with the gas flow and is thus faster as in the latter case where it travels against the flow.

The local mass transfer rates in outburst are always higher than the transfer rate from the secondary, locally we are on the BA branch and Σ drops until the second critical value Σ_{B} is reached, the temperature drops again. This will happen first in the outer parts of the disk and through diffusion processes a cooling wave travels inward (Fig. 3.8 lower panel). Cooling waves travel always outside-in independent whether the heating occurred with an outside-in or inside-out heating wave.

The last interesting and important point to note in this section is model calculations of outburst lightcurves indeed show different values for α in outburst and quiescence when comparisons with observations are made. Just like one would expect from the MRI picture of viscosity α turns out to be higher in the high state than in the quiescence state. Mineshige & Osaki (1985) find for example $\alpha_{\mathrm{outburst}} \approx 0.1$ and $\alpha_{\mathrm{quiescence}} \approx 0.03$.

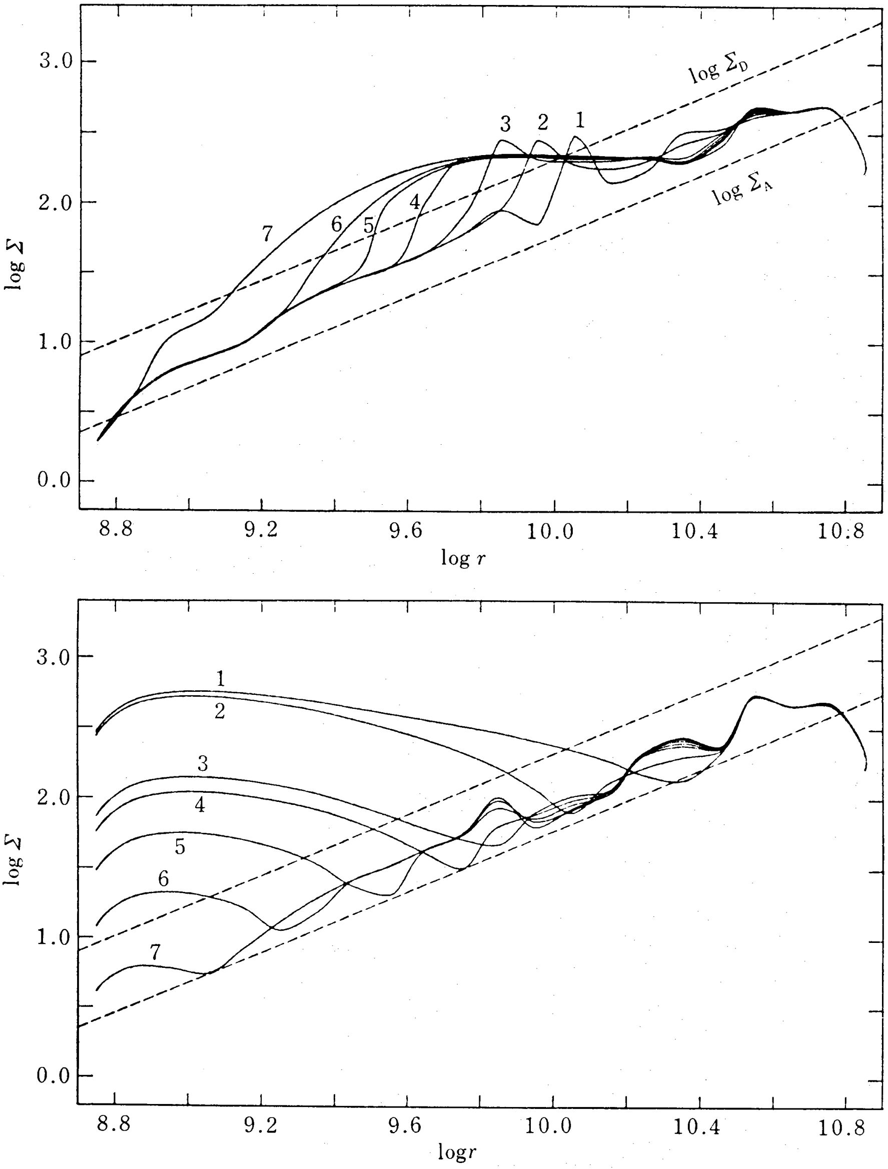

Figure 3.8: Time evolution of surface density $\Sigma(r)$ during an outside-in outburst on the top panel. Elapsed times for timesteps 1 to 7 are 63.48, 63.82, 64.04, 64.16, 64.25, 64.31, and 64.41 in units of 10^5 s. The bottom panel shows the cooling wave travelling from the outside in at times 65.94, 68.42, 73.19, 74.50, 75.58, 76.79, and 77.49 $[10^5\,\mathrm{s}]$. Taken from Mineshige & Osaki (1985) .

3.5 Outflow in cataclysmic variable systems

So far the accretion disk played the main role in the introduction parts, but for many CVs the situation is not as “easy” with the material from the secondary falling onto the primary only flowing nicely through an accretion disk. In some situations a substantial part of the infalling material can be lifted from the disk and “blown” away to outer space by a so-called accretion disk wind. Which observational and theoretical evidence there is for this and how such an outflow works will be presented in this section.

3.5.1 Spectral signatures of outflows

For dwarf novae double peak structures, spectral signatures of an accretion disk as described in Sec. 3.3, are mainly visible in quiescence. In an outburst they are replaced by other typical line profile structures, namely by profiles that are typical for outflowing gas. The *P Cygni profile*, named after the luminous blue variable P Cyg in whose spectrum it was first observed, is the most prominent spectral feature of an outflow. It consists of a blue-shifted absorption trough and the red part of the symmetric emission peak with respect to the rest wavelength of the line transition. A cartoon of the formation of P Cygni profiles is shown in Fig. 3.9. The formation of such a profile is readily understood. Photons from the star get absorbed by atoms in the outflow between the star and the observer, the bluish zone in Fig. 3.9. As those atoms move away from the star photons at blue-shifted wavelength are absorbed and the trough extends from the rest wavelength to the wavelength corresponding to the blueshift of the maximal velocity in the wind v_∞. The observer also sees emission from the wind, which are simply all the photons previously absorbed that got reemitted towards the observer. This emission is of course the same in all parts, the ones moving towards and the ones moving away from the observer, of the outflow, which results in a symmetric emission peak centered on the rest wavelength. Adding the blue-shifted absorption trough and the symmetric emission peak results in a P Cygni profile. Typical lines showing P Cygni profiles are the UV resonance lines C IV (Doublet: 1548 Å & 1550 Å), N V (Doublet: 1238 Å & 1242 Å), Si IV (Doublet: 1393 Å & 1402 Å), and O VI (Doublet: 1031 Å & 1037 Å).

Stellar winds are, at least in a first approximation, spherically symmetric and the P Cygni profiles do not depend on the inclination angle of the systems. However, this is not true for CVs, the exact shapes of the P Cygni profiles highly depend on the inclination of the CV and on the shape of the wind. In fact the profile shapes vary from only absorption via P Cygni like to pure

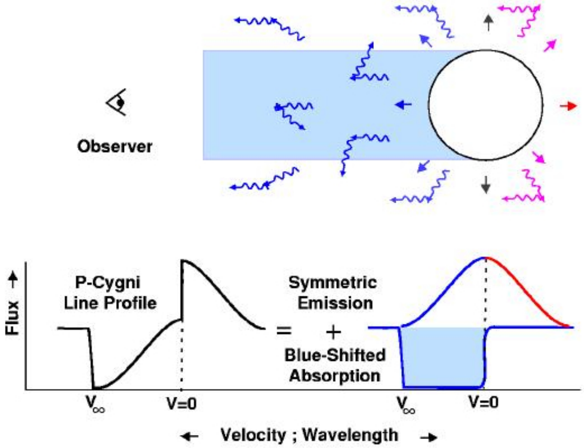

Figure 3.9: Formation of a P Cygni line profile. Blue-shifted and red-shifted photons in the outflow from the star are observed together and form a profile with a blue-shifted absorption trough and a red part of a symmetric emission peak. Illustration courtesy of Stan Owocki.

emission. An example of an observed C IV line with a P Cygni profile is shown in the IUE spectrum of T Leo in Fig. 3.10. The dependence on the inclination angle is a strong evidence that outflows in dwarf novae are not spherically symmetric, but are rather biconical in nature. More on wind theory, structure and observational signatures will be presented in the following sections.

3.5.2 Observational evidence of outflows in CVs

The first detection of outflows in CVs dates back to the late 1970ies and early 1980ies when blueshifted absorption troughs and P Cygni profiles in UV resonance lines were discovered (Heap et al., 1978; Cordova & Mason, 1982). More recent work shows that outflowing material has a strong influence on observations, not only in the “classical” UV wind lines, but also in other features.

For example the peculiar behavior of emission lines of SW Sex stars during eclipse can be interpreted in terms of a powerful disk wind (Honeycutt et al., 1986; Dhillon & Rutten, 1995). In novalike variable systems single peaked optical emission-line profiles can be interpreted in terms of a strong wind in-

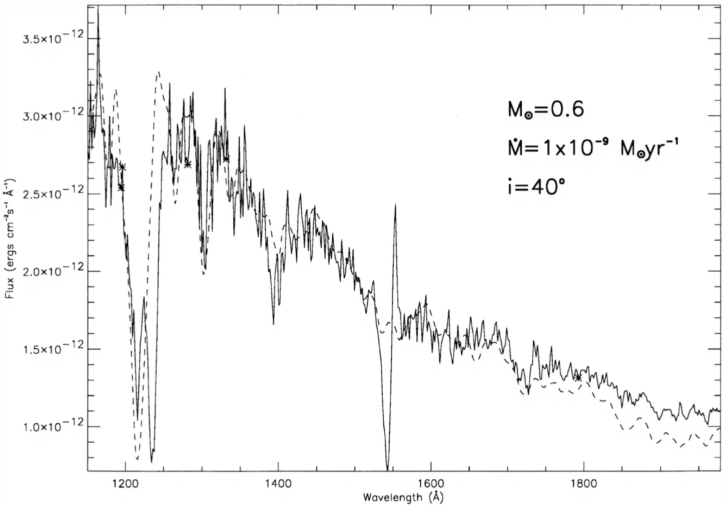

Figure 3.10: IUE low resolution spectrum of the medium inclination dwarf nova T Leo in outburst. Important to note is the P Cygni profile of the 1550 Å CIV resonance line. The dashed line is a fit from an accretion disk model. Taken from Belle et al. (1998).

duced velocity gradient in the emitting material (Murray & Chiang, 1996) and the greater part of all lines in the UV are formed in the outflow as well (Knigge et al., 1997). In addition to the typical P Cygni profiles found in UV lines, at least the spectra of one CV, BZ Cam, show such profiles in optical hydrogen and helium lines, too. These are most easily interpreted in terms of a wind (Ringwald & Naylor, 1998). The extreme UV spectrum of the dwarf nova U Gem in outburst appears to be dominated by strong wind features (Long et al., 1996) and *ASCA* (soft) X-ray observations of another dwarf nova, Z Cam, show direct evidence of a disk wind acting as a partially ionised absorber for X-rays in outburst (Baskill et al., 2001). For instance, Fig. 3.11 shows spectra of the novalike CV IX Vel and the dwarf nova Z Cam. Both spectra show a prominent P Cygni profile from the CIV 1550 Å resonance line as an evidence for wind being present in the system.

All this observational evidence leads to the conclusion that detailed models of CVs, at least in outburst, have to include outflows. Only by comparing models and observations it is possible to learn more about the mechanism and geometry of the outflow. The first models of such outflows were based on a wind theory originally developed to interpret the UV spectra of early-type stars (Mauche & Raymond, 1987; Drew, 1987; Vitello & Shlosman, 1988).

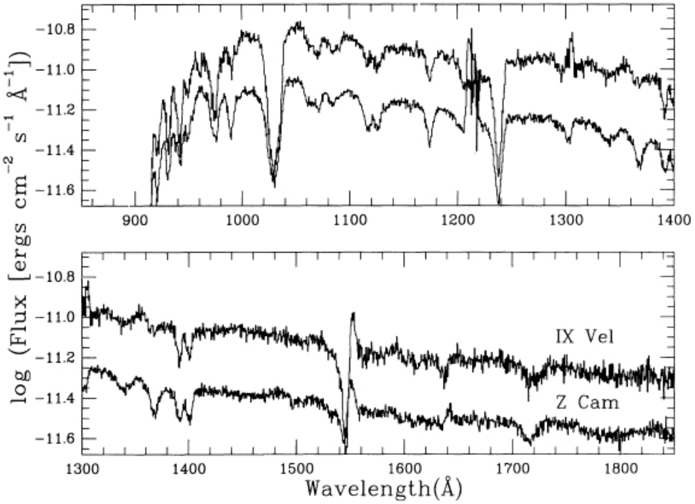

Figure 3.11: HUT spectra of the novalike CVs IX Vel and Z Cam as observed by Long et al. (1994). Note the prominent P Cygni profile of the 1550 Å C IV resonance line.

Studies with these models showed that the wind mass-loss rate amounts to approximately 10% of the disk accretion rate. In addition, the winds are strongly affected by rotation suggesting an origin in the rapidly rotating inner disk. Together with the observational fact that wind effects on the spectra are dependent on the system's inclination this led to the conclusion that the outflows in high-state CVs must be biconical disk winds. A second generation of models (Shlosman & Vitello 1993 (hereafter SV), Knigge et al. 1995 (hereafter KWD)) investigated such a biconical wind structure more closely in a Monte Carlo radiative transfer context. Both of these kinematical models are used in this work and described more closely in Sec. 4.2.

In order to present a more solid theoretical foundation of accretion disk winds an introduction to the hydrodynamics of such a wind is given in the next section.

3.6 Hydrodynamics of accretion disk winds

Hydrodynamic models of disk winds have only recently been developed by Pereyra et al. 1997; Proga et al. 1998, 1999; Feldmeier & Shlosman 1999 (hereafter FS); Feldmeier et al. 1999 (hereafter FS2). Thorough theoretical understanding of disk winds is hampered by the intrinsic multidimensionality of the system and the richness of physical processes necessary for treating the hydrodynamics of the outflow in a realistic way. Processes suggested as a driving mechanism for the outflow are, e.g., magnetic torques, X-ray disk irradiation, and line radiation pressure. Disks in non-magnetic CVs show spectra that are very similar to that of O, B, and Wolf-Rayet stars in their respective spectral peak, which is in all cases in the (far-) UV. In particular, the observed wind features are very similar, suggesting that the driving mechanism is also similar. For O, B, and Wolf-Rayet stars it is commonly agreed that their winds are driven by radiation pressure. Thus we expect that winds from CVs are also driven by radiation pressure in spectral lines, so-called line driving: the photons that are absorbed by atmospheric gas originate (mostly) in the accretion disk, hence transmit an outwardly directed momentum. Re-emission is isotropic, and transmits no net momentum. The theory of line driving through an ensemble of spectral lines was developed in a landmark paper by Castor et al. 1975 (hereafter CAK). The derivations are somewhat tedious, and we give only some heuristic arguments in the following, and refer to the literature for the details.

The novel and unique fact in line driving is that the force depends nonlinearly on the velocity gradient. Since the force determines the velocity (and therefore the velocity gradient), we have here immediately a bootstrap (or self-feedback) mechanism leading to an eigenvalue problem. In the following we explain that the mass-loss rate of the wind is determined as such an eigenvalue, which can be understood from the (Laval) nozzle analogy of the stellar wind.

3.6.1 The line force

The force per gram (or acceleration) resulting from absorption by radiation is given by (see textbooks by Mihalas 1978 and Chandrasekhar 1960)

$$\vec{g}^{\,\mathrm{L}}(\vec{r}) = \kappa(\vec{r})\vec{F}^{(\mathrm{abs})}(\vec{r})\,/c\,, \tag{3.32}$$

where κ is the mass absorption coefficient (units cm^2/g), assumed to be constant with respect to $\vec{r}$ in the following, $\vec{F}$ is the absorbed radiative flux, and c is the speed of light. A single spectral line absorbs flux in an interval of order $F_\nu \Delta\nu_D$, where ν is the line frequency, and $\Delta\nu_D$ is the Doppler width of the line. The fraction of the radiative flux *absorbed* by the gas at $\vec{r}$ is described by the *escape probability* (to be calculated for each line separately),

$$\beta_\nu = \frac{1 - e^{-\tau}}{\tau}\,, \tag{3.33}$$

with the line optical depth τ and it is indeed $0 \leq \beta_\nu \leq 1$, as must hold for a probability. Therefore, for a single spectral line,

$$\vec{g}^{\mathrm{L}} = \frac{\kappa \Delta\nu_D}{c}\, \vec{F}_\nu\, \frac{1-e^{-\tau}}{\tau}\,. \tag{3.34}$$

The frequency integral of $\Delta\nu_D F_\nu$ over all spectral lines, assuming that lines cover the flux distribution uniformly, gives the frequency-integrated flux F from the accretion disk (and a multiplicative constant),

$$\vec{g} \sim \kappa \vec{F}\, \frac{1-e^{-\tau}}{\tau}\,. \tag{3.35}$$

Hence for (very) optically thick lines, $\tau \gg 1$, the force scales as $\frac{\kappa F}{c}\frac{1}{\tau}$, and for optically thin lines, $\tau \ll 1$, as $\frac{\kappa F}{c}$, or $\frac{\kappa F}{c}\frac{1}{\tau^0}$. The ingenious idea of CAK was that the line force from a mixture of thin and thick lines should then scale as

$$\vec{g}^{\mathrm{L}} \sim \vec{F}\tau^{-\alpha}\,, \tag{3.36}$$

where $0 < \alpha < 1$. Note that F and τ depend on the position in the wind. Furthermore, τ refers here to some artificial reference line. CAK used as such a line that has the same mass absorption coefficient as Thomson scattering, which lead to large confusion over the years. Meanwhile, reference to the strongest line occurring in the flow (symbol κ_0) is preferred. The latter equation can be derived strictly analytically (including the forefactor), by assuming a power law distribution of lines in frequency and opacity space, leading to equations including the complete gamma function.

The *optical depth* is calculated in the so-called *Sobolev* approximation, see Sec. 4.1.6 for details. We consider for simplicity only the optical depth in radial direction,

$$\tau(r) = \kappa \int_{R_*}^{r} \mathrm{d}r'\, \rho(r')\phi(x - v(r')/v_{\mathrm{th}})\,. \tag{3.37}$$

Here, $x = (\nu - \nu_0)/\Delta v_D$ is the normalised frequency variable, i.e. the distance from line center in units of the Doppler width, and v_{th} is the most probable thermal speed of the absorbing species (assumed to be constant here). If the velocity law of the wind is monotonic, the variable substitution

$$r' \rightarrow \tilde{x}' = x - v(r')/v_{\mathrm{th}} \tag{3.38}$$

is allowed, where $\tilde{x}$ is the comoving frame frequency. Moreover, if the wind is steeply accelerating, the absorption of photons of a given frequency takes place in a (very) narrow radial regime, where the atoms are Doppler-shifted to just the right amount that a certain line transition is in resonance with these photons. We assume that this resonance location is identical to the radius r under consideration. In this case, the density and the velocity gradient can be assumed to be constant over this resonance layer (also called Sobolev zone), and taken in front of the integral,

$$\tau(r) = \frac{\kappa v_{\rm th}\rho(r)}{{\rm d}v(r)/{\rm d}r} \int_{\tilde{x}}^{\infty} d\tilde{x}'\phi(\tilde{x}') \,. \tag{3.39}$$

Here, it was assumed that the speed in the photosphere is close to zero. Furthermore, since the line profile function gives only a contribution around $\tilde{x} - v/v_{\rm th} \approx 0$, we have that $\tilde{x}_* = x \approx v/v_{\rm th} \gg 1 \equiv \infty$, where the latter relation holds for a Doppler profile function $\phi(x) \sim e^{-x^2}$. Equation (3.39) is written as

$$\tau(r) = \tau_S \Phi(\tilde{x}) \,, \tag{3.40}$$

with Sobolev optical depth $\tau_S = \kappa v_{\rm th}\rho/({\rm d}v/{\rm d}r)$, and Φ is essentially a step function, i.e. the Heaviside function (more precisely, for a Doppler profile function, Φ is the error function).

The line force at r arises from those lines that have their resonance layer at this location, hence $\Phi \equiv 1$, and the line force for the radial direction under consideration becomes

$$g^{\rm L} \sim F \left(\frac{dv/dr}{\rho}\right)^{\alpha} \,. \tag{3.41}$$

A corresponding reasoning for the general vector line force gives

$$\vec{g}^{\rm L} \sim \frac{1}{\rho^{\alpha}} \int {\rm d}\Omega I_n \hat{n} \Big[\big(\hat{n}\cdot\nabla\big)\big(\hat{n}\cdot\vec{v}\big)\Big]^{\alpha} \,, \tag{3.42}$$

where the expression in square brackets is the differential of the projected velocity along the photon trajectory $\hat{n}$.

The Euler equation for a stationary accretion disk wind is then

$$(\vec{v}\cdot\nabla)\vec{v} = -\vec{g}(\vec{r}) + \vec{g}^{\rm L}(\vec{r}) \,. \tag{3.43}$$

We neglect the thermal pressure force since it is tiny compared to the gravity and line force. Since the line force depends on the velocity gradient, this equation adopts a “transonic” form like that for the Laval nozzle or Parker’s solar wind (Parker, 1958, 1960). The corresponding critical point, though, is not one for sound waves, but for a new radiative(-acoustic) wave mode, so-called Abbott waves (Abbott, 1980). Quite uniquely, since g^{L} depends on dv/dr *non-linearly*, this critical point also fixes the mass-loss rate of the line driven wind as an eigenvalue of the Euler equation. There is a deep link between transonic flow, critical points, and nozzle flow, which was first realised for line driven winds by Abbott (1980). Even more than that, for line driven winds from accretion disks, this nozzle analogy (and the maximisation of mass-loss rate) even determines the flow geometry.

We make the simplifying assumption that the line force (3.42) can be approximated by

$$\vec{g}^{\mathrm{L}} \sim \vec{F} \left(\frac{dv_\lambda/d\lambda}{\rho} \right)^{\alpha} . \tag{3.44}$$

Here, the velocity gradient was taken out of the integral in (3.42), and the remaining integral is the radiative flux. This corresponds to applying the mean value theorem of calculus. In our case, however, $I_n \hat{n}$ was left under the integral, i.e. we replaced the trivial $\int d\omega = 4\pi$ of the mean value theorem by what should be a good approximation to the integral: the streamline should roughly align with the flux direction. By taking the velocity derivative out of the integral, a specific value of this quanity is fixed, which can only result from differentiation along a specific direction $\hat{\lambda}$. The latter does usually *not* coincide with the flux direction (the exception are cases of high symmetry, like stars).

We decompose the velocity field in a toroidal and poloidal component. The toroidal (azimuthal) velocity of the disk wind is fixed by assuming (i) Kepler rotation in the disk, and (ii) angular momentum conservation above the disk, where the latter is a good approximation for supersonic flow.

In the spirit of the Bernoulli equation, we introduce an arclength coordinate s along the poloidal component of the streamline of a wind particle. The Euler equation along the streamline is found by projecting (3.43) onto $\hat{v}$. We make the further simplifying assumption that $\hat{\lambda} = \hat{v}$, and also abbreviate $v' \equiv \mathrm{d}v/\mathrm{d}s$, giving

$$vv' = -g_s + CF_s[v'/\rho]^{\alpha} , \tag{3.45}$$

where g_s and F_s are the gravity and flux projections onto the streamline, and C is a constant.

Despite the many approximations already introduced, a further assumption is necessary: we replace the actual streamline of the flow by a simple geometric curve of pre-specified shape; mostly by a straight line. (Actually, over a non-magnetised disk, one expects a streamline that is outwards bent.) We keep the symbol v for the projected velocity. The 1-D Euler equation (3.45) is now used to make the nozzle analogy.

3.6.2 Flow nozzle analogy

We want to determine the location of the critical point in the wind. According to Abbott (1980) and FS the wind critical point occurs at the location where a generalised nozzle function has its minimum. This nozzle function is chosen in direct analogy to the Laval nozzle, where the flow undergoes sonic transition at the tube constriction. For reasons not yet fully understood, a line driven outflow tries to maximize the mass-loss rate (probably via some radiative “underpressure” in the outer wind, communicated to the photosphere via inwards propagating Abbott waves). The critical point is then the location in the wind where, at this maximum mass-loss rate, the radiation field can “just so” balance gravity.

The mass-loss rate leaving the disk in a ring of width $\mathrm{d}R$ at location R is

$$\mathrm{d}\dot{M} = 2\pi\, R\mathrm{d}R\, \rho v \cos\theta\,. \tag{3.46}$$

Here, θ is the angle of the poloidal streamline with the vertical direction, and the cosine accounts for the projection of v perpendicular to the disk. We assume $\alpha = 1/2$ in the following, which is a good approximation for thin winds from accretion disks (see Puls et al. 1996), and allows for an explicit algebraic solution of the nozzle equation. Replacing the density in (3.45) using (3.46),

$$vv' - CF_s\sqrt{\frac{2\pi R\mathrm{d}R\cos\theta}{\mathrm{d}\dot{M}}}\,\sqrt{vv'} + g_s = 0\,. \tag{3.47}$$

Solving this quadratic equation,

$$vv' = g_s\frac{n(s)}{\mathrm{d}\dot{M}}\left[1 \pm \sqrt{1-\frac{\mathrm{d}\dot{M}}{n(s)}}\right]^2\,, \tag{3.48}$$

with the *nozzle function* n given by

$$n(s) = \frac{1}{2}\pi C^2 R\mathrm{d}R\cos\theta\,\ \frac{F_s^2(s)}{g_s(s)}\,. \tag{3.49}$$

The plus and minus sign in (3.48) correspond to so-called steep and shallow wind solutions. Steep wind solutions are everywhere faster than Abbott waves, and shallow solutions are everywhere slower than Abbott waves, and correspond, therefore, to subsonic solar wind breezes. A continuous transition from an initially shallow to an outer steep solution is only possible when the discriminant D in (3.48) becomes zero. If $\mathrm{d}\dot{M}$ is small, $D > 0$ everywhere, and a switch from shallow to steep solutions is nowhere possible in the wind. If, on the other hand, $\mathrm{d}\dot{M}$ is large, $D < 0$ occurs in a finite interval of the streamline; the wind is then *overloaded* and has to decelerate (we do not consider here the unique solution to the Euler equation for $v' < 0$). Therefore, the critical point with a switch from a shallow to a steep solution determines the maximum possible mass-loss rate $\mathrm{d}\dot{M}$ of the wind that can everywhere be supported by the radiation field acting against gravity, especially at the critical point itself. This shows the deep analogy of the line driven flow with the Laval nozzle flow.

In summary, we *maximize* $\mathrm{d}\dot{M}$ up to such a value that at the *minimum* of $n(s)$ along the streamline $1 - \mathrm{d}\dot{M}/n = 0$ holds.

The unique parameter on which $\mathrm{d}\dot{M}$ depends is the inclination angle θ of the wind cone with the disk normal. We therefore search for the tightest constriction (as function of s) of the widest nozzle (as function of θ), and both the location s_c of the critical point and the inclination θ_c of the wind cone in the disk are determined via the relation

$$n(s_c;\theta_c) = \min_s \max_\theta n(s;\theta)\,. \tag{3.50}$$

Geometrically, the wind mass-loss rate is thus determined by the value of the nozzle function n (or, equivalently, of F_s^2/g_s) at its *saddle* point,

$$\mathrm{d}\dot{M}_c = n(s_c;\theta_c)\,. \tag{3.51}$$

3.6.3 Critical point of Euler equation

The above considerations for the simplified case $\alpha = 1/2$, which can be solved algebraically, shall now be generalised to general α. Introducing the mass-loss rate (3.46), the Euler equation (3.45) becomes, introducing $w' = vv'$,

$$w' + g_s - \frac{CF_s}{\mathrm{d}\dot{M}^\alpha}\frac{(2\pi R\mathrm{d}R\cos\theta)^\alpha}{g_s^{1-\alpha}}g_s^{1-\alpha}w'^\alpha = 0\,, \tag{3.52}$$

where w', g_s, and $g_s^{1-\alpha}w'^\alpha$ all have the dimension of acceleration. For general α, this equation can no longer be solved algebraically. Nevertheless, the nozzle analogy can be fully adopted. From Eq. (3.51), the mass-loss rate

$\mathrm{d}\dot{M}$ and the nozzle function n have the same dimension. Hence we re-write (3.52) as

$$w' + g_s - \eta \frac{n^\alpha}{\mathrm{d}\dot{M}^\alpha} w'^\alpha g_s^{1-\alpha} = 0\,, \tag{3.53}$$

with nozzle function

$$n = \frac{1}{\eta^{1/\alpha}}\, 2\pi R \mathrm{d}R \cos\theta \frac{(CF_s)^{1/\alpha}}{g_s^{(1-\alpha)/\alpha}}\,. \tag{3.54}$$

The parameter η was introduced in order to fulfill Eq. (3.51) also for general α.

The solution “topology” of Eq. (3.53) can be understood from Figure 3.12 (adopted from Fig. 3 in Cassinelli 1979), which shows the line force g^{L} as function of w', for three selected values of the mass-loss rate. These curves are *concave* from below since $\alpha < 1$. This driving force is in balance with the two retarding forces (plotted positive in the figure), inertia w' and gravity g_s. Note that the inertial force is a 45° diagonal in the diagram, and that g_s is a constant, since a fixed yet arbitrary location is considered. The retarding and driving forces cross at either zero or one (open square in the diagram) or two points (closed squares). The latter two correspond to the so-called shallow and steep solutions. If the mass-loss rate adopts the critical CAK value, the shallow and steep solution merge into one. For still higher mass-loss rates, no real solution is possible, and the wind is called overloaded.

At the critical point (subscript “c”), one has therefore

$$\frac{\partial g^{\mathrm{L}}}{\partial w'_c} = 1 = \frac{\partial}{\partial w'_c}(w' + g_s)\,, \tag{3.55}$$

or

$$\frac{\partial}{\partial w'_c}(w' + g_s - g^{\mathrm{L}}) = 0. \tag{3.56}$$

This is the famous CAK critical-point condition. Note that the Euler equation is $w' + g_s - g^{\mathrm{L}} = 0$, at *every* point, hence also at the critical point. This set of two equations (at the critical point) is readily solved, giving the well-known CAK relations

$$w'_c = \frac{\alpha}{1-\alpha} g_{s,c}\,, \tag{3.57}$$

and

$$\eta \left(\frac{n_c}{\mathrm{d}\dot{M}}\right)^\alpha = \frac{1}{\alpha^\alpha (1-\alpha)^{1-\alpha}}\,. \tag{3.58}$$

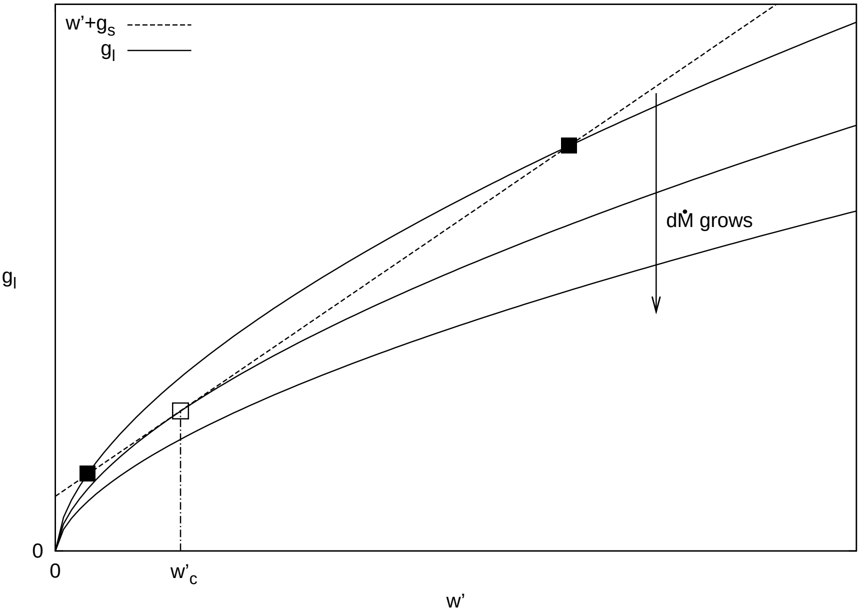

Figure 3.12: The solution "topology" of the Euler equation, adopted from Cassinelli (1979). w' and g_s are the two retarding forces, plotted positive, whose sum crosses the driving force g^{L} at either zero, one (open square) or two points (closed squares). The line force is plotted for three values of the mass-loss rate. The critical point w'_c is marked.

Requiring $n_c = \mathrm{d}\dot{M}$, we arrive at

$$\eta = \frac{1}{\alpha^{\alpha}(1-\alpha)^{1-\alpha}}\,, \tag{3.59}$$

thus the nozzle function is

$$n = \alpha(1-\alpha)^{(1-\alpha)/\alpha}\, 2\pi R \mathrm{d}R \cos\theta \frac{(CF_s)^{1/\alpha}}{g_s^{(1-\alpha)/\alpha}}\,. \tag{3.60}$$

This reproduces indeed the simple $\alpha = 1/2$ case from before. The unique critical wind solution is then determined by the (appropriate) saddle point of the function

$$n(s,\theta) \sim \cos\theta \left(\frac{F_s}{g_s^{1-\alpha}}\right)^{1/\alpha}\,. \tag{3.61}$$

3.6.4 Nozzle function for g_s and F_s of a disk wind

The effective gravitational acceleration (gravity minus centrifugal force) above a Keplerian accretion disk along the s-streamline is given by (M is the white dwarf mass)

$$g_s(s) = -GMR\left(\frac{s/R+\sin\theta}{[R^2+2Rs\sin\theta+s^2]^{3/2}} - \frac{\sin\theta}{[R+s\sin\theta]^3}\right)\,. \tag{3.62}$$

Closed algebraic expressions for the radiative flux can only be given in highly simplified cases for the radial temperature run in the disk, e.g. for an isothermal disk and for $T \sim r^{-1/2}$, see FS. The disk with a $T \sim r^{-1/2}$ temperature stratification is called *Newtonian* in the following. Fortunately, the radiation field from a narrow ring emitting as a black body can be calculated analytically, and thus the disk emission be obtained from a one-dimensional numerical integration. The nozzle function obtained from this, along with the relevant saddle points, are shown in Fig. 6 of FS, and the relevant eigenvalues for θ are given in their Table 1. Note that $\lambda_{\rm cr} = 90^\circ - \theta_c$ is tabulated there. The value of the nozzle function itself at the saddle, i.e. the critical mass-loss rate, is given in the same table, and shown as function of footpoint radius in Fig. 3.13. Note that in Shlosman & Vitello (1993), the mass-loss rate from a disk ring is taken as proportional to the ring area $R\mathrm{d}R$. This is a severe approximation, and the current eigenvalue or nozzle analysis allows to *derive* the mass-loss rate from a ring as function of its radius.

The wind starts roughly at three white dwarf radii from disk center. Further in, details of wind launching are presently unknown due to the complexity of the disk boundary layer, disk corona, etc. Interestingly, in the wind models of FS adopting a Shakura & Sunayev disk, no appropriate saddle point of the nozzle function and hence no critical wind solution is found inside ≈ 3 white dwarf radii.

As for the outer wind termination radius in the disk, we do not follow the conclusion in FS2, that the total mass-loss rate is dominated by the inner wind up to, say, seven white dwarf radii, and that regions further can be neglected. Instead, Fig. 3.13 indicates that the region in the disk from ten to thirty white dwarf radii should contribute roughly one third of the total mass-loss rate.

For $r > 5R_{\rm WD}$, FS2 find a power law dependence

$$\mathrm{d}\dot{M}/\mathrm{d}R = R^{-\lambda}\,. \tag{3.63}$$

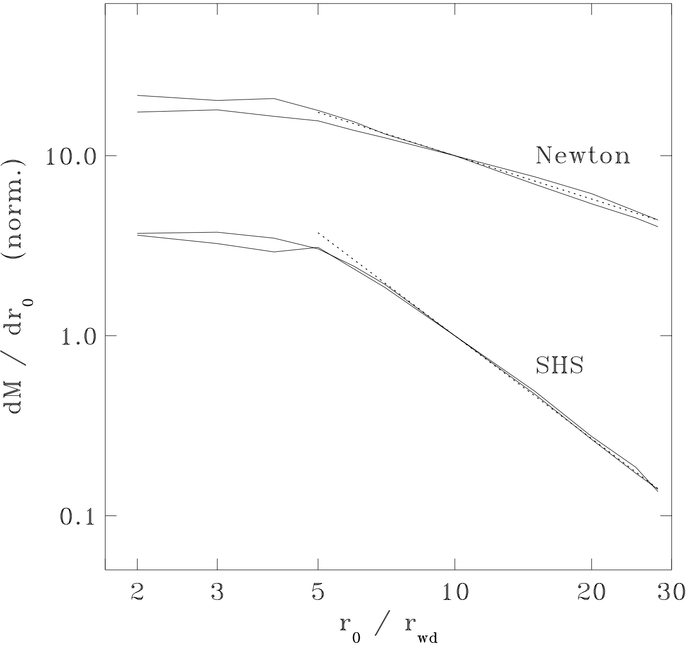

Figure 3.13: Mass-loss rate per disk annulus, $\mathrm{d}\dot{M}/\mathrm{d}r_0$, as a function of footpoint radius. Data for $\alpha = 2/3$ and $\alpha = 1/2$ was used for both Newtonian and SHS disks. Fits with $\mathrm{d}\dot{M}/\mathrm{d}r_0 \propto r_0^{-1.9}$ (SHS) and $\propto r_0^{-0.8}$ (Newtonian) are shown as dotted lines. Curves are nomalised at $r_0/r_{\mathrm{WD}} = 10$. This is Fig. 2 from FS2.

A rough value for λ can be estimated from Eq. (3.60), by considering the R-dependence of the nozzle function in the near disk regime ($s \to 0$). Obviously then, $g \sim R^{-2}$, and $F \sim I^4 \sim R^{-2} \dots R^{-3}$, where in the latter relation the outer regions of either a Newtonian or SHS disk are assumed. From (3.60), $\mathrm{d}\dot{M}/\mathrm{d}R \sim R^{-1}$ follows [in FS2: $R^{-0.8}$] for the Newtonian disk and either $\alpha = 1/2$ or $2/3$; and $\mathrm{d}\dot{M}/\mathrm{d}R \sim R^{-3}$ resp. $R^{-2.5}$ for the SHS disk and $\alpha = 1/2$ resp. $2/3$ [in FS2: $R^{-1.9}$ for both α]. In our wind models, we adopt the values for λ from FS2.

As for the critical angle θ_c, it varies only marginally in the wind launching area. We adopted the values for the different disk models calculated by FS as shown in their Table 1. For $r_0 \approx 3\,R_{\mathrm{WD}}$ they find $\theta_c = 25^\circ \dots 27^\circ$ and for the outer edge of the wind at $r_0 \approx 30R_{\mathrm{WD}}$ they find $\theta_c = 33^\circ \ldots 39^\circ$. The influence on the resulting spectra of such a minor variation in θ_c is negligible compared to other uncertainties in the model. We therefore adopt a simple linear variation of θ_c from 25° to 35° as r_0 varies from $3\,R_{\mathrm{WD}}$ to $30\,R_{\mathrm{WD}}$.

A short summary of the actual wind model used in our calculations as derived from the nozzle function analysis is given in Sec. 4.2.3

Disk, Outflow and Dwarf Novae – summary

Disks in CVs

- geometrically thin
- gas rotates Keplerian
- viscosity can be parametrised by α
- MRI as most promising theory of viscosity
- double peak line profile structure as spectral evidence

Dwarf novae

- brightening by several magnitudes in semi-periodic outbursts
- enhanced mass flow due to enhanced viscosity
- disk instability model (DIM) for enhancing viscosity
- thermal instability triggers outburst
  - local limit cycle due to H ionisation triggers disk
  - inside-out or outside-in heating waves
  - outside-in cooling waves

Outflow

- P Cygni line profiles as spectral evidence for outflow
- biconical wind from disk in high state
- wind follows streamlines
- hydrodynamical models
  - critical point of Euler equation
  - determination of mass loss & streamline angle

CHAPTER 4

Techniques

"An expert is a man who knows some of the worst mistakes which can be made, in a narrow field."
[Niels Bohr]

4.1 Radiative transfer

For processing the radiation from the accretion disk through the outflow we need to introduce a description for the radiation field and radiation processes. This includes the calculation of occupation numbers, electron densities, and opacities. All the necessary quantities are introduced in this section. Naturally this section is a rather compact introduction, for a full account on radiative transfer see e.g. Mihalas (1978).

4.1.1 The radiation field

In the case of a low $\vec{B}$-field polarisation can be neglected and the radiation field, see Fig. 4.1, is completely described by the specific intensity I_ν, which is a function of direction $\hat{n}$, frequency ν, position $\vec{r}$, and time t. The specific intensity is defined as the energy ΔE transported during the time Δt in the frequency intervall $[\nu, \nu + \Delta\nu]$ through the surface element $\Delta\sigma = \Delta A \cos\theta$ into the solid angle $\Delta\omega$ in the direction $\vec{n}$:

$$I_\nu = I(\vec{n}, \nu, \vec{r}, t) = \frac{\Delta E}{\Delta\sigma \Delta\nu \Delta\omega \Delta t} \,. \tag{4.1}$$

We consider only stationary cases in the following and omit t. In order to describe the radiation field more properly the so-called *moments of intensity*,

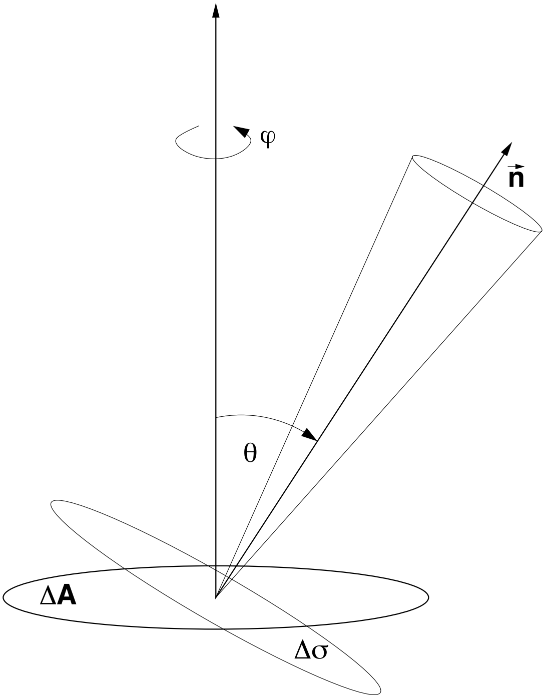

Figure 4.1: Schematic sketch of the parameters defining the radiation field. Taken from Hammer (2004).

integrals of the specific intensity over the solid angle $\mathrm{d}\omega$, are useful to define. Starting with the *zeroth moment* , the mean intensity, which is defined as

$$J_\nu(\vec{r}) = \frac{1}{4\pi} \oint_{4\pi} \mathrm{d}\omega \, I_\nu(\vec{n}, \vec{r}) \, . \tag{4.2}$$

The *radiation flux*, or *first moment*, is a vector defined as

$$\vec{\mathcal{F}}_\nu(\vec{r}) = \oint_{4\pi} \mathrm{d}\omega \, I_\nu(\vec{r}, \vec{n}) \, \vec{n} \, , \tag{4.3}$$

and is connected to the *Eddington flux* $\vec{H}_\nu$ and to the *astrophysical flux* $\vec{F}_\nu$ via simple scaling relations

$$\vec{H}_\nu = \frac{1}{4} \vec{F}_\nu = \frac{1}{4\pi} \vec{\mathcal{F}}_\nu \, . \tag{4.4}$$

The units for both moments are $\mathrm{erg\,cm^{-2}\,s^{-1}\,Hz^{-1}}$.

The energy density in a volume ΔV at $\vec{r}$ can be calculated with (4.2) as $u_\nu(\vec{r}) = \dfrac{4\pi}{c} J_\nu(\vec{r})$ where an integration over all frequencies yields

$$u(\vec{r}) = \frac{4\pi}{c} \int \mathrm{d}\nu \, J_\nu(\vec{r}) \,, \tag{4.5}$$

the total radiation energy contained in ΔV.

4.1.2 Transfer equations

In order to calculate a synthetic spectrum it is necessary to solve the equation of radiative transfer for the system under consideration. It describes the modification of the specific intensity in an infinitesimal length $\mathrm{d}\vec{s}$ along a ray

$$\frac{\mathrm{d}I_\nu(\vec{r})}{\mathrm{d}\vec{s}} = \eta_\nu(\vec{r}) - \kappa_\nu(\vec{r}) \cdot I_\nu(\vec{r}) \,, \tag{4.6}$$

where $\eta_\nu(\vec{r})$ is the emissivity of the gas at position $\vec{r}$ at frequency ν and $\kappa_\nu(\vec{r})$ the opacity. The specific intensity at $\vec{r} + \mathrm{d}\vec{s}$ is thus the specific intensity at $\vec{r}$ to which the intensity emitted in $\mathrm{d}\vec{s}$ gets added and from which a part proportional to the specific intensity itself is absorbed. We can define the *source function* as $S_\nu \equiv \eta_\nu / \kappa_\nu$ and use this in (4.6) to get

$$\frac{\mathrm{d}I_\nu(\vec{r})}{\mathrm{d}\vec{s}} = \kappa_\nu(\vec{r})[S_\nu(\vec{r}) - I_\nu(\vec{r})] \,. \tag{4.7}$$

This differential equation of radiative transfer is highly non-trivial to solve, as the source function also depends on the radiation field. An iteration scheme is necessary. On the other hand the underlying geometry is also important for finding a solution to the radiative transfer problem. For plane-parallel or spherically symmetric situations solution schemes exist. One is the use of the so called short-characteristics method (Olson & Kunasz, 1987) with the accelerated lambda iteration method. For a review see Hubeny (2003). In this work, however, the underlying geometry is cylinder symmetric and the velocity field considered for the accretion disk wind has contributions of all three vector components. Therefore it is necessary to solve the radiative transfer equation in three dimensions. We apply a Monte Carlo method, which will be presented in more detail in Sec. 4.3, to solve the transfer equation.

4.1.3 Opacity and emissivity

For all solution methods of the radiative transfer equation (4.6) the opacity $\kappa_\nu(\vec{r})$ and emissivity $\eta_\nu(\vec{r})$ are needed. Three different types of atomic transitions need to be considered to describe the whole picture of *true absorption*, *true emission* and *scattering*, from which the opacity and emissivity can be calculated. An absorption process removes a photon from the photon field and transfers its energy to the plasma. An emission is the inverse process where energy from the plasma is taken to add a new photon to the field. A scattering process on the other hand does not transfer energy but only changes the direction in which the photon travels[1].

Bound-bound transitions are transitions in which a bound electron on the initial energy level E_i absorbs a photon which transfers the electron to a more energetic but still bound final energy level $E_\mathrm{f} > E_\mathrm{i}$. If the de-excitation is collisional the whole transition is an absorption process. However, if the de-excitation is a radiative de-excitation the bound-bound transition is a scattering process, as are scattering processes on free electrons, e.g. Thomson scattering.

Bound-free transitions are transitions where a bound electron absorbs a photon with enough energy that E_f is more energetic than the ionisation energy of the atom, the electron is no longer bound and becomes a free electron in the plasma adding the difference of the photon energy to the ionisation energy as kinetic energy to the plasma. This process is called *photoionisation*. The inverse process is called recombination and removes the kinetic energy plus the binding energy of the final state E_f from the plasma.

Free-free transitions are transitions where the kinetic energy of an electron moving freely in the field of an ion is changed. A free-free absorption adds kinetic energy to the electron, whereas an electron can also loose kinetic energy via *bremsstrahlung*.

In order to calculate the overall opacity and emissivity at a point $\vec{r}$ for the frequency ν we have to consider and sum all transitions at this frequency for all chemical elements involved in the model. Both can be calculated from a product of the cross section $\sigma(\nu)$ and the occupation number n of the involved transitions. E.g. for the opacity consider

---

[1] Because of the finite line width involved in the process this is not quite true, but still is a good assumption.

$$\kappa_\nu = \sigma(\nu) n_{\text{low}} \,, \tag{4.8}$$

where n_{low} is the occupation number of fitting absorbing states. The cross section can be separated in $\sigma(\nu) = \sigma_0 \phi(\nu)$ with a constant part σ_0 and a profile function $\phi(\nu)$. Profile functions have to be chosen according to physical situation. The line profiles can be broadened e.g. due to thermal motion (*Doppler broadening*) or the Stark effect (*quadratic* or *linear Stark broadening*).

Also included in the opacity calculations is Thomson scattering on free electrons.

4.1.4 Occupation numbers

As it was shown in the last subsection a calculation of opacity and emissivity is only possible if we know the occupation numbers. With the assumption of local thermodynamic equilibrium (LTE) these are only a function of the local density $\rho(\vec{r})$ and local temperature $T(\vec{r})$, completely described by the *Boltzmann* and *Saha* equations. Excitations within an ionisation stage are given in terms of population numbers n in those stages and can be calculated via the Boltzmann equation

$$\frac{n_i}{n_j} = \frac{g_i}{g_j} \exp^{-(E_i - E_j)/kT} \,, \tag{4.9}$$

for the bound states i, j with the statistical weights g, the Boltzmann constant k, and the excitation energies E. Occupation numbers for states in different ionisation stages can be calculated with the Saha equation

$$\frac{n_{\text{up}}}{n_{\text{low}}} = \frac{2}{n_{\text{e}}} \left(\frac{2\pi m_{\text{e}} kT}{h^2} \right)^{\frac{3}{2}} \frac{g_{\text{up}}}{g_{\text{low}}} \exp^{-(E_{\text{up}} - E_{\text{low}})/kT} \,, \tag{4.10}$$

with the electron number density n_{e}, the electron mass m_{e}, and Planck constant h, where n_{up} and n_{low} are the occupation numbers of two levels in different ionisation stages.

In a stationary accretion disk wind scenario temperature and density are given by the wind model, see Sec. 4.2 for a description of the models used in this work, the electron density, however, has to be calculated with the aid of the Saha equation in a Newton-Raphson iteration scheme.

4.1.5 Remarks on LTE

Local thermodynamic equilibrium is a state where local processes such as collisions, bring the medium in a state in which each local area is in thermodynamic equilibrium. For the heavy particles in a gas to be in LTE the radiation field need not to be local, e.g. the radiation field can be obtained from solving a non-local transfer equation. LTE breaks down in cases where the mean-free path a heavy particle travels before thermalizing is longer than the local area the particle should thermalize with, is wide. For cold and dense media collisional processes dominate and the LTE assumption is indeed satisfied.

In the case of hot and thin media, however, radiative processes with their non-local character dominate, and the LTE assumption breaks down. To correctly calculate the occupation numbers in this *non-LTE* case we have to consider all radiative and collisional (de-)excitation processes of all states involved in the model. This would be done with the so-called *statistical equations*, which need some kind of iteration scheme to be solved, as the solution depends on the radiation field, which in return depends on the occupation numbers. However, such a sophisticated iteration scheme is beyond the scope of this work, only a rather simple iteration scheme for temperature corrections is used. Despite the fact that the hot and thin accretion disk wind in cataclysmic variables should be, physically correct, treated in non-LTE, our work uses only LTE and leaves the full non-LTE treatment for a future upgrade of the code.

4.1.6 Opacities in moving media

Calculation of opacity and emissivity in moving media is not as straightforward as in static media. Necessary Doppler shifts make both anisotropic in the lab frame. Two methods for dealing with radiative transfer have been established, the *Sobolev approximation* and the *co-moving frame method*.

It was first realised by Sobolev (Sobolev, 1960) that the line transfer problem in moving media can be simplified. The method was later generalised by Rybicki & Hummer (1978, 1983). The idea is that along a ray the intensity for frequency ν only changes at discrete *resonance points* where moving material has just the right Doppler shift to allow for absorption and emission at ν. The resonance condition for the line of sight velocity $v_l = \vec{v} \cdot \vec{n}$ is given by

$$\frac{\nu - \nu_0}{\nu_0} = \frac{v_l}{c}\,, \tag{4.11}$$

with ν_0 being the rest wavelength of the according transition. This approximation is only valid if the resonance region is very sharp. A condition for this can be derived with the estimate for the length of the resonance region

$$\Delta l = \frac{c}{\nu_0} \frac{\Delta\nu}{\left|\frac{\mathrm{d}v_l}{\mathrm{d}l}\right|}\,, \tag{4.12}$$

with $|\mathrm{d}v_l/\mathrm{d}l| \approx v_0/l_0$, where v_0 and l_0 are typical velocity and typical length scales in the medium under consideration. Assuming a line width $\Delta\nu$ only due to Doppler broadening $\Delta\nu = (\nu_0 v_{\mathrm{th}})/c$, with v_{th} the mean thermal velocity plus turbulent motion in the medium, the condition for the resonance length is given by

$$\frac{\Delta l}{l_0} \approx \frac{v_{\mathrm{th}}}{v_0}\,. \tag{4.13}$$

For macroscopic velocities much larger than thermal velocities we therefore have a sharp resonance region. In an accretion disk wind the thermal motion is of the order of several tens km/s, whereas the outflow velocity is of the order of several thousands km/s, thus the assumption of a sharp resonance region is satisfied. The same is true for winds from O and Wolf-Rayet (WR) stars.

Using the knowledge that interaction can only take place at the sharp *resonance surfaces* radiative transfer in moving media can be simplified and integral solutions are possible, even if the line of sight crosses several resonant surfaces. For more details about the method refer to Rybicki & Hummer (1978, 1983) or to Mihalas (1978). The Sobolev approximation is widely and with some success used for O and WR winds as well as for accretion disk winds in CVs (Shlosman & Vitello, 1993; Long & Knigge, 2002) due to its elegance and simplicity. For hydrodynamic analysis of line-driven disk wind (Proga et al., 1998, 2002; Feldmeier et al., 1999; Feldmeier & Shlosman, 1999) the Sobolev approximation is a necessity, as the validity of the Sobolev theory is essential for the CAK formalism (Castor et al., 1975).

However there are some limitations. Multiple scattering in the resonance region is neglected, there is only one interaction per resonance surface. In wind situations with a non-monotonic velocity law Sobolev calculations are still feasible, but get more complicated. As the resonance surfaces are taken to be sharp, physical quantities are assumed to be constant on the resonance surface. More realistic is the assumption of a finite resonance region in which physical quantities are allowed to change. In cases where more effects like line overlap, or wind clumping have to be considered, it is better to drop the Sobolev approximation and adopt accurate methods as co-moving frame calculations (see e.g. Hillier et al. 2003).

This method is based on a transformation into the co-moving frame, the frame in which the local medium is at rest. Opacities and emissivities are isotropic in this frame, the anisotropy is taken care of by the frame transformation. Numerical integration of the radiative transfer equation, or integration of the opacities, with this method requires a frame transformation at every sampling point (see e.g. Knigge et al. 1995). Such a method is more expensive, but can reveal differences compared to the Sobolev method, e.g. comparison of co-moving frame methods and Sobolev methods for O and WR star winds yield differences in wind acceleration and clumping factors (Hillier et al., 2003; Gräfener & Hamann, 2005; Gräfener, 2007).

In a Monte Carlo context opacity calculations using a co-moving frame method are a tractable problem (Knigge et al., 1995), where the trade-off in run time with todays' computer power to the gained insight from comparison to older Sobolev results is of no question. We therefore implement a co-moving frame method in this work.

4.2 Wind Models

Two different kinematical models for accretion disk winds of cataclysmic variables have been introduced in literature (Shlosman & Vitello, 1993; Knigge et al., 1995). These have been implemented in this work as reference and comparison. Furthermore a hydrodynamical analysis of cataclysmic variable accretion disk wind by Feldmeier & Shlosman (1999) has been used as a basis for creating a new model to be used with Monte Carlo radiative transfer. In the following subsection these models will be introduced in a chronological order.

4.2.1 Shlosman & Vitello Model

The model described in this subsection was first intruduced by Shlosman & Vitello (1993). Throughout this work we will refer to this model as SV model. It was introduced as a first attempt to calculate UV wind lines in cataclysmic variables without assuming radial symmetry. Earlier work by Drew & Verbunt (1985), Drew (1987) and Mauche & Raymond (1987) have all assumed spherical wind emitted from the white dwarf. As described above (Chap. 1) it is evident, that cataclysmic variables, at least in outburst, must have a biconical outflow originating on the accretion disk. SV described such a wind in a straightforward way. The geometrical layout of their wind is shown in Fig. 4.2.

A biconical outflow in absence of any clumping or other effects such as a hot spot on the disk, can be described by assuming axial symmetry. With this assumption a cylindrical set of coordinates is the natural choice to describe the system. The z-axis is taken to be co-aligned with the rotation axis of the disk. The r- and θ-coordinates are the radial and azimuthal coordinates on the disk surface. We assume a geometrically thin accretion disk completely neglecting its z-dimension. Wind is launched from the disk in an area between $r_{\min}$ and $r_{\max}$ and is described in intersection free streamlines. Those streamlines are three-dimensional helices laying on cones with constant opening angles θ. The opening angle of the cones depend on the initial radius where the streamline is launched from,

$$\theta = \theta_{\min} + (\theta_{\max} - \theta_{\min})x^{\gamma}\,. \tag{4.14}$$

Where $x := (r_0 - r_{\min})/(r_{\max} - r_{\min})$ and r_0 is the radial coordinate of the launching point on the disk surface. SV generally use $\gamma = 1$ which corresponds to a linear variation of the opening angle. Here the same value for γ is used unless specified otherwise. The limiting angles of the biconical wind structure are $\theta_{\min}$ and $\theta_{\max}$, which correspond to the cone angles at the inner and outer boundaries $r_{\min}$ and $r_{\max}$ of the wind.

With the chosen cylindrical coordinate system streamline velocities in the wind are given in the components v_r, v_θ and v_z. The velocity along a streamline is denoted by v_l. Then simple geometry gives the relations $v_r = v_l \sin\theta$ and $v_z = v_l \cos\theta$. SV make the assumption that v_l is given by a power law of the length $l = \left[(r - r_0)^2 + z^2\right]^{1/2}$ along the streamline

$$v_l = v_0 + (v_\infty - v_0)\left[\frac{(l/R_v)^\alpha}{(l/R_v)^\alpha + 1}\right]\,, \tag{4.15}$$

where the initial and asymptotic wind velocities along the streamline v_0 and v_∞ are taken as parameters of the model. The two further parameters in this velocity law are the acceleration scale height of the wind R_v and α the power law constant. In their model SV scaled the asymptotic velocity with local escape velocity at the streamline base, namely $v_{\mathrm{esc}} = (2\mathrm{GM}_{\mathrm{WD}}/r_0)^{1/2}$. As initial velocity they assumed $v_0 = 6\,\mathrm{km\,s^{-1}}$. The wind in the streamlines has not only a velocity in l-direction, but also an orbital velocity v_ϕ. It is initially given by the Keplerian motion of the disk at the streamline launching

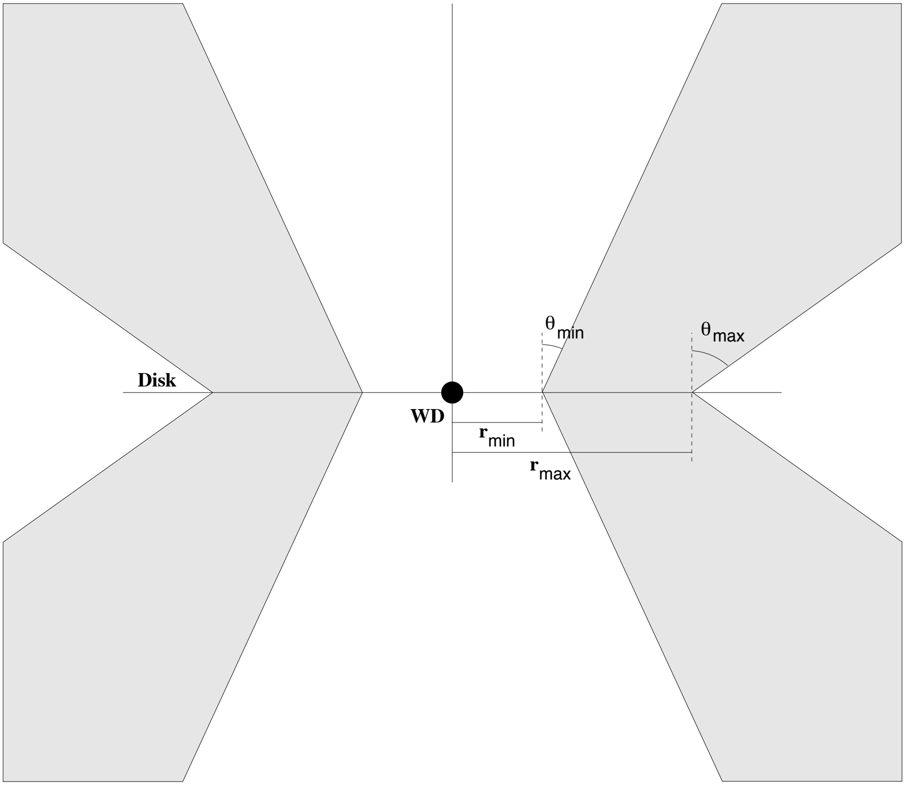

Figure 4.2: Biconical structure and important angles of the SV disk wind model

point $v_{\phi,0} = (\mathrm{GM}_{\mathrm{WD}}/r_0)^{1/2}$ and only changed by the assumption of angular momentum conservation around the rotation axis leading to

$$v_\phi r = v_{\phi,0} r_0 \, . \tag{4.16}$$

SV took the mass-loss rate per unit surface of the disk in the direction of a streamline, $\dot{m}$, at the base radius r_0 to be of the form

$$\dot{m}(r_0) = \dot{M}_{\mathrm{wind}} \frac{r_0^\lambda \cos\theta(r_0)}{\int \mathrm{d}A \, r_0'^\lambda \cos\theta(r_0')} \, , \tag{4.17}$$

with the area integral being over the disk surface between $r_{\min}$ and $r_{\max}$, more exactly

$$\int \mathrm{d}A = 2 \int_{r_{\min}}^{r_{\max}} \mathrm{d}r\, r \int_0^{2\pi} \mathrm{d}\phi\,, \tag{4.18}$$

with the factor of 2 being due to the disk having a lower and upper side . Despite the possibility with this formula to accomodate for a more complicated form of mass loss, SV generally used $\lambda = 0$ corresponding to a uniform mass loss. As the streamlines connect to the disk at an angle, the $\cos\theta$ factor is needed for correcting this.

One important thing to mention is that SV included a boundary layer as radiation source in their model which is not done in this work. SV used a non-equally spaced grid in r, z and θ above and below the disk. Densities are calculated for each grid cell at the cell center.

The density in the first cell above the disk is given by

$$\rho(r_0) = \frac{\dot{m}(r_0)}{v_z(r_0)}\,. \tag{4.19}$$

For points further out in the wind the values of r_0 and $\theta(r_0)$ need to be determined first. Simple geometrical considerations, namely the “projection” of the θ-run of the streamlines from a height z to the disk at $z = 0$, lead to

$$r_0 = r - z\tan\theta(r_0)\,, \tag{4.20}$$

with

$$\theta(r_0) = \theta_{\min} + (\theta_{\max} - \theta_{\min})\frac{r - r_{\min,z}}{r_{\max,z} - r_{\min,z}}\,, \tag{4.21}$$

where $r_{\min,z} = r_{\min} + z\tan\theta_{\min}$ and $r_{\max,z} = r_{\max} + z\tan\theta_{\max}$ are the r values which limit the wind cone at height z. Then, with given (r, z), r_0 and $\theta(r_0)$, the velocity $v(r,z) = (v_r(r,z), v_\theta(r,z), v_z(r,z))$ is readily calculated using equations 4.15 and 4.16. The density at (r, z) can then be calculated from the relation

$$\rho(r,z) = \frac{r_0}{r}\frac{\mathrm{d}r_0}{\mathrm{d}r}\frac{\dot{m}(r_0)}{v_z(r,z)}\,. \tag{4.22}$$

As the wind flows upwards from the disk the area between the streamlines increases. This is incorporated in the above equation via the $(r_0/r)(\mathrm{d}r_0/\mathrm{d}r)$ term, which is just the area between two streamlines at some height above the disk divided by the area between these two streamlines on the disk. Taken a geometrical view and keeping in mind that the distance l along a streamline is $l(r) = z/\cos\theta(r)$ one can derive

$$\frac{\mathrm{d}r}{\mathrm{d}r_0} = 1 + \frac{z}{\cos^2\theta(r)}\frac{\mathrm{d}\theta}{dr_0}\,. \tag{4.23}$$

Equipped with these densities and velocities the wind structure can easily be calculated.

Further assumptions of SV are a constant wind temperature of 20,000 K and local ionisation equilibrium. They also used only the ions H, He, C, N, and O considering only solar abundances for those. As a radiation transport model SV implemented a Sobolev method, which is described more closely in 4.1.6. The standard parameter set used for the SV model is shown in Table 4.1.

Table 4.1: Standard parameter set for SV model

Parameter	Value
$M_{\mathrm{WD}}(\mathrm{M}_\odot)$	0.8
$R_{\mathrm{WD}}(\mathrm{cm})$	7×10^8
$T_{\mathrm{WD}}(\mathrm{K})$	$40,000$
$\dot{M}_{\mathrm{disk}}(\mathrm{M}_\odot\mathrm{yr}^{-1})$	1×10^{-8}
$R_{\mathrm{disk}}(R_{\mathrm{WD}})$	34
$\dot{M}_{\mathrm{wind}}(\mathrm{M}_\odot\mathrm{yr}^{-1})$	1×10^{-9}
$\theta_{\mathrm{min}}(\mathrm{deg})$	20
$\theta_{\mathrm{max}}(\mathrm{deg})$	65
$r_{\mathrm{min}}(R_{\mathrm{WD}})$	4
$r_{\mathrm{max}}(R_{\mathrm{WD}})$	12
$R_v(R_{\mathrm{WD}})$	100
$v_\infty(v_{\mathrm{esc}})$	3
α	1.5
λ	0

4.2.2 Knigge, Woods & Drew Model

The model described in this subsection was first introduced by Knigge et al. (1995). Throughout this work we will refer to this model as KWD model. It is a second kinematical model for a biconical disk wind and was developed with reduction of the necessary parameters in mind. Hence fewer parameters as for the SV model are needed to describe a very similar accretion disk wind with the KWD model. The main physical parameters for the disk wind are outflow collimation, mass-loss rate as function of disk radius and the velocity gradient in the wind. As such they are the same as for the SV model, but described in different geometrical terms.

The basic wind geometry is such that the wind is emitted from the disk, but in a way that it seems to originate from a point D below the disk, as shown in Fig. 4.3. A blow-up depicting the geometric variables is shown in Fig. 4.4. Wind is emitted from the whole disk thus the degree of collimation is determined only by the distance d of the point D below the disk. From a geometrical point of view it is obvious that there exists a $d_{\min}$ for which the collimation is minimal. In the original KWD model $R_{\mathrm{disk}} = 50\, R_{\mathrm{WD}}$ which gives $d_{\min} = 3.57\, R_{\mathrm{WD}}$. The ratio $d/d_{\min}$ can be used as a measure for the geometric collimation of the wind. The range of opening angles $\Delta\gamma = \gamma_{\max} - \gamma_{\min}$ is maximised for $d = \sqrt{R_{\mathrm{disk}} R_{\mathrm{WD}}}$.

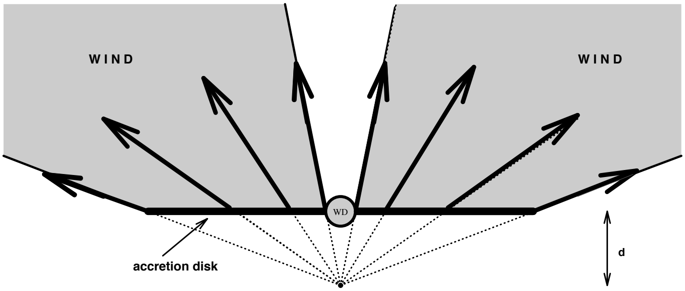

Figure 4.3: Biconical structure of the KWD disk wind model. Taken from Knigge et al. (1997).

The wind outflow follows streamlines like in SV. Those streamlines have a rotational velocity component which stems from the Keplerian rotational velocity $v_{\theta,0} = (\mathrm{GM_{WD}}/r_0)^{1/2}$ at the streamline footpoint with radius r_0. This

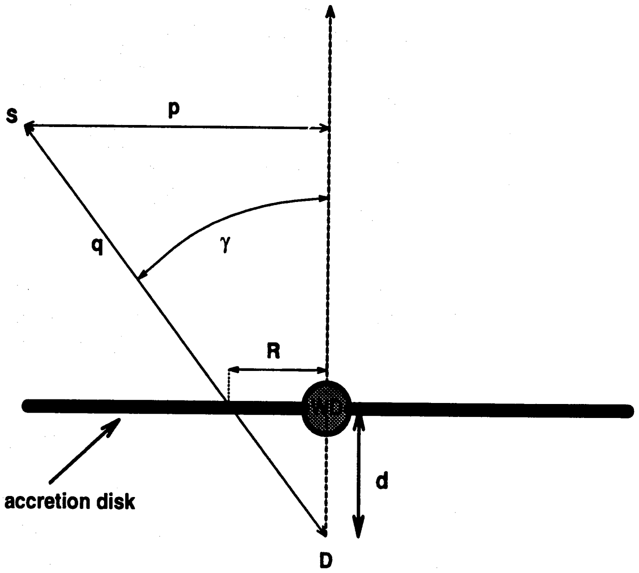

Figure 4.4: Geometric parameters used by KWD in their disk wind model. S is an arbitrary reference point. Taken from Knigge et al. (1995).

rotational velocity component is then changed by angular momentum conservation of wind material about the rotational axis. In our notation the rotational axis of the wind is the z-axis

$$v_\theta = \frac{r_0}{r}\sqrt{\frac{GM_{\mathrm{WD}}}{r_0}}\,. \tag{4.24}$$

In addition to the rotational components KWD implemented two velocity laws for the radial component. The first one is a constant velocity which is equal to the escape velocity at the streamline footpoint up to a factor f:

$$v_q(\vec{r}) = f v_{\mathrm{esc}}(r_0) = f\sqrt{\frac{2GM_{\mathrm{WD}}}{r_0}}\,. \tag{4.25}$$

For this work we only implemented the second radial velocity law of KWD, which is inspired by the theory of hot star winds. The analytic form KWD use as a basis for this is taken from the theory of hot star winds, see e.g. Castor & Lamers (1979); Lamers & Morton (1976) or Castor et al. (1975). It has the following form:

$$v(r) = v_0 + (v_\infty - v_0)\left(1 - \frac{R_*}{r}\right)^\beta . \qquad (4.26)$$

Introduced here are the quantities v_0, v_∞, R_* and β which can be seen as the initial velocity, the velocity at infinity and some kind of launching radius being the stellar radius in those cases. β adjusts the acceleration length. The CAK theoretical value is $\beta = 1/2$, but KWD decided to use the slightly higher value of $\beta = 4/5$. This value is mainly guided by their desire to distinct the accelerated hot disk wind model from the constant wind model. Furthermore $\beta > 1/2$ is suggested by some works, e.g. Lamers & Morton (1976). Recasting Eq. (4.26) for a disk wind KWD came up with the idea of using a v_∞ which scales with the escape velocity $v_{\mathrm{esc}}(r_0)$ at the streamline footpoint, which is a natural choice. This goes for the sound speed $c_{\mathrm{s}}(r_0)$ at the streamline footpoint as a choice for v_0, too. For the sound speed the approximate expression used is

$$c_{\mathrm{s}}(r_0) = 10\sqrt{\frac{T(r_0)}{10^4\mathrm{K}}}(\mathrm{km\,s^{-1}}) \qquad (4.27)$$

derived by Frank et al. (1985). For the “launching radius” there is not such a natural choice, rather KWD use a variable R_s instead which, in combination with β, sets an acceleration length scale for the wind. With all these considerations KWD derive a radial velocity law for the accelerated disk wind of the following form:

$$v_q(\vec{r}) = c_{\mathrm{s}}(r_0) + [f' v_{\mathrm{esc}} - c_{\mathrm{s}}(r_0)]\left(1 - \frac{R_s}{l + R_s}\right)^\beta , \qquad (4.28)$$

with $l = q - d\cos\gamma$ being the distance from the disk along the streamline. KWD use δ instead of γ to distinguish between the angle between the streamline and the disk normal, which is needed for l, but is only equal to γ as it is defined above the disk. As in this work the computational domain is only the half-sphere above the disk, δ and γ can be used unanimously. One obvious difference between R_* as it is used in Eq. 4.26 and R_s as it is used in Eq. (4.28) is the appearance of R_s in the denominator alongside l. This is a nice trick to ensure the non-singularity of v_q at $l = 0$. f' is just a constant scaling factor as is f in Eq. (4.25). Note also that as the velocity laws of SV are based upon hot star winds, as well, Eq. (4.15) is very similar to Eq. (4.28).

Now that we have established the velocity laws for the streamlines let us turn to the densities in the wind. The total mass-loss rate in the wind $\dot{M}_{\mathrm{wind}}$ is not equally distributed for each unit surface area on the disk, but instead the local mass-loss rate $\dot{m}$ is assumed to be linked to the local radiative flux on the disk and as such to the local disk temperature by a power law

$$\dot{m}(r_0) \propto F^{\alpha}(r_0) \propto T^{4\alpha}(r_0)\,. \tag{4.29}$$

Usually α is taken to be 1 so that the local mass-loss follows the temperature distribution on the disk and this value is consequently used throughout this work. The proportionality factor can be determined by the need of normalising to the total mass-loss rate in the wind $\dot{M}_{\rm wind}$. Starting from

$$\dot{M}_{\rm wind} = \int \mathrm{d}A\, K \dot{m}(r) = 2 \int_0^{2\pi} \int_{r_{\rm in}}^{r_{\rm out}} \mathrm{d}\phi\, r\, \mathrm{d}r\, K\, \dot{m}(r)\,, \tag{4.30}$$

with K being the proportionality factor to be determined and the surface integral being over the whole disk surface including the upper and lower sides one can derive

$$K = \frac{\dot{M}_{\rm wind}}{2\pi T_*^4 I}\,, \tag{4.31}$$

with $I = \int_{r_{\rm in}}^{r_{\rm out}} \mathrm{d}r \left(\frac{1}{r^2} - \frac{\sqrt{R_{\rm WD}}}{r^{5/2}} \right)$. For this derivation the standard accretion disk temperature distribution

$$T(r_0) = T_* r_0^{-3/4} \left(1 - \sqrt{\frac{R_{\rm WD}}{r_0}} \right)^{1/4}\,, \tag{4.32}$$

see Pringle (1981), with

$$T_* = \left(\frac{3 G M_{\rm WD} \dot{M}_{\rm disk}}{8\pi\sigma} \right)^{1/4}\,, \tag{4.33}$$

is used. Now that we have $\dot{m}(r_0)$, the streamlines angles and velocity laws we are able to calculate the initial density distribution right above the disk with

$$\rho_0(r_0) = \frac{\dot{m}(r_0)}{v_{(q,0)}(r_0)\cos\gamma}\,. \tag{4.34}$$

The density in the wind is then determined by mass continuity

$$\rho(\vec{r}) = \rho_0(r_0) \frac{r_0}{r} \frac{\mathrm{d}r_0}{\mathrm{d}r} \frac{v_{(q,0)}(r_0)}{v_q(\vec{r}}\,, \tag{4.35}$$

with the factor $\frac{r_0}{r}\frac{\mathrm{d}r_0}{\mathrm{d}r}$ being due to the geometrical increase in the unit area as the streamlines rise above the disk. Within the geometry of the KWD model this term is easily evaluated as

$$\frac{r_0}{r}\frac{\mathrm{d}r_0}{\mathrm{d}r} = \left(\frac{d}{q\cos\gamma}\right)^2 . \tag{4.36}$$

Inserting that into Eq. (4.35) yields the final equation for the density

$$\rho(\vec{r}) = \rho_0(r_0)\left(\frac{d}{q\cos\gamma}\right)^2 \frac{v_{(q,0)}(r_0)}{v_q(\vec{r})} , \tag{4.37}$$

where on the right-hand side there are only known quantities included and $\rho(\vec{r})$ can be calculated.

One major difference between KWD and SV is the use of an exact radiation transfer method versus the use of a Sobolev method. The standard parameter set for the KWD model is shown in Table 4.2.

Table 4.2: Standard parameter set for KWD model

Parameter	Value
$M_{\mathrm{WD}}(\mathrm{M}_\odot)$	0.8
$R_{\mathrm{WD}}(\mathrm{cm})$	6.8×10^8
$T_{\mathrm{WD}}(\mathrm{K})$	0
$\dot{M}_{\mathrm{disk}}(\mathrm{M}_\odot \mathrm{yr}^{-1})$	1×10^{-9}
$R_{\mathrm{disk}}(R_{\mathrm{WD}})$	50
$\dot{M}_{\mathrm{wind}}(\mathrm{M}_\odot \mathrm{yr}^{-1})$	1×10^{-11}
$d(R_{\mathrm{WD}})$	$14.3, 57.1$
d/d_{min}	$1, 16$
$R_v(R_{\mathrm{WD}})$	10
$v_\infty(v_{\mathrm{esc}})$	1.5
α	1
β	0.8

4.2.3 Hydrodynamical wind model

Contrary to the two kinematical models presented in the previous subsections the basis for the last wind model used in this work is a hydrodynamical analysis of accretion disk wind in CVs. Namely the work by Feldmeier & Shlosman which they presented in two consecutive papers (Feldmeier & Shlosman, 1999; Feldmeier et al., 1999). A thorough theoretical introduction to hydrodynamic analysis of an accretion disk wind was already given in Sec. 3.6, therefore we present here only the short summary of the "hydro wind model" actually used in this work.

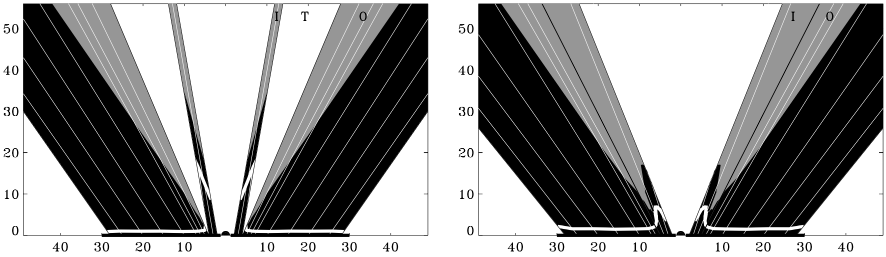

Figure 4.5: Wind geometry of a hydrodynamical wind above a SHS disk with $r_{\rm disk} = 30\,R_{\rm WD}$, $\alpha = 3/2$ (left-hand panel) and $\alpha = 1/2$ (right-hand panel) taken from FS. "I" and "O" mark the inner and outer wind with "T" being the transition region. For our hydro model developed here only the outer regions are of interest. Thin white lines indicate wind cones, thick white lines are locations of the flow critical points. Compare to Fig. 4.2.

The hydrodynamical analysis results in a picture of an accretion disk wind, which resembles quite well the kinematical picture of the SV model. Compare the outer wind in Fig. 4.5 to SV wind in Fig. 4.2. Furthermore the wind velocities derived in FS2 can be fitted with Eq. (4.15). With this in mind we refrain from developing a completely new model out of the hydrodynamical calculations, but instead use the results from the nozzle function analysis (Sec. 3.6.4) to constrain the parameters of the SV model. Only the mass-loss rate per disk annulus, which is taken to be a function of annulus area in the SV model (4.17) and therefore is a severe approximation, is changed to the power-law behaviour found by FS2. We use

$$\frac{{\rm d}\dot{m}(r_0)}{{\rm d}A(r_0)} = k r_0^{-1.9} \text{ for } r_0 > 5\,R_{\rm WD} \tag{4.38}$$

and

$$\frac{\mathrm{d}\dot{m}(r_0)}{\mathrm{d}A(r_0)} = \mathrm{const.} = \frac{\mathrm{d}\dot{m}(5\,R_{\mathrm{WD}})}{\mathrm{d}r_0} \text{ for } 3\,R_{\mathrm{WD}} < r_0 < 5\,R_{\mathrm{WD}}\,, \tag{4.39}$$

with $\mathrm{d}A(r_0) = \mathrm{d}\phi\, r\mathrm{d}r$ and where the constant k is determined via the requirement that the total mass-loss rate is given by $\dot{M}_{\mathrm{wind}} = \int \mathrm{d}A\,\dot{m}(r_0)$. As the mass-loss rates derived by the dynamical models are generally very low, actually too low to produce the observed P Cygni features, we leave the total mass-loss rate $\dot{M}_{\mathrm{wind}}$ as a parameter of the model. For the velocity law in the hydro wind we use Eq. (4.15) along the streamline and Eq. (4.16) for the rotational velocity. The terminal velocity of the wind streamlines is only very poorly constrained in the hydrodynamical models, we therefore take those values from the kinematical SV model. The standard parameter set and those values from the SV parameter set we fixed for the hydrodynamical wind model are shown in Table 4.3.

From the nozzle analysis we use $r_{\mathrm{min}} = 3\,R_{\mathrm{WD}}$ and $r_{\mathrm{max}} = 30\,R_{\mathrm{WD}}$ as a constraint of the area where the wind is launched. θ varies according to (4.14) with $\gamma = 1$, but we take $\theta_{\mathrm{min}} = 25°$ and $\theta_{\mathrm{max}} = 35°$ as fixed from the nozzle analysis. For the arc of reasoning which brought us to these values refer to Sec. 3.6.4.

4.2.4 Radiation sources

For all the above models the same radiation sources are used. We consider the white dwarf and the accretion disk as a source for photons. Neither a boundary layer, nor the secondary is considered. The latter because of the negligible amount of radiation it produces in the wavelength ranges important for the treatment of an accretion disk wind, whereas the former is neglected for several reasons. First the physics of a boundary layer is poorly understood, which makes it almost impossible to include it in a thorough fashion. It could even be, that a small magnetic field of the white dwarf disrupts the disk. This could create a corona like boundary layer, which would be too thin and too complicated to incorporate properly as a radiation source. On the other hand a boundary layer of 10,000 K as used by SV can be neglected without introducing a large error in wind description and resulting spectra.

The *white dwarf* is considered as a blackbody source with a temperature of T_{WD}. In principle it is possible to include spectra calculated with TMAP

Table 4.3: Standard parameter set for hydro wind model. Note that $r_{\rm min}$, $r_{\rm max}$, $\theta_{\rm min}$ and $\theta_{\rm max}$ are no longer parameters, but fixed by the nozzle analysis.

Parameter	Value
$M_{\rm WD}(\rm M_{\odot})$	0.8
$R_{\rm WD}(\rm cm)$	7×10^8
$T_{\rm WD}(\rm K)$	$40,000$
$\dot{M}_{\rm disk}(\rm M_{\odot} yr^{-1})$	1×10^{-8}
$R_{\rm disk}(R_{\rm WD})$	34
$\dot{M}_{\rm wind}(\rm M_{\odot} yr^{-1})$	1×10^{-9}
$\theta_{\rm min}(\rm deg)$	25
$\theta_{\rm max}(\rm deg)$	35
$r_{\rm min}(R_{\rm WD})$	3
$r_{\rm max}(R_{\rm WD})$	30
$R_v(R_{\rm WD})$	100
$v_\infty(v_{\rm esc})$	3
α	1.5
λ	0

instead of using a blackbody. Limb darkening in the Eddington approximation

$$\eta(\theta) = \frac{1}{2}(1 + \frac{3}{2}\cos\theta)\,, \tag{4.40}$$

with θ relative to the local outward normal, is also included. This provides a good approximation to limb darkening in the sun (e.g. Mihalas 1978) and was also used by KWD; SV and Long & Knigge (2002) in their CV wind codes.

The *accretion disk* as a radiation source is divided into a set of rings. For those rings either an accretion disk spectrum calculated with AcDc or a blackbody spectrum is used. The temperature for the blackbody is calculated according to (3.16). The rings are logarithmically spaced from $r_{\rm in}$ to $r_{\rm disk}$. As a standard set 20 rings are taken into account. In cases where AcDc rings are used as input there is the possibility to use further blackbody rings to fill up the disk. Although it is not quite clear whether the Eddington approximation also holds for an accretion disk, it is, at least for optically thick disks, a good first approximation (Diaz et al., 1996). We thus follow KWD; SV and Long & Knigge (2002) to include limb darkening for the disk also according to (4.40).

Input spectra, ring radii and temperatures are shown in the results chapter 5 for the calculated models.

4.3 Monte Carlo methods

Monte Carlo methods are a general class of computational methods based on statistical sampling and probabilities, thus the name resembling the famous casino. The first idea for this method dates back to the 1940ies (Metropolis & Ulam 1949, also see the review by Metropolis 1985). Nowadays such methods are widely used in quantum field theory, radiative transfer, simulation of hardware, only to name a few areas (see e.g. Langfeld 2007; Marchuk et al. 1980; Tenzer et al. 2006).

Monte Carlo methods can either be used to directly simulate the physical processes involved in the problem, or to numerically solve the equations involved describing the problem. Of course a direct simulation is also just a method of solving the equations. As the methods are based on statistical sampling the accuracy depends on the number of samples taken. In simple cases, unweighted Monte Carlo sampling, the error estimation can be approximated by using Poisson statistics. Therefore accurate Monte Carlo methods are computationally expensive. Fortunately computer time and memory is no longer such a limiting issue nowadays, furthermore are all the samples taken by a Monte Carlo algorithm independent, which makes it an ideal algorithm for parallel implementation. Together with the relative ease with which even complicated problems can be implemented in a Monte Carlo algorithm, as compared to standard solution methods of integro-differential equations, which often rely on special geometry or other methods for simplifying the problems, this has led to an increasing popularity of these methods.

In the following we will give some general definitions first and then introduce the Monte Carlo method for solving radiative transfer problems.

4.3.1 General definitions

Probability distribution functions are functions $p(x)$ normalised over an interval $x \in [a, b]$ such that $\int_a^b \mathrm{d}x\, p(x) = 1$. With such a distribution a random event that falls with probability $p(x)\mathrm{d}x$ into the interval $x, x+\mathrm{d}x$ can be simulated by drawing a random number ζ and requiring

$$\zeta = \int_a^x \mathrm{d}x'\, p(x')\,. \tag{4.41}$$

Throughout this work ζ is a pseudo-random number drawn from a uniform distribution between zero and one. As a random number generator we use an algorithm based on Wichmann & Hill (1982), which provides a fast way of calculating random numbers and has a sufficiently long sequence of independent random numbers.

In cases where there is no analytic solution for (4.41) and $p(x)$ can be tabulated such that $p_i = p(x_i)$ for $i = 1, N$ discrete values of x_i, the random event can be calculated via a *table-look up*. With the normalised cumulative probability

$$P_i = \frac{\sum_0^i p(x_j)\delta x_j}{\sum_0^N p(x_j)\delta x_j}\,, \tag{4.42}$$

we have to find an i, such that $P_i < \zeta < P_{i+1}$, then the random event is given by

$$x = x_i + \left(\frac{\zeta - P_i}{P_{i+1} - P_i}\right)(x_{i+1} - x_i)\ . \tag{4.43}$$

The *rejection method* is a third method of calculating a random event from a complicated probability distribution $p(x)$ if the peak of this distribution $p_{\max}$ is known. Sampling can then be done by using a distribution $g(x) > p_{\max}$ for which this can be done more easily. Sample x from $g(x)$ and accept this as a sample if $\zeta < f(x)/g(x)$, otherwise reject x and start again.

This is for example a good method for sampling a random unit vector (n_x, n_y) in the Euclidian plane. Generate a point (x, y) where x and y are independently sampled from $[-1, 1]$. Accept this point if $x^2+y^2 \leq 1$, reject it otherwise. Normalise the accepted vector appropriately.

Monte Carlo weights are a way of reducing computational costs and can also be used to equalise errors for the quantities of interest. They were introduced by Cashwell & Everett (1959) and developed further by Witt (1977). In a standard Monte Carlo calculation every sample has the same weight, namely $w = 1$. In some cases however, it might be favorable to adjust the weights. For example in the case we look at here, the sampling of emergent spectra, the weight represents a certain energy, so-called energy weight. In the case of equal weights more samples will be created for those parts of the spectrum where there is more energy available and less samples in the other parts. This leads to a difference in Monte Carlo noise, as the noise depends on the number of samples taken. To overcome this problem and to ensure the same level of Monte Carlo noise throughout the spectrum equal numbers of samples have to be taken throughout the spectrum. This in return leads to a necessary adjustment of the energy weight each sample carries. How we do this exactly is quantified in Sec. 4.3.3.

4.3.2 Radiative transfer in a Monte Carlo context

Solving the equation of radiative transfer (4.7) in multi-dimensional situations (e.g. non-spherically, or even asymmetric outflows, nebulae or other media), in maybe moving media, or where possibly special quantities like polarisation are to be considered, is widely done by application of Monte Carlo methods (see e.g. Ercolano et al. 2003; Kurosawa & Hillier 2001; Niccolini et al. 2003; Sim 2007a; Stern et al. 1995; Wolf et al. 1999). For this work we are interested in the transport of photons through the 3-D structure of an accretion disk wind. In the Monte Carlo context a photon is not a single particle, but rather a so-called *photon packet*, a collection of many photons with the same frequency ν and some total energy E_{pp}. Thus if we use the term photon in the following we actually mean such a photon packet. The idea of a direct Monte Carlo simulation is simple, photons are created and then transported through the medium by probabilistic means. All quantities of interest, the point of origin, the direction, the point of interaction, and the new direction are all determined via suiting probability distribution functions. After leaving the medium the photons are accumulated in angle and frequency bins, other quantities like polarisation can of course be saved, as well, but are not of interest for this work. One such photon trajectory is one Monte Carlo event and is independent of all other photon trajectories. Note that the photon's random walk in the medium satisfies the definition of a Markov chain.

Instead of using the escaping photons also the photon interactions can be used to determine a source function, which then can be integrated numerically without a further Monte Carlo algorithm. This method offers a high reduction of Monte Carlo noise and was put forward by Lucy (1999b), it is however, computationally not feasible for the large frequency grids we use in our calculations, because of a limit in available computer memory. But the knowledge of the photon trajectories and interactions can not only be used for the determination of a source function, but also for the determination of the radiation field in the medium. The radiation field in return can be used to update the temperature and occupation numbers in the medium. A first derivation of such an update procedure was given by Mazzali & Lucy (1993). With this techniques an iterative scheme can be implemented, which allows for a self-consistent solution of the radiative transfer in the medium. Without such a scheme appropriate temperatures and occupation numbers have to be assumed or pre-calculated.

4.3.3 Monte Carlo radiative transfer in this work

We use photon packets with energy weights in our implementation, where w_i represents the weight of the i-th photon. A weight of $w = 1$ corresponds to an energy

$$\Delta E = \frac{E_{\mathrm{total}}}{N_{\mathrm{pp}}}\,, \tag{4.44}$$

where N_{pp} corresponds to the total number of photons used in the simulation. We use the weights also as a method of keeping the Monte Carlo noise equal for each frequency bin, therefore the weights have to be adjusted as

$$w_\nu = \frac{E_\nu}{n_{\mathrm{pp}}}\frac{1}{\Delta E}\,, \tag{4.45}$$

where E_ν is the total energy in the frequency bin ν and n_{pp} the number of photons in that bin, the factor $1/\Delta E$ normalises the weight as to compare to the $w = 1$ case. As we then use exactly the same number of photons for each frequency bin, the initial frequency bin is not randomly sampled, only the initial photon frequency in this bin is sampled from a linear distribution.

Photons are either created on the white dwarf with a probability $p_{\mathrm{WD}} = E_{\mathrm{WD}}/E_{\mathrm{total}}$ or the disk surface with a probability $p_{\mathrm{disk}} = E_{\mathrm{disk}}/E_{\mathrm{total}}$. If a photon is created on the white dwarf the initial position on the white dwarf surface is completely random. The initial direction is determined with respect to the local outward normal and then transformed back to the standard coordinate system with the origin at the white dwarf center. In local polar coordinates the initial direction is given by $\hat{d}_{\mathrm{init}} = (1, \theta, \phi)$. The probability to emit in a solid angle $\mathrm{d}\omega = \sin\theta \mathrm{d}\theta \mathrm{d}\phi$ is given by

$$\mathrm{d}p(\theta, \phi) = \eta(\theta)\cos\theta\sin\theta\,\mathrm{d}\phi\,\mathrm{d}\theta\,, \tag{4.46}$$

where $\eta(\theta)$ is the standard limb darkening in Eddington approximation, see Eq. (4.40), and $\cos\theta$ is the geometric factor that the emitting surface appears smaller when seen under an angle θ. The $\sin\theta$ factor is purely due to the spherical coordinates and later comes again into play when the flux per solid angle $I_\nu/\mathrm{d}\omega$ is calculated from the photon bins. Obviously the ϕ-direction is arbitrary and as such sampled by $\phi = \zeta 2\pi$.

If a photon is created on the disk surface the initial position is given by $\vec{r}_{\mathrm{init}} = (r_{\mathrm{i}}, \phi_{\mathrm{i}}, z_{\mathrm{i}})$ in cylindrical coordinates. It is $z_{\mathrm{i}} = 0$ as the disk is taken to be infinitesimally thin, furthermore the disk is axisymmetric thus $\phi_{\mathrm{i}} = \zeta 2\pi$. The initial radial position r_{i} is found via a table-look up from the cumulative distribution function

$$P(r_{\mathrm{i}}) = \frac{\int_{r_{\mathrm{inner}}}^{r_{\mathrm{i}}} I_\nu \, 2\pi r \, \mathrm{d}r}{\int_{r_{\mathrm{inner}}}^{r_{\mathrm{disk}}} I_\nu \, 2\pi r \, \mathrm{d}r} , \tag{4.47}$$

where r_{disk} is the radius of the accretion disk and $I_\nu = I_\nu(\theta = 0)$ the intensity in the frequency bin at ν. The initial direction $\hat{d}$ is found in the same way as for emission on the white dwarf.

The next step is to determine whether and where a photon interacts. For this the optical depth along the line of flight (LOF) is calculated by integrating the opacities via a trapezium rule with transformations into the co-moving frame at each integration point. After this integration we not only know the total optical depth τ_{tot} for this LOF in the medium, but also the run of the optical depth $\tau = \tau(s)$ as a function of the distance s along the LOF. From the definition of the optical depth the probability that the photon escapes the medium is given by

$$p_{\mathrm{esc}} = e^{-\tau_{\mathrm{tot}}} , \tag{4.48}$$

then the probability that the photon scatters is given by

$$p_{\mathrm{scat}} = 1 - p_{\mathrm{esc}} . \tag{4.49}$$

If the sampled random number $\zeta < p_{\mathrm{esc}}$ then the photon escapes the medium, otherwise it scatters at an optical depth of

$$\tau_{\mathrm{scat}} = -\ln[1 - \zeta(1 - e^{-\tau_{\mathrm{tot}}})] . \tag{4.50}$$

After the calculation of τ_{scat} the point s along the LOF where this optical depth is reached and the scattering process happens is easily determined by inverting $\tau(s)$ and thus the location $\vec{r}_{\mathrm{scat}}$.

The escape of the photon can be implemented in two ways. The straightforward way is to really determine whether the photon leaves the wind or not, and if it leaves the wind, then it really leaves the simulation and “dies”, if it stays in the wind the whole photon weight stays in the wind. This is called a live or die algorithm (LOD). On the other hand the notion of weights allows at this point for an algorithm we term “forced scattering” (FSc). A part of the photon is taken to always scatter in the medium and a part of the photon, namely the one with the weight $w_{\rm esc} = wp_{\rm esc}$, escape and is detected. In this case ζ does not determine *if* scattering occurs, but only determines the point where scattering for the photon with the reduced weight $w_{\rm new} = wp_{\rm scat}$ occurs via Eq. (4.50). This technique is based on the assumption that a photon is really a photon packet consisting of many photons out of which a certain part would actually exhibit this behaviour and escape and another part would stay in the medium. Such an algorithm is used to reduce the noise of the simulation and has been used in a Monte Carlo simulation of accretion disk wind by Knigge et al. (1995).

After the scattering location is known, and also whether and in which line the scattering occurs which is of course not determined probabilistically, all there is left to be done is to assign the photon a new frequency $\nu_{\rm new}$ and a new direction $\hat{d}_{\rm new}$, both are taken to be independent from the incident $\nu_{\rm old}$ and $\hat{d}_{\rm old}$. The new direction is drawn from an spherically isotropic distribution and the new frequency is drawn from a Gaussian in the co-moving frame and then transformed into the rest frame. Therefore the new frequency is given by

$$\nu_{\rm new} = (\nu_0 + \xi \Delta\nu_{\rm D}) \left[1 + \frac{\vec{v}(\vec{r}_{\rm scat}) \cdot \hat{d}_{\rm new}}{c} \right] , \tag{4.51}$$

where ξ is a random number sampled from a Gaussian distribution with mean zero and standard deviation unity, ν_0 and $\Delta\nu_{\rm D}$ are the rest frequency and the Doppler width of the line in which scattering occurs respectively.

4.4 Code

In this section we are going to focus on the simulation code that was developed for the present work. A quick overview of the code itself and the workflow is followed by a comparison to other existing codes.

4.4.1 WOMPAT - the code flow overview

The code developed for this work was dubbed WOMPAT, an acronym for Wind mOdel with Monte carlo Parallel rAdiative Transfer. It is written in Fortran90 and parallelised with the aid of MPI. As a Monte Carlo code it is based on the simple principle of simulating photon transfer through the medium of concern by probabilistic means. In order to suppress Monte Carlo noise energy packets with energy weight w and frequency ν, which represent a family of monochromatic photons, are used. All parts of the photon's life, its creation, its interactions and finally where and how it leaves the wind are determined by probabilities. However, to keep the noise on equal level for each frequency bin, it is ensured that equal numbers of packets are created in each bin and the weights for the packets are adjusted accordingly. See also Sec. 4.3.3.

Preparation of the model:

The first step is to set up a frequency grid and model atoms for the calculations. This is done using the Tübingen Model Atom Database (TMAD), for a detailed account see Rauch & Deetjen (2003), Werner et al. (2003), and references therein. Our "standard" model atom consists of H, He, C, N, O, and Si. All the relevant UV wind lines are doublets, but no splitting is included in the atomic data. At this stage we also have to decide whether Doppler or Stark broadening is used. Our standard choice is Doppler broadening, therefore all models where not noted otherwise are calculated this way.

Having set up the atomic and frequency data the next step is to calculate densities and opacities due to the model used for this specific calculation. All our models are based on a cylindrical grid with logarithmic spacing in r- and z-direction, finer spaced cylinder rings (aka boxes) at the lower, inner edge of the disk wind, larger boxes towards the upper, outer edge. Densities, temperatures, and therefore the LTE opacities are constant in each box.

A third preparation step is to get the intensities of the emitting surfaces. This can either be done by calculating blackbody spectra with the appropriate temperature for the white dwarf or a disk ring, or by reading a pre-calculated spectrum (see also Sec. 4.2.4). With this information the total energy emitted and the look-up tables for choosing where photons are emitted are calculated via numerical integration.

Photon creation:

We use equal numbers of photons per frequency bin, therefore the initial photon frequency $\nu_{\rm init}$ is only probabilistically determined in the bin via

$$\nu_{\rm init} = \nu_j + \zeta(\nu_{j+1} - \nu_j)\,, \tag{4.52}$$

where ν_j and ν_{j+1} are the lower frequencies of the j-th and $j+1$-th frequency bin. The initial position $\vec{r}_{\rm init}$ and direction $\hat{d}_{\rm init}$ of the photon are determined via probabilistic means as described in Sec. 4.3.3.

Determination of the scattering location:

From $\vec{r}_{\rm init}$ along the direction $\hat{d}_{\rm init}$ the optical depth integration

$$\tau(s) = \int_0^s \kappa(l)\,\mathrm{d}l\,, \tag{4.53}$$

along the LOF is performed with the trapezium rule. The number of sampling points in each box depends on whether a resonance line is encountered or not. In resonance regions finer sampling is applied. Transformation into the co-moving frame is calculated at each sampling point independently. The run of $\tau(s)$ with the distance s along the LOF is stored alongside the information which line was encountered at which location. Whether scattering occurs, in the live or die case, and where it occurs, in the LOD and forced scattering cases, is determined via probabilistic means as described in Sec. 4.3.3, as is the new frequency $\nu_{\rm new}$ and new direction $\hat{d}_{\rm new}$ of the photon after the interaction.

Detection of emergent photons:

Photons, or in the FSc case rather parts of photons, can emerge from the computational domain in two ways. They can either hit the surface of the white dwarf or the disk, then they are absorbed there and removed from the simulation, or they can leave the domain on the sides or upper edge, where they are detected in a “virtual detector”. Our detector bins the photons in frequency and angle bins by adding the emergent weight $w_{\rm esc}$ of the photon to the appropriate bin. After all photons have been propagated the bins contain information $E_{\rm bin}$ in units of energy per second, which can be converted to an intensity I_ν per frequency and solid angle as

$$I_\nu = E_{\rm bin}\frac{1}{\Delta\nu}\frac{1}{\Delta\omega} = E_{\rm bin}\frac{1}{\Delta\nu}\frac{1}{2\pi\sin\theta\,\Delta\theta}\,, \tag{4.54}$$

where $\Delta\nu$ is the frequency bin width. $\Delta\omega = 2\pi\sin\theta\,\Delta\theta$ is the solid angle which is taken up by the angle bin for which the intensity should be calculated.

In a LOD run a new photon is created after the previous photon left the wind. In a FSc run the remaining part of the photon is propagated again until it reaches a certain minimum weight after which the photon is treated in a LOD manner. This procedure is repeated for all N photons used for the simulation. Note that as we use equal numbers of photons for each frequency bin it is obvious that N is a multiple of the number of frequency bins.

4.4.2 Monte Carlo radiation field estimators and temperatures

The knowledge of the individual photon paths can also be used for creating Monte Carlo estimators of the radiation field. These can then be used to calculate new temperatures and new occupation numbers in an iterative process (Mazzali & Lucy, 1993; Lucy, 1999a). The radiation temperature T_R can be calculated with the mean photon energy in a blackbody radiation field $\bar{x} = h\bar{\nu}/kT_R$, which is given by $\bar{x} = 3.832$. With the frequency moment

$$\bar{\nu} = \frac{\int_0^\infty \nu J_\nu \,\mathrm{d}\nu}{\int_0^\infty J_\nu \,\mathrm{d}\nu}\,, \tag{4.55}$$

the radiation temperature is calculated as

$$T_R = \frac{h\bar{\nu}}{\bar{x}}\,. \tag{4.56}$$

Monte Carlo estimators for the mean intensity J_ν can be obtained from the results that the energy density of the radiation field in the frequency interval $[\nu, \nu + \mathrm{d}\nu]$ is given by $u_\nu = 4\pi/c\, J_\nu \,\mathrm{d}\nu$ as shown in Eq. (4.5). A photon packet with energy $\epsilon_p = w_p \Delta E$ contributes with this energy to the time-averaged energy content of the volume it passes as $\epsilon_p \delta t/\Delta t$, where $\delta t = l/c$ with l being the length the photon travels through the box and Δt is the duration of the Monte Carlo experiment taken as $\Delta t = 1$ in our stationary case. From this argument we can construct an estimator for the monochromatic mean intensity

$$J_\nu \mathrm{d}\nu = \frac{1}{4\pi}\frac{1}{\Delta t}\frac{1}{V}\sum_{\mathrm{d}\nu} \epsilon_p l\,, \tag{4.57}$$

where V is the volume of the box under consideration and the summation is over all tracks of photons in the frequency range $[\nu, \nu + \mathrm{d}\nu]$. Correspondingly we can construct an estimator for the integrated mean intensity

$$J = \frac{1}{4\pi}\frac{1}{\Delta t}\frac{1}{V}\sum \epsilon_p l\,, \tag{4.58}$$

where the sum is now performed over all photon tracks in the box regardless of frequency. With these estimators obtained after one Monte Carlo run with a LOD algorithm it is straightforward to compute new temperatures for the boxes using (4.56).

With these new temperatures new occupation numbers and opacities can be calculated, then another set of photons is propagated through the wind. This procedure is repeated roughly 5 times until the temperature differences between two iteration steps are only of the order of a few percent, at most. There is however no strict convergence criterium, but experience shows that after a few iterations there is no more general trend, but the temperatures rather fluctuate around some mean value. If that is the case we use the temperature structure obtained by this method as a basis for propagating one single set of photons through the wind to obtain final spectra. This can then be done for a smaller spectral range in order to keep the noise of the final spectra as low as possible, whereas for the temperature structure calculations the whole spectral range has to be considered.

A flowchart for WOMPAT as an overview of the complete algorithm is shown in Fig. 4.6.

4.4.3 Comparison with existing codes

In this section we present two tests for WOMPAT. The first one is very simple and is a comparison with AcDc to check if the disk emission in WOMPAT works properly. Secondly we compare our results for the standard SV and KWD models with the results obtained by the other state-of-the-art Monte Carlo accretion disk code *Python* by Long & Knigge (2002).

Ring emission compared to AcDc

As a first step we compare a disk made of 20 blackbody rings with the spectra obtained by AcDc_RingRot with the same 20 blackbody rings as input. This is shown in Fig. 4.7. The area integration of the rings is the same for both codes, but the limb darkening is different. AcDc uses only a geometrical correction of emission, whereas WOMPAT utilises a full limb darkening according to (4.40). As expected there is no major difference between the two codes besides the Monte Carlo noise in the spectra obtained with WOMPAT.

For the second test we compare AcDc ring spectra with the emission from the disk by WOMPAT if we use the AcDc spectra as input in our code. Fig. 4.8 shows no significant differences, except for the Monte Carlo noise, between the spectra. From these tests we conclude that emitting photons from the disk with our Monte Carlo code works as it is intended.

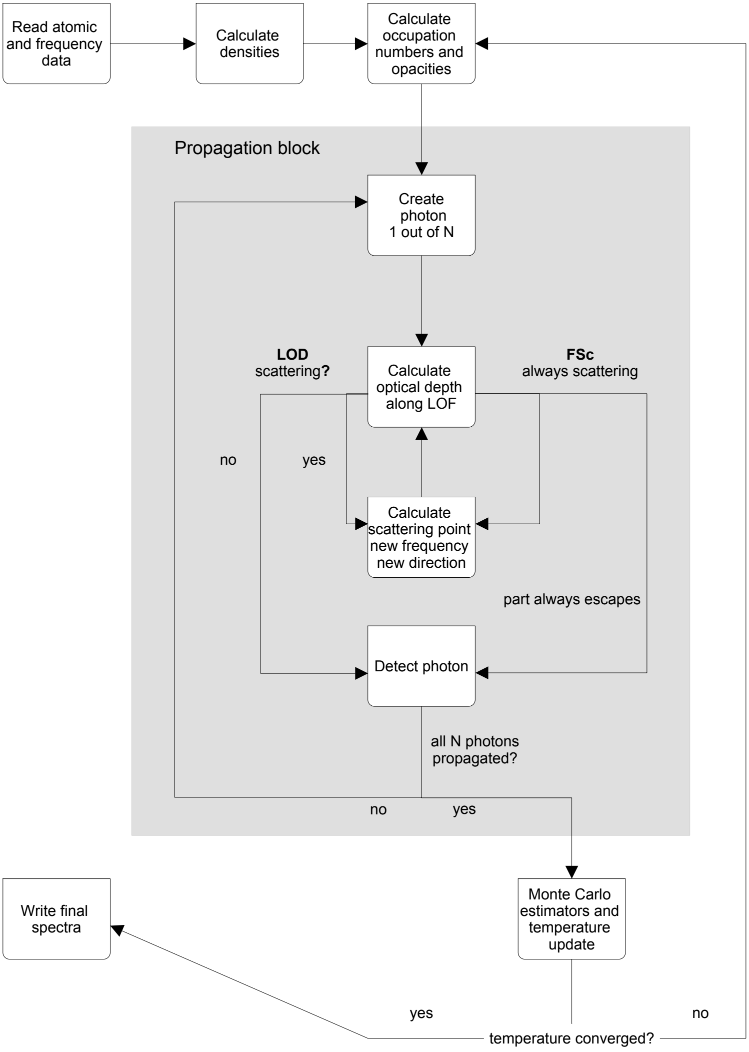
Read atomic and frequency data
Calculate densities
Calculate occupation numbers and opacities
Propagation block
Create photon 1 out of N
LOD scattering?
FSc always scattering
Calculate optical depth along LOF
no
yes
Calculate scattering point new frequency new direction
part always escapes
Detect photon
all N photons propagated?
no
yes
Write final spectra
Monte Carlo estimators and temperature update
yes
no
temperature converged?

Figure 4.6: Code flowchart of WOMPAT. The main loop is the "propagation block" marked by the grey backdrop with which N photons used for the calculation are propagated. Note also the differences between LOD and FSc algorithms.

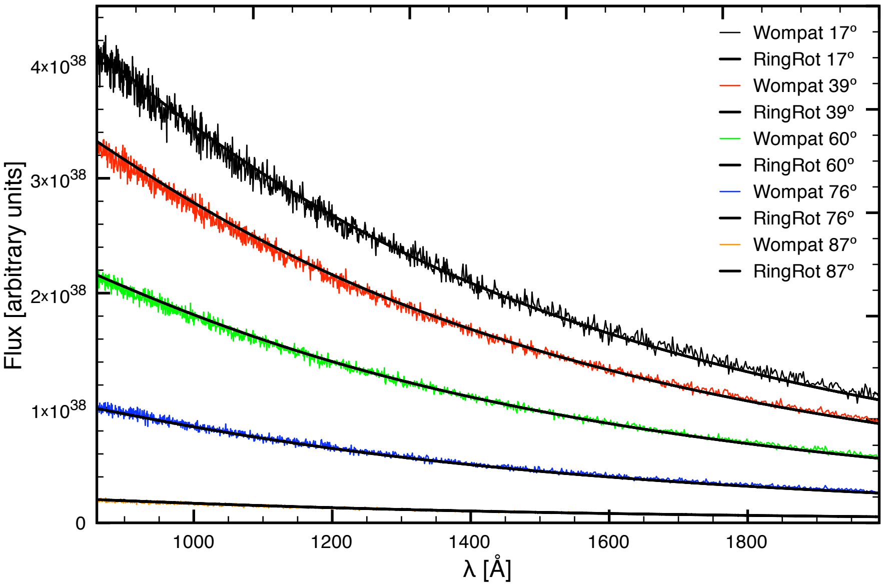

Figure 4.7: Comparison between blackbody spectra as calculated with AcDc_RingRot and calculated with WOMPAT.

WOMPAT vs Python

Here we compare our results for the standard SV and KWD models (see Sec. 4.2.1, 4.2.2 and Tab. 4.1, 4.2) with results obtained with Python. All Python results were kindly provided by Sim (2007b). There are three major differences between the two codes, (i) Python uses a Sobolev method to calculate optical depth, (ii) Python utilises an approximate NLTE method following Mazzali & Lucy (1993), but also a pseudo-LTE switch can be used, (iii) Python solves the temperature structure self-consistently. More to the last point as we compare the temperature structures obtained with WOMPAT and Python. Note that in order to keep the differences between the codes as small as possible we use Doppler broadened lines only for these comparisons.

Figure 4.9 shows the line profile of the C IV 1550 Å resonance line for different inclination angles as calculated with WOMPAT (coloured lines) and with Python (black lines) for the SV model. The results for the two codes are

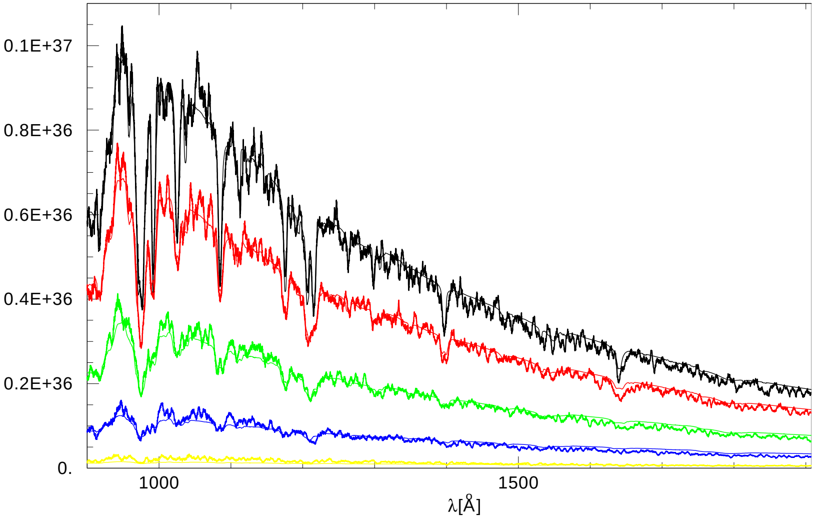

Figure 4.8: Comparison between a real disk spectrum calculated with AcDc and the spectrum of emitted disk photons with WOMPAT. Shown are inclinations $17, 39, 60, 76 \,\&\, 80$ degrees from top to bottom with the thick coloured "noisy" lines being the Monte Carlo spectra and the thin lines the AcDc spectra.

not in complete agreement, but keeping in mind the differences between the implementations the results are promising. The WOMPAT spectra were calculated using an isothermal wind with 20,000 K, whereas the Python spectra are based on a temperature structure, this might account for the differences. The spikes at the rest-wavelengths are only present for 20,000 K SV models, but are independent of the frequency grid used. They are definitely unphysical "artifacts" as they are present for all inclination angles and too strong and sharp for being a real line, but we were unable as to determine where exactly they originate from.

Figure 4.10 shows exactly the same comparison only for the KWD model. The differences for this wind model are larger than the differences for the SV model. These are probably due to the larger differences between LTE and NLTE in the thin KWD wind, which leaves a question of validity for this comparison. As the occupation numbers are resembled in the depth of the lines, we can clearly say that those are not similar in WOMPAT and in Python, which we attribute to the differences in temperatures and occupation number calculations. On the other hand we can conclude that the velocity structure is implemented in a correct way, as the width of the lines is comparable and this is only dependent on the velocities.

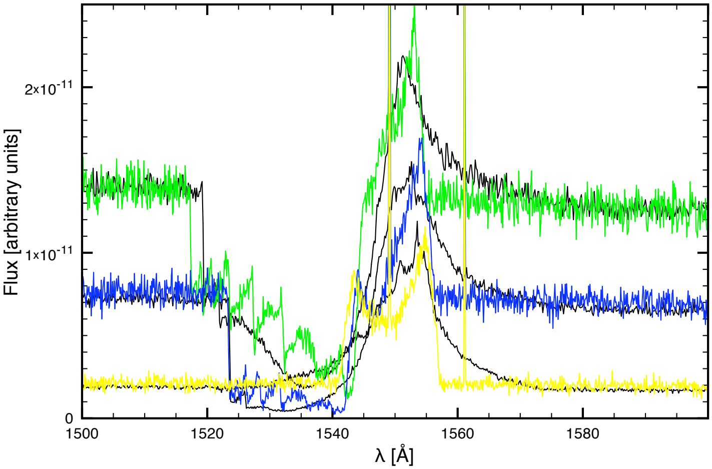

Figure 4.9: Comparison of calculated C IV 1550 Å resonance lines for the SV model and different inclination angles. Plotted are results from Python (black lines) and WOMPAT (coloured lines). Inclination angles are from top to bottom: 45.0° (green), 62.5° (blue) and 80.0° (yellow). Spectra are unsmoothed and the spikes are probably artifacts (see text).

We can not only compare spectral lines, but also calculated temperature structures for the SV standard model. These are shown in a 3-D plot as temperature over r-z in Fig. 4.11. Next to small deviations due to Monte Carlo noise there is no significant difference between the temperatures obtained with Python and the temperatures obtained with WOMPAT for the inner parts of the wind. However, the rise of the temperature is significantly faster when calculated with WOMPAT, as well as the plateau of the temperature in the lower outer parts of the wind being higher than for calculations with Python. These differences are attributed to the differences of the two codes in calculating occupation numbers, approximate NLTE compared to LTE, and the differences in the radiative transfer. If we compare the WOMPAT results with a Python run which calculates the occupation numbers in a pseudo-LTE way, the differences diminish, but are still visible. In order to save computer time

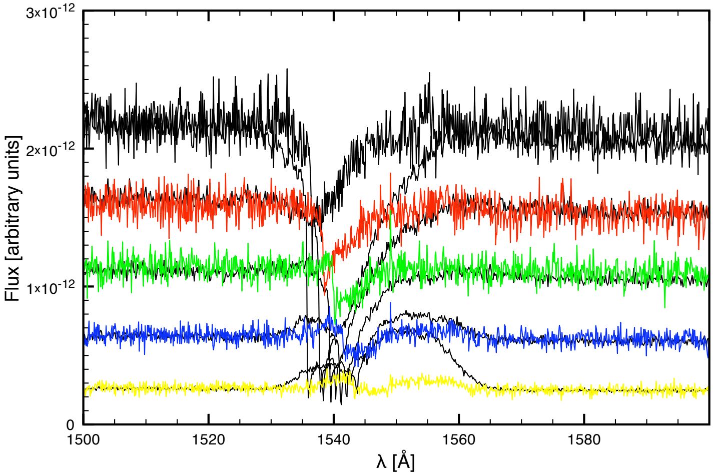

Figure 4.10: Comparison of calculated C IV 1550 Å resonance lines for the KWD model and different inclination angles. Plotted are results from Python (black lines) and WOMPAT (coloured lines). Inclination angles are from top to bottom: $40.0°$ (black), $50.0°$ (red), $60.0°$ (green), $70.0°$ (blue) and $80.0°$ (yellow).

we also implemented an ad hoc temperature structure, where the wind is assumed to have a temperature of 20,000 K for boxes with $z < 20R_{\mathrm{WD}}$ and r from the outer $2/3$ of the wind, and a temperature of 40,000 K for the other parts. This structure aims on resembling the NLTE temperature structure calculated with Python without going through iterative processes and is shown in Fig. 4.12. Results obtained with this temperature structure are shown and compared to wind with constant temperatures and wind with iteratively calculated temperatures in the results sections 5.1.2 and 5.1.3.

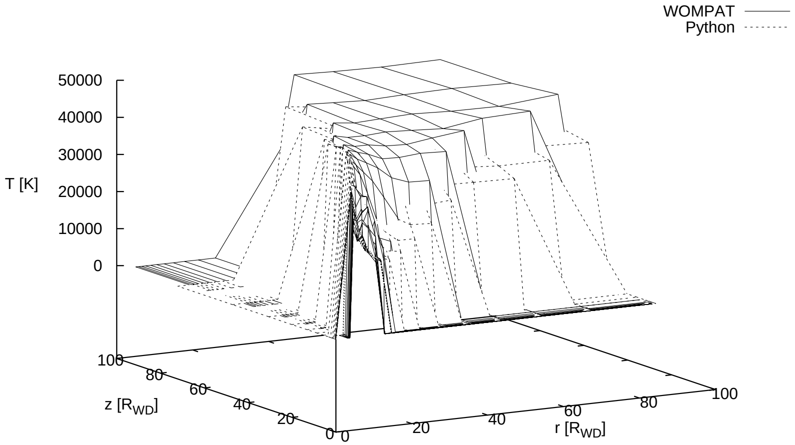

Figure 4.11: Comparison of temperature structures for the standard SV model calculated with WOMPAT (solid lines) and Python (broken lines). Plotted are the temperatures of the boxes in K over the r-z coordinates of the box center in white dwarf radii.

Techniques – summary

Wind code WOMPAT

- 3-D Monte Carlo radiative transfer
- LTE occupation numbers
- parallel calculations
- opacities calculated in co-moving frame

Wind models

- Shlosman & Vitello
- Knigge, Woods & Drew
- hydrodynamical model
- disk and white dwarf as radiation source

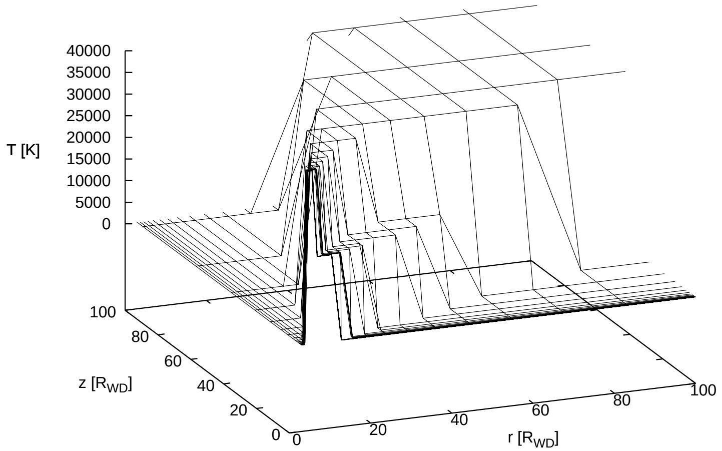

Figure 4.12: The ad hoc temperature structure for a standard SV model. Two areas of constant temperature, 20,000 K for the lower outer regions of the wind, 40,000 K for the other parts. Plotted are the temperatures of the boxes in K over the r-z coordinates of the box center in white dwarf radii.

CHAPTER 5

Results

> *"Enthusiasm is followed by disappointment and even depression, and then by renewed enthusiasm."*
>
> [Murray Gell-Mann]

5.1 The standard models

The standard SV and KWD models were only implemented as a reference and in order to compare to existing codes. Nevertheless they are also a good for comparison with our new hydrodynamical wind model (see Sec. 4.2.3) and for demonstrating a very interesting finding, the dependence of the P Cygni profile strength of the UV resonance lines on the line broadening function used. Abundances as shown in Tab. 5.1 are used for all models, except where noted otherwise. Also the doublets are not split up in our models.

5.1.1 Comparison of densities

Densities ρ in units of $\mathrm{g/cm^3}$ for the three models used in this work are shown in Figs. 5.1 (SV), 5.2 (hydro) and 5.3 (KWD). A comparison between these figures yields the obvious differences in the models. The overall mass-loss rate for KWD is smaller than the mass-loss rate for the SV and hydro models, therefore the overall density in this model is lower. For all models the density drops very fast from the highest values close to the disk to values several orders of magnitude lower in the outer regions of the wind. The most important difference between the models stems from the different radial dependence of the mass-loss rate in the models. In SV there is no radial dependence of

Table 5.1: Element abundances used for the standard models.

Element	Number fraction
H	0.897829
He	0.100000
C	0.000484
N	0.000122
O	0.000839
Si	0.000727

the mass-loss rate, except for the streamline angle run with radius, therefore the density just above the disk is almost the same for every r. Of course this is not the intuitive behaviour of a line-driven disk wind and the radial run of the mass-loss rate and thus of the densities in the KWD and hydro models is much more realistic. In both these models it is shown that the density in the inner parts of the wind is higher and then gradually drops for higher r.

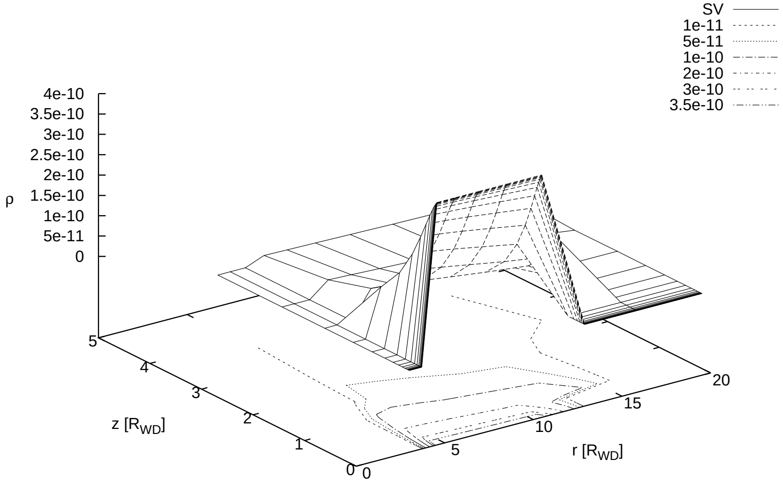

Figure 5.1: Wind density in the standard SV model. Plotted are densities ρ in $\mathrm{g/cm^3}$ and isocontours.

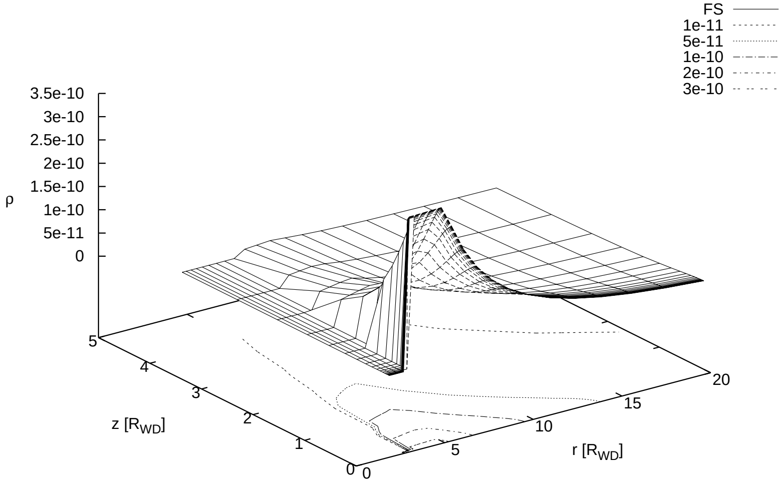

Figure 5.2: Wind density in the standard hydrodynamical model. Plotted are densities ρ in $\mathrm{g/cm^3}$ and isocontours.

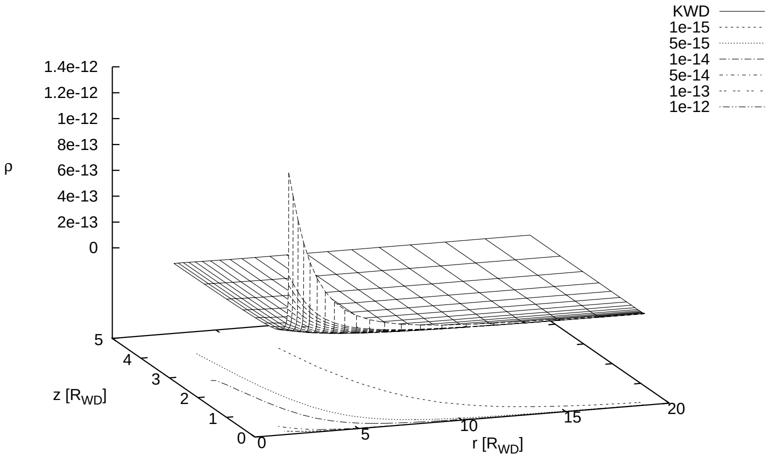

Figure 5.3: Wind density in the standard KWD model. Plotted are densities ρ in $\mathrm{g/cm^3}$ and isocontours.

5.1.2 Standard SV model

The standard SV model as described in Sec. 4.2.1 was used to test the influence of the temperatures in the wind, as well as the influence of the size of the computational domain on the calculated spectra. We used two sizes for the computational domain, a “small” cylinder with radius and height $100\,R_{\rm WD}$ and a “large” cylinder with radius and height $2000\,R_{\rm WD}$. Our standard grid size is 30 x 30 boxes and the standard wavelength range for all the calculations here is between 850 Å and 2000 Å, including the important N V and C IV wind lines, but also the hydrogen Lyman edge at 912 Å. We show calculations for the large grid first. Resulting spectra for a constant wind temperature of 20,000 K are shown in Fig. 5.4. For this temperature the C IV line at 1550 Å is very prominent. Depending on the inclination it shows either a absorption, emission or P Cygni profile. Also a prominent feature is the Si IV line at 1400 Å, which shows the same profiles as the carbon line. The Lyman edge is also clearly seen as it gets stronger for larger viewing angles. Completely missing is the N V line at 1240 Å, because of the low temperatures in the wind. The strong spikes in the line centers of C IV and Si IV at low inclination angles are probably “artifacts” in very view frequency grid points directly at the line center, see also Fig. 4.9 and the explanation there.

The picture changes dramatically if we consider a constant wind temperature of 40,000 K as shown in Fig. 5.5. Most of the lines, which are present for a temperature of 20,000 K in the wind are gone, only very weak C IV 1550 Å and Si IV 1400 Å lines persist, but instead the N V 1240 Å line is strong and features P Cygni profiles for intermediate inclination angles.

When we use the 20,000/40,000 K temperature structure as described in Sec. 4.4.3 for the wind the resulting spectra (Fig. 5.6) resemble both, the spectra calculated with constant wind temperatures of 20,000 and 40,000 K, although the “lower temperature” lines such as the C IV are much weaker than for the constant temperature. However, the “higher temperature” lines, mainly the N V, are as strong as for the constant temperature. This is due to the larger volume of the wind being at 40,000 K as compared to the area with 20,000 K.

The last possibility for wind temperatures we have in this work is to calculated them iteratively. For the SV model the resulting temperatures are shown in Fig. 4.11. Clearly the temperature structure calculated in such an iterative process is a high temperature, roughly 40,000 K, almost throughout the entire wind, thus we expect the spectra to be similar to those for a constant 40,000 K

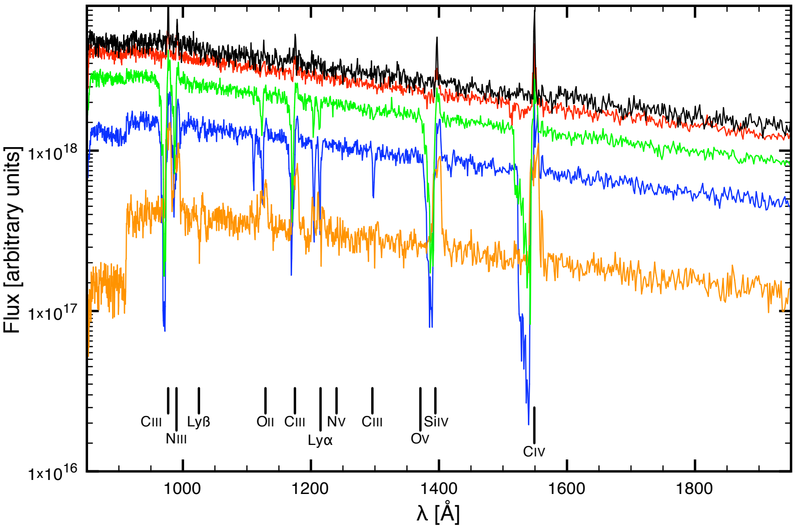

Figure 5.4: Standard SV model spectra for $T_{\rm wind} = 20,000\,{\rm K}$ on a large grid. Inclination angles are from top to bottom: 10.0° (black), 27.5° (red), 45.0° (green), 62.5° (blue) and 80.0° (orange). Note the prominent C IV 1550 Å and Si IV 1400 Å lines, as well as the Lyman edge. The N V 1240 Å line is absent.

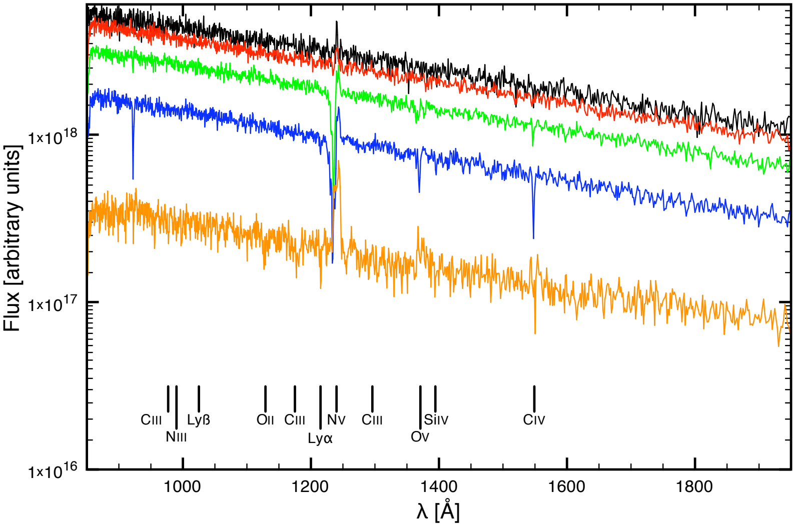

Figure 5.5: Standard SV model spectra for $T_{\rm wind} = 40,000\,{\rm K}$ on a large grid. Inclination angles as above. Note the prominent N V 1240 Å line. The C IV 1550 Å and Si IV 1400 Å lines are very weak, the Lyman edge is absent.

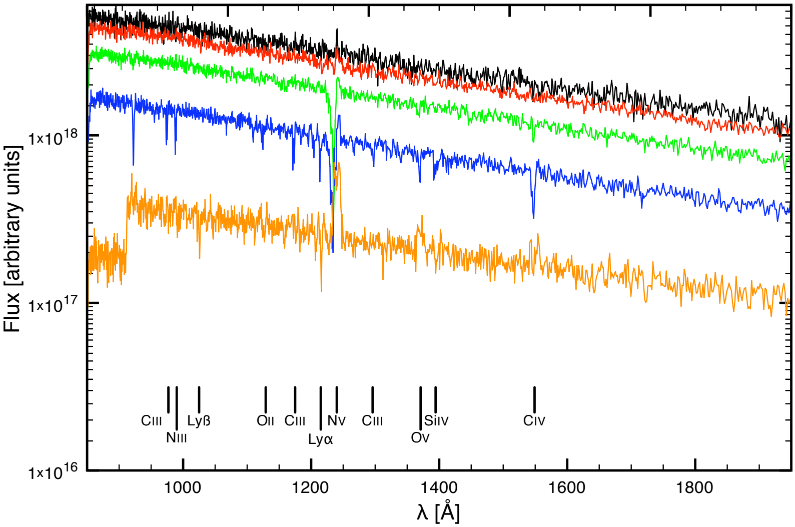

Figure 5.6: Standard SV model spectra for the 20,000/40,000 K temperature structure on a large grid. Inclination angles as above. Spectral features are a mixture of the features in Fig. 5.4 and Fig. 5.5.

wind temperature. Indeed the spectra in Fig. 5.7 resemble quite closely those in Fig. 5.5.

A further important comparison is that for the different sizes of our computational domain. In Fig. 5.8 we show a comparison of the C IV 1550 Å and Si IV 1400 Å lines for models with 20,000 K wind temperature to exemplify the differences. The important difference is the width of the absorption troughs, which are systematically broader for the larger computational domain. From this we can conclude that there is absorbing material in the lines even beyond the small domain and it is therefore important for calculations of real systems to use the larger domain. If only a small computational domain is used faster moving parts of the wind might be missed and the lines might not appear as broad as they are in the observation. The larger number of boxes seems to resolve the lines slightly better than the 30 x 30 grid, but the difference is not as distinct as to justify the significantly higher demands in memory and computer time for such model grids.

We can also use either Doppler or Stark line broadening mechanisms, which makes a big difference on the resulting line strengths of the model. Fig. 5.9 shows a comparison of the N V 1240 Å line calculated with Doppler

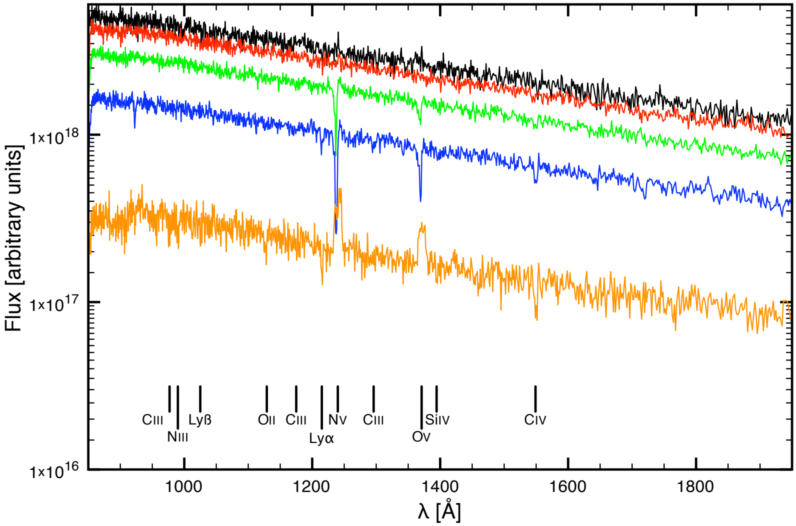

Figure 5.7: Standard SV model spectra for iterated temperature on a large grid. Inclination angles as above. Note the similarity to Fig. 5.5.

and Stark broadening and different mass-loss rates for an inclination of $45.0°$. For the standard mass-loss rate of $\dot{M}_{\rm wind} = 1 \cdot 10^{-9} {\rm M}_\odot/{\rm yr}$ the line with Doppler broadening shows a P Cygni profile with a deep absorption trough, whereas for Stark broadening with the same mass-loss rate the line is still present with a P Cygni profil but very weak. For Stark broadening and even lower mass loss the line disappears completely. The profile gets slightly stronger for higher mass-loss rates, but the factor of 5 leads to very high mass-loss rates without even reproducing the complete profile. Estimations for reproducing the strong P Cygni profile we obtain for Doppler broadening lead to mass-loss rates in the range of the accretion rate, the whole disk needs to be evaporated before reaching the white dwarf – an unrealistic scenario. One probably solution to this problem might be the introduction of clumps in the wind. These could then be denser as compared to a standard smooth wind and this might lead to realistic P Cygni profiles for realistic mass-loss rates even with Stark broadening. However, we did not explore such a clumping for our wind models and the above conclusion remains speculation.

The reason for this different behaviour lies in the different form the line opacity has if calculated with the different broadening functions. A Doppler profile is slightly higher in the core, but not as broad as a Stark profile if plotted as opacity over wavelength. A Stark profile has slightly less opacity in the line

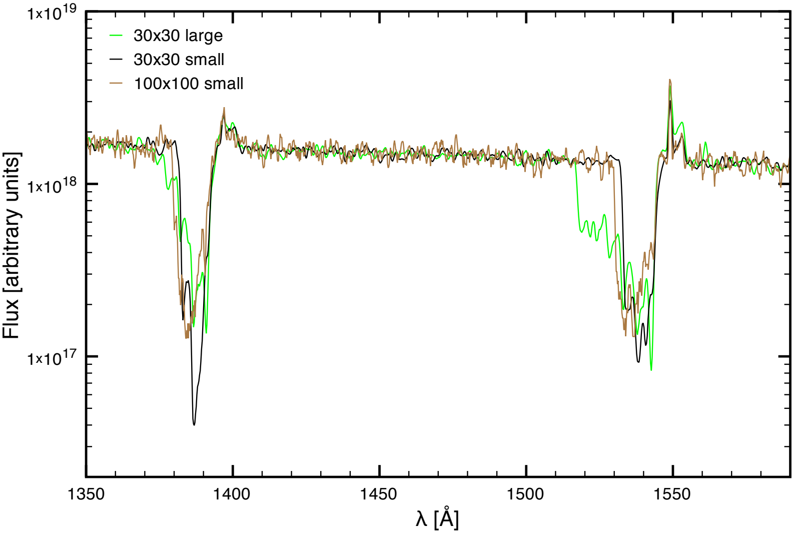

Figure 5.8: Comparison of the C IV 1550 Å and Si IV 1400 Å lines for models with 20,000 K wind temperature and different computational domain sizes and different numbers of boxes. Exemplarily shown is an inclination of 45°. Note the lines for the larger domain being systematically broader.

core, but is broader in the wings. In the relevant UV range, however, the continuum opacity is this high that only the line cores make it above the continuum. Therefore only the line core height above the continuum is relevant for the line opacity, and as this is higher for Doppler broadening the lines are more pronounced if the opacities are calculated in this way.

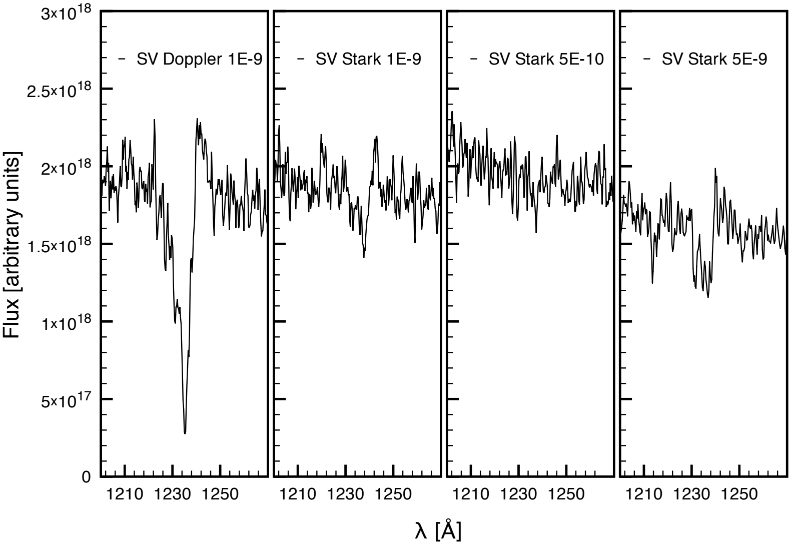

Figure 5.9: Comparison of the N V 1240 Å line calculated with Doppler and Stark broadening and different mass-loss rates for an inclination of $45.0°$. The left-hand panel shows a Doppler broadened model with $\dot{M}_{\rm wind} = 1 \cdot 10^{-9} \rm M_{\odot}/yr$. The other three panels show Stark broadened lines with $\dot{M}_{\rm wind} = 1 \cdot 10^{-9} \rm M_{\odot}/yr$, $5 \cdot 10^{-10} \rm M_{\odot}/yr$ and $5 \cdot 10^{-9} \rm M_{\odot}/yr$.

5.1.3 *Standard hydrodynamical model*

For the hydrodynamical model almost the same results and conclusions as for the SV model apply, although there are some minor differences between the models. As a comparison of this new hydrodynamical wind model with the old SV model the same calculations as in the above subsection are presented here. Fig. 5.10 shows spectra for a 30 x 30 grid on a large computational domain with a constant wind temperature of 20,000 K. The same lines as for the SV model feature prominently, but the C IV 1550 Å and Si IV 1400 Å lines have a much narrower absorption trough and furthermore show a prominent double peaked structure for high inclination.

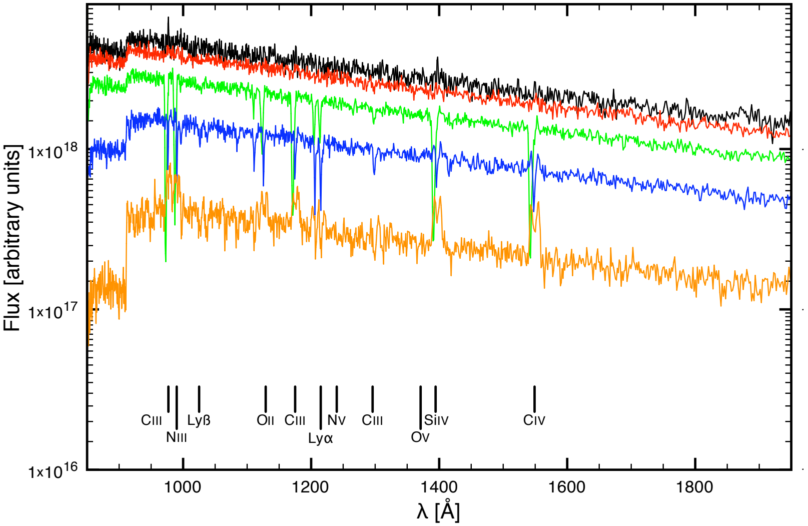

Figure 5.10: Standard hydrodynamical model spectra for $T_{\rm wind} = 20,000\,{\rm K}$ on a large grid. Inclination angles are from top to bottom: 10.0° (black), 27.5° (red), 45.0° (green), 62.5° (blue) and 80.0° (orange). Note the prominent C IV 1550 Å and Si IV 1400 Å lines, as well as the Lyman edge. The N V 1240 Å line is absent.

For a wind with a constant temperature of 40,000 K as it is shown in Fig. 5.11 the same differences compared to the SV are obvious, the N V 1240 Å line is narrower. All the differences, including the prominent double peaked structure and the narrower absorption trough, are best explained with the higher collimation of the wind for the hydrodynamical model.

In the case of the hydrodynamical model the spectra calculated with a

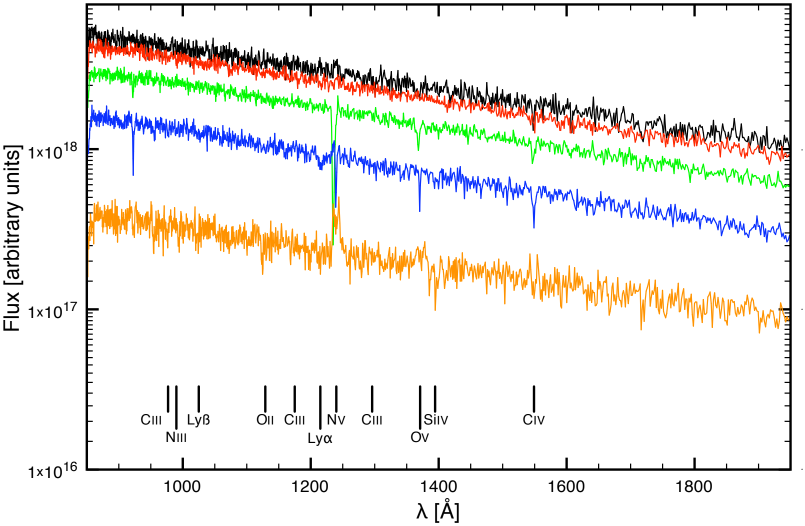

Figure 5.11: Standard hydrodynamical model spectra for $T_{\rm wind} = 40,000\,{\rm K}$ on a large grid. Inclination angles as above. Note the prominent N V 1240 Å line. The C IV 1550 Å and Si IV 1400 Å lines are very weak, the Lyman edge is absent.

20,000/40,000 K temperature structure, shown in Fig 5.12, do not have as much features of the 20,000 K wind as it is the case for the SV model. This is due to the wind in the hydro model being much thinner, in the area where it has 20,000 K for the temperature structure, compared to the SV model. E. g. the Lyman edge is missing completely.

However, an iterated temperature structure (Fig. 5.13) yields, for the case of the hydrodynamical wind model, not a huge difference to the 20,000/40,000 K temperature structure as for the SV model.

A direct comparison for a N V 1240 Å line seen at an inclination of 45.0° between the hydrodynamical model and the SV model is shown in Fig. 5.14 in the first panel. The SV line is slightly broader and has a more pronounced emission peak. The other two panels in this figure show the same line and inclination but for different computational domain sizes and box numbers. Differences between the calculations for the large domain with either 100 x 100 boxes or 30 x 30 boxes is negligible. We therefore use only 30 x 30 boxes for our further calculations to overcome memory limitations. For the small domain the line is, as the lines in Fig. 5.8, clearly narrower than the lines for the large domain. Therefore further calculations use the large domain.

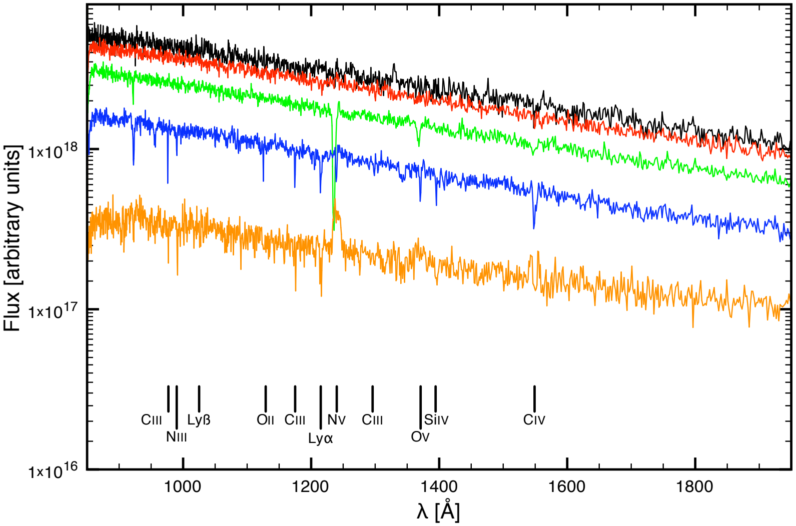

Figure 5.12: Standard hydrodynamical model spectra for the 20,000/40,000 K temperature structure on a large grid. Inclination angles as above. Spectral features are a mixture of the features in Fig. 5.10 and Fig. 5.11 with a strong emphasis on the features for a 40,000 K wind.

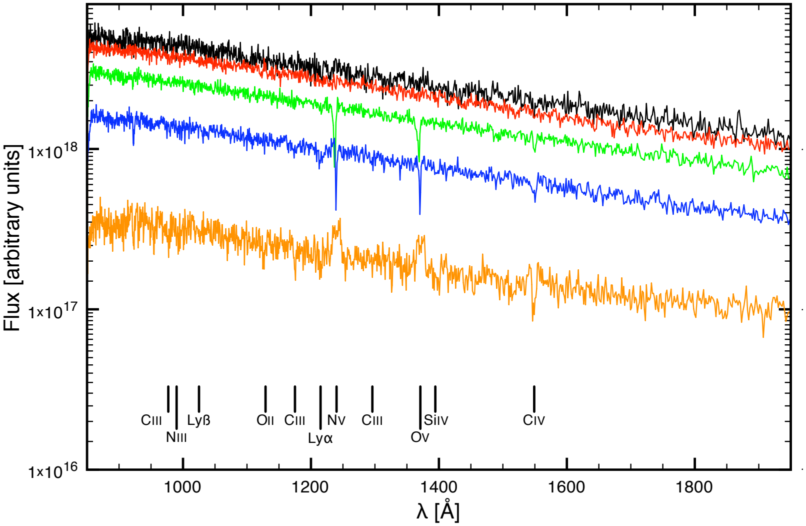

Figure 5.13: Standard hydrodynamical model spectra for the temperature structure iterated on a large grid. Inclination angles as above. Only minor differences to Fig.5.12.

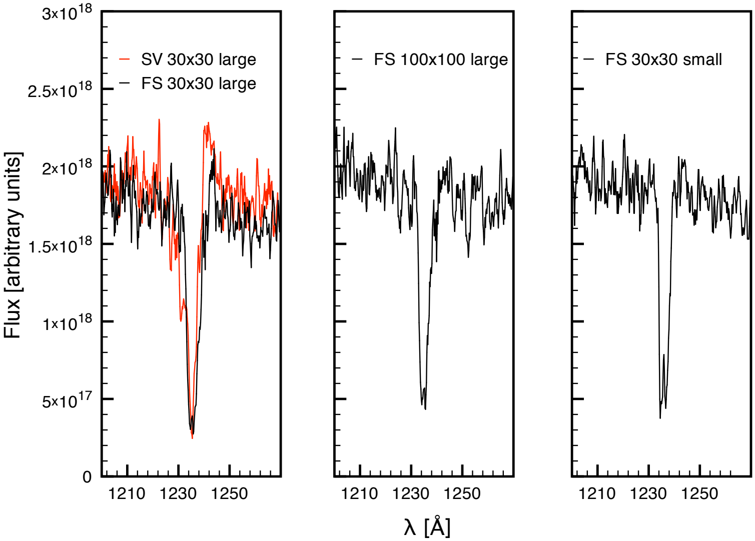

Figure 5.14: Comparison of the N V 1240 Å line for models with 20,000/40,000 K temperature structure. Computational domain size and number of boxes used in the panels. Ploted is an inclination of $45.0°$. Black are the lines for hydrodynamical models, red is a reference SV model line. Note the line is broader for SV as compared to the hydro model.

Different broadening mechanisms for different mass-loss rates are presented in Fig. 5.15. As an example we use again the N V line seen at an inclination of $45.0°$. The panel on the left-hand side shows the Doppler broadened line with the standard mass-loss rate of $\dot{M}_{\mathrm{wind}} = 1 \cdot 10^{-9} \mathrm{M}_{\odot}/\mathrm{yr}$, the other three panels show Stark broadened lines for different mass-loss rates. Clearly we need to adjust the mass-loss rate to higher values in order to obtain a deeper line. Even with mass-loss rates of $\dot{M}_{\mathrm{wind}} = 5 \cdot 10^{-9} \mathrm{M}_{\odot}/\mathrm{yr}$ the line is not as strong as with the standard mass-loss rate for Doppler broadening.

5.1.4 Standard KWD model

The standard KWD model was merely implemented as comparison to existing codes. In Fig. 4.10 we showed such a comparison. Other test calculations with this model showed similar results and led to the same conclusions as the two other models above. As these were thoroughly discussed in the last two subsections we refrain from repetition and move directly to comparisons with observations in the next section.

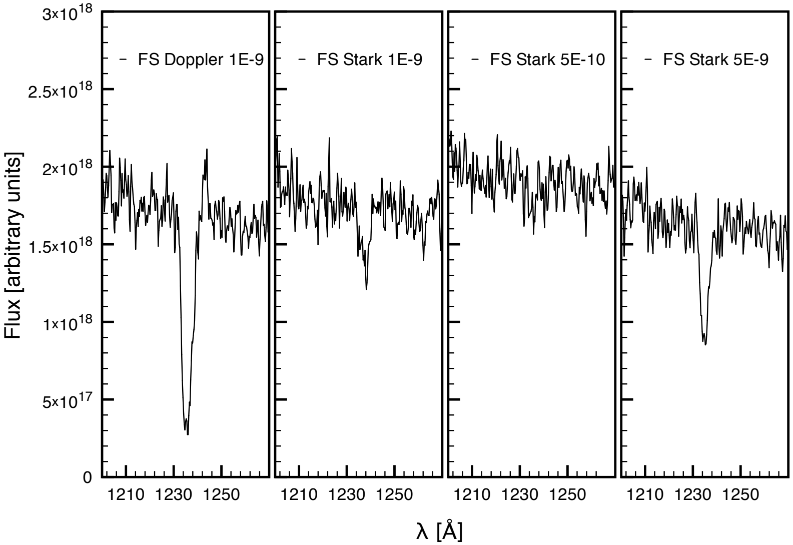

Figure 5.15: Comparison of the N V 1240 Å line calculated with Doppler and Stark broadening and different mass-loss rates for an inclination of 45.0°. Mass-loss rates in units of $\mathrm{M}_{\odot}/\mathrm{yr}$ and broadening mechanism used in the panels.

5.2 AM Canum Venaticorum

AM CVn the prototype system for the class of AM CVns (Sec. 2.6) is a hydrogen-deficient “nova-like” CV with a magnitude in V-band of $14.1\,\mathrm{mag}$ (Downes et al., 1997) in the constellation Canes Venatici (hunting dogs). The orbital period is found to be $1029\,\mathrm{s}$ (Harvey et al., 1998). For primary and secondary masses there are several values in discussion with the most agreed upon being $M_{\mathrm{WD}} \approx 0.7\,\mathrm{M}_{\odot}$ and $M_2 \approx 0.1\,\mathrm{M}_{\odot}$ (Roelofs et al., 2007). However, using synthetic accretion-disk spectra calculated with AcDc we find the best agreement with observation for models with $M_{\mathrm{WD}} = 0.6\,\mathrm{M}_{\odot}$ and accretion rate $\dot{M} = 1 \cdot 10^{-8}\mathrm{M}_{\odot}/\mathrm{yr}$ (Nagel, priv. comm.). Therefore these parameters are adopted for the study of AM CVn wind spectra in this work. The corresponding white dwarf radius is $R_{\mathrm{WD}} = 9550\,\mathrm{km}$. As accretion-disk extension we consider $r_{\mathrm{in}} = 1.36\,R_{\mathrm{WD}}$ to $r_{\mathrm{out}} = 14.66\,R_{\mathrm{WD}}$, where the outer radius r_{out} of the disk corresponds roughly to the tidal radius. The best agreement with observation for disk models is found if an inclination of roughly $40°$ is assumed (Nagel et al., 2004). There are, however, also other inclination angles up to $60°$ discussed in the literature. We use a SV model for the wind calculations with the parameter set given in Table 5.2 and abundances as given in Table 5.3.

A first WOMPAT model with a constant wind temperature of 40,000 K, shown in Fig. 5.16, can be used for a rough estimation of the mass-loss rate. The wind spectra show the observed P Cygni profile in the N V 1240 Å line, which is not present in the disk spectrum. Neither the model for an inclination of $39°$, nor the model for an inclination of $60°$ gives a completely satisfying fit for a mass-loss rate of $1 \cdot 10^{-9}\mathrm{M}_{\odot}/\mathrm{yr}$. In both cases the N V 1240 Å is not broad enough and the emission part of the profile is not high enough to resemble the observation. Overall the observation is resembled more closely by the model with an inclination of $60°$, although this finding might change if other mass-loss rates are considered. Also note that the sharp Ly α line at 1215 Å, which is neither fit by the disk nor by the wind is due to interstellar hydrogen. The calculated models are reddened by $E(B-V) = 0.1$ for $i = 39°$, $E(B-V) = 0.13$ for $i = 60°$ and $E(B-V) = 0.04$ for the AcDc model, with the large differences between the AcDc model and the wind model being due to the presence of a white dwarf with an effective temperature of 100,000 K in the wind models, which is not included in the disk model.

A closer comparison of only the N V 1240 Å line with the observed STIS spectrum was performed for the same 30 x 30 grids on the large computa-

Table 5.2: WOMPAT parameter set for AM CVn with SV model.

Parameter	Value
$M_{\rm WD}({\rm M}_\odot)$	0.6
$R_{\rm WD}({\rm cm})$	9.55×10^8
$T_{\rm WD}({\rm K})$	$40,000$ or $100,000$
$\dot{M}_{\rm disk}({\rm M}_\odot {\rm yr}^{-1})$	1×10^{-8}
$r_{\rm in}(R_{\rm WD})$	1.36
$r_{\rm out}(R_{\rm WD})$	14.66
$\dot{M}_{\rm wind}({\rm M}_\odot {\rm yr}^{-1})$	1×10^{-9}, 5×10^{-9}, 5×10^{-10}
$\theta_{\rm min}({\rm deg})$	20
$\theta_{\rm max}({\rm deg})$	65
$r_{\rm min}(R_{\rm WD})$	1.4
$r_{\rm max}(R_{\rm WD})$	10
$R_v(R_{\rm WD})$	100
$v_\infty(v_{\rm esc})$	3
α	1.5
λ	0

Table 5.3: Abundances for the model atom used for AM CVn calculations. Almost no hydrogen and solar metal abundances.

Element	Mass fraction
H	$9.878 \cdot 10^{-11}$
He	$9.878 \cdot 10^{-1}$
C	$2.864 \cdot 10^{-3}$
N	$8.390 \cdot 10^{-4}$
O	$7.789 \cdot 10^{-3}$
Si	$7.176 \cdot 10^{-4}$

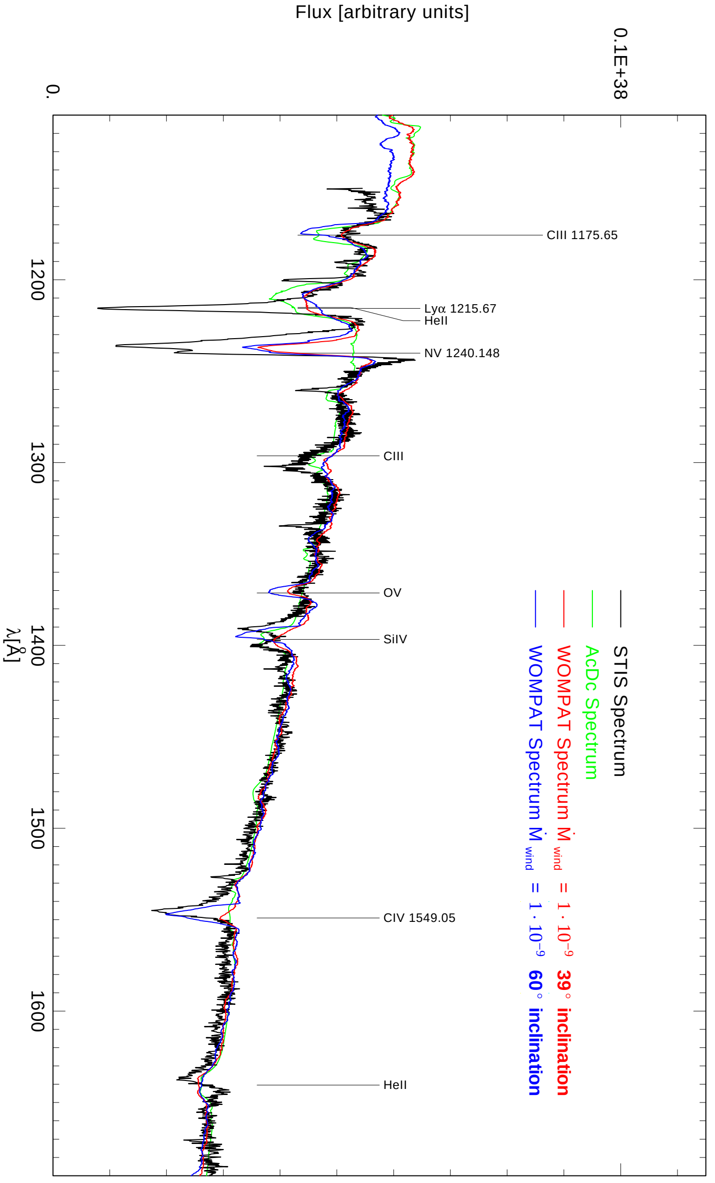

Figure 5.16: Observed STIS spectrum (black), AcDc disk spectrum (green) and wind spectra for inclinations of $i = 39^\circ$ (red) and $i = 60^\circ$ (blue), both for $\dot{M} = 1 \cdot 10^{-9} \mathrm{M}_\odot/\mathrm{yr}$. Note the prominent P Cygni profile of the 1240 N V line not resembled by the disk, but by the wind. All models are reddened (see text).

tional domain and for the same three mass-loss rates as the comparison for the whole STIS spectral range. Results for an inclination of 39° are plotted in Fig. 5.17, those for an inclination of 60° in Fig. 5.18. We chose these two inclinations as the first is the most probable value as discussed in the literature and the latter is the most extreme inclination which is still thought of being possible. For both inclination angles mass-loss rates of $1 \cdot 10^{-9} \mathrm{M}_\odot/\mathrm{yr}$ and $5 \cdot 10^{-10} \mathrm{M}_\odot/\mathrm{yr}$ show generally lines which are not strong enough as compared to the observed spectrum. The best fits are found for the mass-loss rate of $5 \cdot 10^{-9} \mathrm{M}_\odot/\mathrm{yr}$, which are a factor of 5 higher than the canonical mass-loss rate of 10% of the accretion rate. Interestingly for the lower two mass-loss rates the calculations for an inclination angle of 60° fit the observations slightly better than the lines for an angle of 39°. For the highest mass-loss rate, however, the inclination angle of 39° seems more likely. Therefore our calculations do not allow for a better determination of the system's inclination, yet.

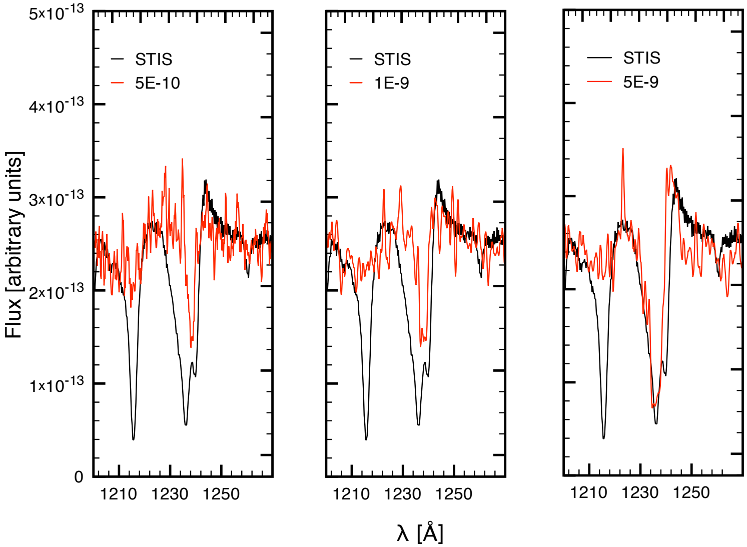

Figure 5.17: Comparison of calculated N v 1240 Å lines with the observed line. The STIS observation is plotted in black in each panel, the calculated lines are shown for an inclination of 39° and are drawn in red. Mass-loss rates in units of $\mathrm{M}_\odot/\mathrm{yr}$ from left to right: $5 \cdot 10^{-10}$, $1 \cdot 10^{-9}$, and $5 \cdot 10^{-9}$. Also compare to Fig. 5.18.

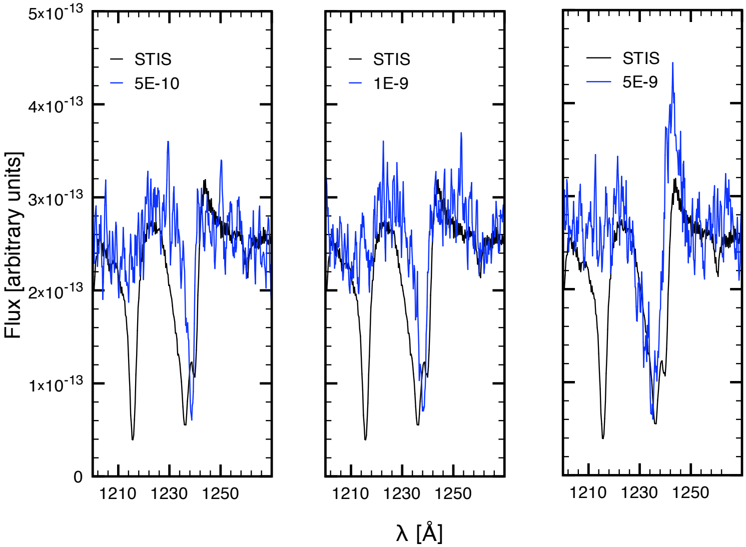

Figure 5.18: Comparison of calculated N V 1240 Å lines with the observed line. The STIS observation is plotted in black in each panel, the calculated lines are shown for an inclination of 60° and are drawn in blue. Mass-loss rates in units of $\mathrm{M}_\odot/\mathrm{yr}$ from left to right: $5 \cdot 10^{-10}$, $1 \cdot 10^{-9}$, and $5 \cdot 10^{-9}$. Also compare to Fig. 5.17.

5.3 SS Cygni

SS Cygni in the prominent constellation cygnus (swan) is the brighest known dwarf nova with an outburst brightness of $8.2\,\mathrm{mag}$ in V band and $12.1\,\mathrm{mag}$ in quiescence (Downes et al., 1997). It belongs to the U Gem subtype of DN and has the basic system parameters primary mass $M_{\mathrm{WD}} = (1.19 \pm 0.02)\mathrm{M}_{\odot}$, secondary mass $M_2 = (0.704 \pm 0.002)\mathrm{M}_{\odot}$, and an inclination $i = (37 \pm 5)^{\circ}$ (Ritter & Kolb, 1998). Further parameters needed for a SV wind model calculation for SS Cyg, as well as, AcDc rings for irradiation of the wind from a real disk, are taken from Kromer et al. (2007). Table 5.4 shows all the relevant parameters for an accretion disk wind model of SS Cyg as they were used in our calculations.

Table 5.4: WOMPAT parameter set for SS Cyg with SV model.

Parameter	Value
$M_{\mathrm{WD}}(\mathrm{M}_{\odot})$	1.19
$R_{\mathrm{WD}}(\mathrm{cm})$	3.9×10^{8}
$T_{\mathrm{WD}}(\mathrm{K})$	$50,000$
$\dot{M}_{\mathrm{disk}}(\mathrm{M}_{\odot}\mathrm{yr}^{-1})$	1.56×10^{-8}
$r_{\mathrm{in}}(R_{\mathrm{WD}})$	2.56
$r_{\mathrm{out}}(R_{\mathrm{WD}})$	102.56
$\dot{M}_{\mathrm{wind}}(\mathrm{M}_{\odot}\mathrm{yr}^{-1})$	4.44×10^{-10}
$\theta_{\mathrm{min}}(\mathrm{deg})$	20
$\theta_{\mathrm{max}}(\mathrm{deg})$	65
$r_{\mathrm{min}}(R_{\mathrm{WD}})$	2.56
$r_{\mathrm{max}}(R_{\mathrm{WD}})$	20
$R_v(R_{\mathrm{WD}})$	100
$v_{\infty}(v_{\mathrm{esc}})$	3
α	1.5
λ	0

Only the calculation for a large 30 x 30 grid with our usual 20,000/40,000 K temperature structure and a mass-loss rate of $\dot{M} = 4.44 \cdot 10^{-10}\mathrm{M}_{\odot}/\mathrm{yr}$ is pre-

Table 5.5: Abundances for the model atom used for SS Cyg & Z Cam calculations. These correspond to solar values.

Element	Mass fraction
H	$7.382 \cdot 10^{-1}$
He	$2.495 \cdot 10^{-1}$
C	$2.913 \cdot 10^{-3}$
N	$8.541 \cdot 10^{-4}$
O	$7.823 \cdot 10^{-3}$
Si	$7.300 \cdot 10^{-4}$

sented here. Fig. 5.19 shows the limiting inclination angles $i = 32°$ (blue) and $i = 42°$ (red) in comparison to an observed HST spectrum. The very prominent Ly α line originates in the disk and is contaminated in the observation by interstellar absorption. In contrast to this, the N V 1240 Å line originates from the wind, but is comparably weaker in the observation and in the models. Also present in the models, but without a prominent P Cygni profile, is the C IV 1550 Å line.

For a comparison with observation we concentrate on the wavelength range around Ly α for which outburst spectra obtained with HST exist. One such spectrum, Z3DV0104T as taken from MAST, is shown in Fig. 5.20 together with the relevant part of the calculated spectrum for inclinations of $32°$ and $42°$ as used above. Ly α is well resembled, except for the interstellar absorption which deepens the line, but also the N V line is well resembled by the model. The model with an inclination of $32°$ seems to fit slightly better than the model for $42°$. Different mass-loss rates, different temperature structures, or different abundances might change this. The exploration of these possibilities, however, is beyond the scope of this work.

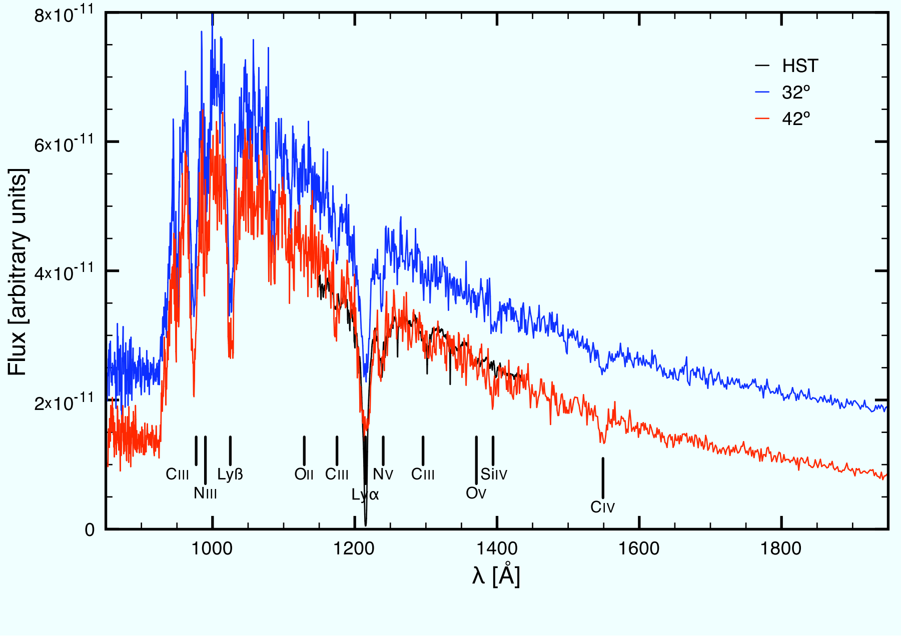

Figure 5.19: Calculated spectra for SS Cyg with $\dot{M} = 4.44 \cdot 10^{-10} \mathrm{M}_{\odot}/\mathrm{yr}$ and 20,000/40,000 K temperature structure. Shown are $i = 32^{\circ}$ (blue) and $i = 42^{\circ}$ (red), as well as a HST spectrum (black). For readability the upper spectrum was shifted upward by $1 \cdot 10^{-11}$. Note the Ly α line originating from the disk. The N V 1240 Å and the C IV 1550 Å lines are wind features.

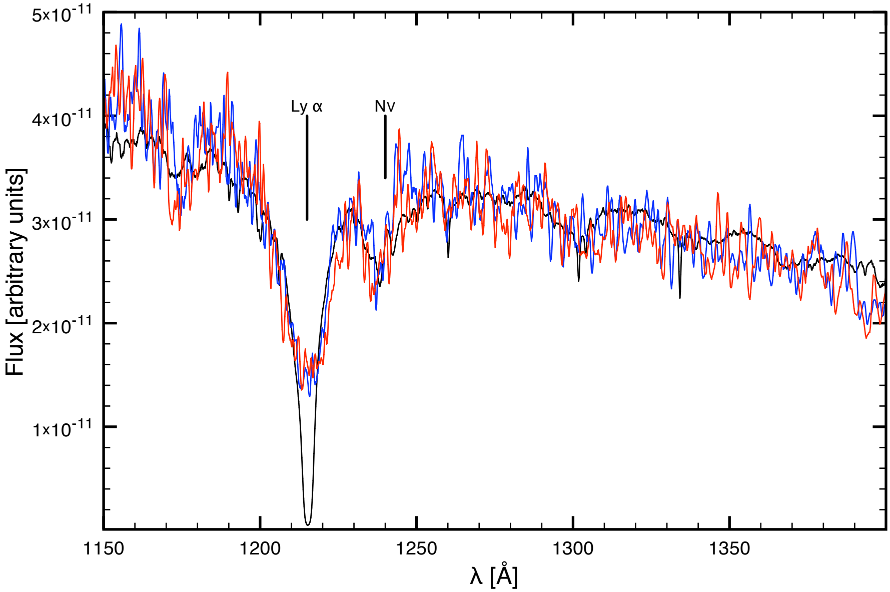

Figure 5.20: Observed HST spectrum (black), WOMPAT spectrum for $i = 32^\circ$ (blue) and $i = 42^\circ$ (red). Blow-up from Fig. 5.19 without the artificial shift.

5.4 Z Camelopardalis

Z Cam is the prototype for the class of dwarf novae showing a standstill, a halt in the normal decline after outburst about 1 mag below maximum light. In Z Cam these standstills can last from days to years. The system in the rather large but faint constellation camelopardalis (giraffe) is one of the brightest dwarf novae with $V = 10.5\mathrm{mag}$ in outburst and $14.8\mathrm{mag}$ in quiescence (Downes et al., 1997). It is very well observed and the basic system parameters were found to be $M_{\mathrm{WD}} = (0.99 \pm 0.15)\mathrm{M}_{\odot}$, $M_2 = (0.7 \pm 0.03)\mathrm{M}_{\odot}$, and an inclination $i = (57 \pm 11)^{\circ}$ (Ritter & Kolb, 1998). Hartley et al. (2005) find for a standstill situation an accretion rate of $\dot{M} = 1.1 \cdot 10^{-9}\mathrm{M}_{\odot}/\mathrm{yr}$ and a white dwarf temperature of 57,000 K. See Table 5.4 for a complete list of the parameters used for the Z Cam calculations. As elemental abundances we used the same solar values as for SS Cyg (Tab. 5.5). Contrary to the calculations for AM CVn and SS Cyg we use only a blackbody disk as a photon source and not accretion disk rings calculated with AcDc. Therefore all spectral features shown in this section are pure wind features.

As a comparison we use a low resolution IUE observation (swp35817) taken in march 1989 during a standstill obtained from MAST. This particular observation has not been used in a publication before, only the high resolution data from this campaign was used by Prinja & Rosen (1995). A first comparison of this observation with a WOMPAT spectrum calculated for 20,000 K constant wind temperature, for an inclination of 57° on a large 30 x 30 grid is shown in Fig. 5.21. The absorption lines or the absorption parts of the lines are stronger for the calculated spectrum than in the observation. Due to the low temperature in the wind the N V line is not present, but the observed C IV line at 1550 Å and the Si IV line at 1400 Å are quite prominent in the calculated model. Si IV is seen as a doublet in the observation, which we cannot resolve in the model as the line is only represented as a singlet in our frequency grid.

In Fig. 5.22 a close-up of the N V region around 1240 Å is shown for different inclination angles. All models were calculated for the 20,000/40,000 K temperature structure and clearly in all cases the computed line is not wide enough. For a mass-loss rate of $5.1 \cdot 10^{-10}\mathrm{M}_{\odot}/\mathrm{yr}$ an inclination angle of 57° seems most likely, there are however still other parameters like the temperature structure or the abundances which need to be considered before any valid conclusions can be drawn. A fourth panel in Fig. 5.22 shows the same inclination with a different mass-loss rate, where the line again is not wide enough to resemble the observation.

Table 5.6: WOMPAT parameter set for Z Cam with SV model.

Parameter	Value
$M_{\mathrm{WD}}(\mathrm{M}_{\odot})$	1.0
$R_{\mathrm{WD}}(\mathrm{cm})$	5.8×10^{8}
$T_{\mathrm{WD}}(\mathrm{K})$	$57,000$
$\dot{M}_{\mathrm{disk}}(\mathrm{M}_{\odot}\mathrm{yr}^{-1})$	1.1×10^{-9}
$r_{\mathrm{in}}(R_{\mathrm{WD}})$	21.1
$r_{\mathrm{out}}(R_{\mathrm{WD}})$	70
$\dot{M}_{\mathrm{wind}}(\mathrm{M}_{\odot}\mathrm{yr}^{-1})$	1.1×10^{-10}
$\theta_{\mathrm{min}}(\mathrm{deg})$	20
$\theta_{\mathrm{max}}(\mathrm{deg})$	65
$r_{\mathrm{min}}(R_{\mathrm{WD}})$	2.56
$r_{\mathrm{max}}(R_{\mathrm{WD}})$	20
$R_{v}(R_{\mathrm{WD}})$	100
$v_{\infty}(v_{\mathrm{esc}})$	3
α	1.5
λ	0

In Fig. 5.23 a close-up of the C IV region around 1550 Å is shown for different inclination angles, mass-loss rates and models. Clearly in all cases the computed line is too deep, which might have its origin in the mass-loss rate being to high or it might be due to the constant wind temperature at 20,000 K for which the calculations were performed. A different temperature structure with higher temperatures leads to C IV being less occupied and thus the line becomes weaker. We show only the limiting inclination angles of $46°$ and $68°$. Again the most probable inclination depends on the mass-loss rate. For $\dot{M}_{\mathrm{wind}} = 1.1 \cdot 10^{-10}\mathrm{M}_{\odot}/\mathrm{yr}$ an inclination of $68°$ seems closer to the observation, but for $\dot{M}_{\mathrm{wind}} = 5.1 \cdot 10^{-10}\mathrm{M}_{\odot}/\mathrm{yr}$ $46°$ seem more realistic. Without further parameter studies we cannot find any definite answers for neither the inclination nor the mass-loss rate. As a fourth panel in Fig. 5.23 a calculation for our newly developed hydrodynamical model is shown for the limiting inclination angles, the same constant temperature and a mass-loss rate of $5.1 \cdot 10^{-10}\mathrm{M}_{\odot}/\mathrm{yr}$. Comparing this profile to the profiles obtained with the SV

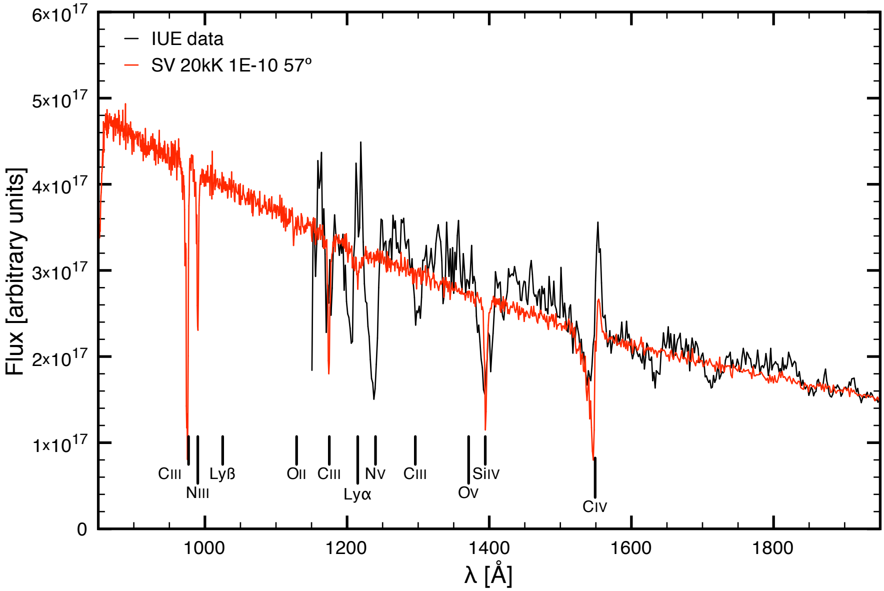

Figure 5.21: Observed IUE spectrum (black) and WOMPAT spectrum (red) for $i = 57°$ and a wind with $T = 20,000\mathrm{K}$. Note the C IV 1550 Å P Cygni profile and the strong Si IV 1400 Å line.

model we see that the absorption is much narrower and the emission part of the P Cygni profile is missing. These are similar findings as we obtained in Sec. 5.1.3 for the standard hydrodynamical model.

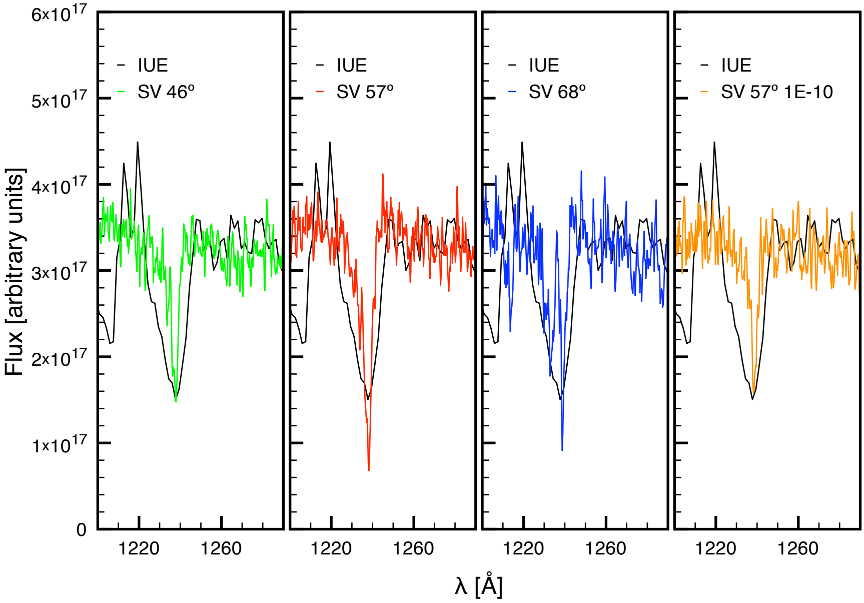

Figure 5.22: Observed IUE spectrum (black) and WOMPAT spectra for SV model and inclinations 46°, 57° and 68° for a mass-loss rate of $5.1 \cdot 10^{-10}\mathrm{M}_\odot/\mathrm{yr}$, as well as model for 57° with $\dot{M}_\mathrm{wind} = 1.1 \cdot 10^{-10}\mathrm{M}_\odot/\mathrm{yr}$. All for the 20,000/40,000 K temperature structure.

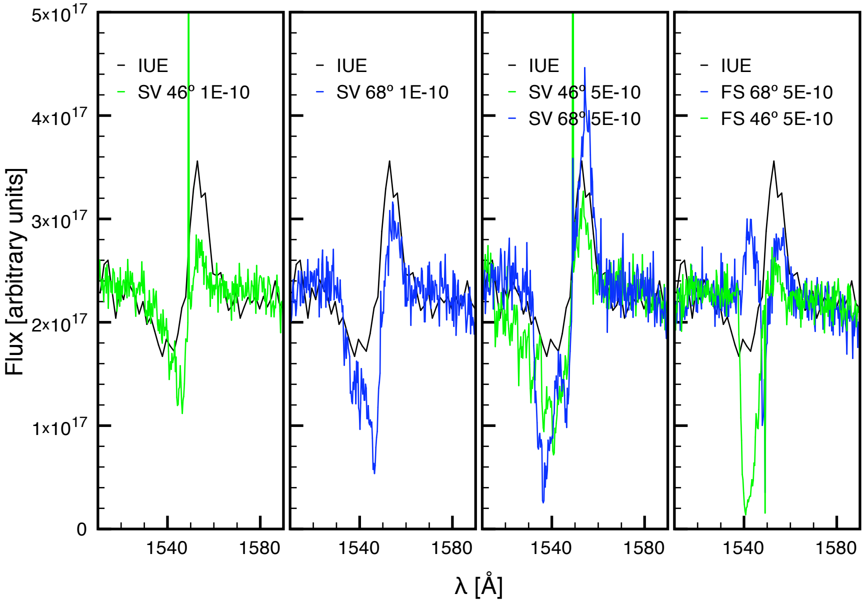

Figure 5.23: Observed IUE spectrum (black) and WOMPAT spectra for SV model and inclinations 46°, 57° and 68°, as well as hydro model for 57°. $\dot{M}_{\rm wind} = 1.1 \cdot 10^{-10} {\rm M}_\odot/{\rm yr}$ and $T_{\rm wind} = 20,000$ K.

CHAPTER 6

Conclusions

"There is a great satisfaction in building good tools for other people to use."

[Freeman Dyson]

We presented a fully 3-D radiative transfer code for accretion disk winds based on a Monte Carlo scheme. On top of the two kinematical models for accretion disk winds of cataclysmic variables already presented in the literature we developed a hydrodynamical model which can be used as a basis for the Monte Carlo radiative transfer. This model will be a good starting point for further, and more thorough, treatment of radiative transfer in the wind. A first application to a real system, Z Cam, was performed with this model, however a parameter study, which is needed to gain further understanding, was beyond the scope of this work. The second goal we achieved was to incorporate meaningful accretion disks calculated with AcDc as a photon source for the wind. For two real systems, the helium dwarf nova AM CVn and the dwarf nova SS Cyg we showed that the wind code is a necessary complement for understanding those systems needed on top of the accretion disk and vice versa. A third important finding was that the use of a realistic Stark broadening function instead of Doppler broadening leads to the necessity to adjust the mass-loss rates to higher values. But in order to gain more insight in this very interesting and important point more and deeper parameter studies are also necessary.

For the helium dwarf nova AM CVn no studies of mass-loss via accretion disk wind were performed so far. Within our standard calculations for this system and comparison to available STIS spectra we can conclude that a mass-loss rate higher than $1 \cdot 10^{-9} \mathrm{M}_\odot/\mathrm{yr}$, even as high as $5 \cdot 10^{-9} \mathrm{M}_\odot/\mathrm{yr}$ is probable. This might change however if more calculations, which take Stark broadening and the hydrodynamical model into account, are available. No stronger constraints on the inclination angle of the system are possible with our data at the moment. The studies on AM CVn and SS Cyg show that there is no principal difference in the outflow from a helium and a "normal" hydrogen accretion disk. For SS Cyg our limited exploration of the parameter space does not allow us to determine the inclination or the mass-loss rate any clearer than already known, although an inclination close to 32° seems most likely for a mass-loss rate of $\dot{M} = 4.44 \cdot 10^{-10}\mathrm{M}_\odot/\mathrm{yr}$. But this will be changed with a future larger exploration of the parameter space. The combination of accretion disk model and wind model does, however, resemble the Ly α line quite well, except for the interstellar component. An exploration of the parameter space is also needed for the third system we considered in this work, Z Cam. Considerations of the N V line and a wind with 20,000/40,000 K temperature structure lead to inconclusive results with a mass-loss rate of $5.1 \cdot 10^{-10}\mathrm{M}_\odot/\mathrm{yr}$ an inclination angle of 57° seems most likely. However, if the 1550 Å C IV line is considered mass-loss rates of $1.1 \cdot 10^{-10}\mathrm{M}_\odot/\mathrm{yr}$ with an inclination of 68° might almost be as possible as a mass-loss rate of $5.1 \cdot 10^{-10}\mathrm{M}_\odot/\mathrm{yr}$ with an inclination of 46°.

A word of warning on fitting time resolved spectra with P Cygni profiles with a stationary radiative transfer code as WOMPAT is. It has been shown (e.g. by Prinja et al. 2003, 2004) that those profiles are modulated with the orbital period, but they also change on faster timescales which could be due to some kind of clumping in the wind. Therefore any fit to a time resolved spectrum is going to yield time resolved results, only from averaged spectra the averaged parameters of the system can be extracted. An ultimate goal should be to provide time resolved models which include clumping.

One interesting point to mention is that the average number of scattering processes a photon encounters on its way through the accretion disk wind is of the order of 1, of course dependent on the wind density but in none of our calculations the number was very far of the 1. This is from the CAK side of wind theory expected and a nice point that our hydrodynamical ansatz is not too far off. The hydrodynamical model is going to be expanded beyond the standard model in order to make realistic calculations and comparisons to observations possible.

APPENDIX A

Constants and other mathematical symbols used

As it is common in astronomy all values are in *cgs* units. Wavelengths are given in Å, where 1 Å $= 0.1\,\mathrm{nm}$.

AU	Astronomical Unit, distance sun - earth	$1.495 \cdot 10^{13}\mathrm{cm}$
G	gravitational constant	$6.6726 \cdot 10^{-8}\mathrm{cm}^3\,\mathrm{g}^{-1}\,\mathrm{s}^{-2}$
h	Planck constant	$6.625 \cdot 10^{-27}\mathrm{erg\,s}$
k	Boltzmann constant	$1.38 \cdot 10^{-16}\mathrm{erg/K}$
$\mathrm{L}_\odot$	Solar luminosity	$3.827 \cdot 10^{33}\mathrm{erg/s}$
$\mathrm{M}_\odot$	Solar mass	$1.989 \cdot 10^{33}\mathrm{g}$
$\mathrm{R}_\odot$	Solar radius	$6.960 \cdot 10^{10}\mathrm{cm}$

$\vec{F}_\nu$	astrophysical flux
$\vec{\mathcal{F}}_\nu$	radiation flux
$\vec{H}_\nu$	Eddington flux
κ	opacity
L_1	inner Lagrange point
P_{orb}	orbital period
r_{disk}	radius of accretion disk
τ	optical depth
v_{D}	Doppler velocity
v_∞	terminal wind velocity
v_{th}	velocity due to thermal motion

APPENDIX B

Abbreviations used

ACDC	Accretion Disk code
AGN	Active Galactic Nuclei
ASCA	Advanced Satellite for Cosmology and Astrophysics
CV	Cataclysmic Variable
DIM	Disk Instability Model
DN	Dwarf Nova
FS	Feldmeier & Shlosman
FSc	Forced Scattering algorithm
HUT	Hopkins Ultraviolet Telescope
HST	Hubble Space Telescope
IUE	International Ultraviolet Explorer
KWD	Knigge, Woods & Drew
LOD	Live Or Die algorithm
LOF	Line Of Flight
LOS	Line Of Sight
LTE	Local Thermodynamical Equilibrium
MC	Monte Carlo
MHD	Magneto-Hydro Dynamics
MPI	Message Passing Interface
MRI	Magneto-Rotational Instability
MTI	Mass Transfer Instability
NLTE	Non-Local Thermodynamical Equilibrium
SA	Sobolev Approximation
SHS disk	Shakura-Sunyaev disk
STIS	Space Telescope Imaging Spectrograph
SV	Shlosman & Vitello
UV	ultraviolet
WOMPAT	Wind mOdel in Monte carlo Parallel rAdiative Transfer
YSO	Young Stellar Object

List of Figures

1.1 HST images of Herbig-Haro objects 2
1.2 HST image with bipolar outflow 3
1.3 M87 jet 4
2.1 Mean lightcurve of Z Cha in quiescence 9
2.2 Decomposition of Z Cha mean lightcurve 10
2.3 Roche potential 12
2.4 Roche lobe mass flow cartoon 13
2.5 Disk formation schematics 16
2.6 Annotated artwork of SS Cyg 17
2.7 Polar schematic 20
2.8 Intermediate Polar schematic 21
2.9 Orbital period distribution 23
3.1 Spectral evolution of SS Cyg 37
3.2 Double peaked line from disk 38
3.3 Observed Z Cha Hα line 38
3.4 Lightcurves of Z Cam and SU UMa 40
3.5 Lightcurve of U Gem 41
3.6 Eclipse profiles of OY Car from quiescence to outburst . . . 42
3.7 $\Sigma - T_{\rm eff}$ relation 44
3.8 $\Sigma(r)$ time evolution 47
3.9 P Cygni profile formation 49
3.10 C IV as P Cygni in T Leo 50
3.11 HUT spectrum of IX Vel & Z Cam 51
3.12 Solution topology of CAK critical point 59
3.13 $\mathrm{d}\dot{M}$ per disk annulus 61
4.1 Schematic of radiation field 65
4.2 Sketch of SV wind model 73
4.3 Sketch of KWD wind model 76
4.4 Geometric parameters of KWD 77
4.5 Wind geometry of hydrodynamical wind 81
4.6 WOMPAT Code flowchart 94

4.7 RingRot vs WOMPAT blackbody disk 95
4.8 Monte Carlo photons from ACDC disk 96
4.9 Comparison of C IV in SV WOMPAT vs Python 97
4.10 Comparison of C IV in KWD WOMPAT vs Python 98
4.11 SV temperature structure WOMPAT vs Python 99
4.12 Ad hoc temperature structure 100
5.1 Density in SV wind 103
5.2 Density in hydro wind 103
5.3 Density in KWD wind 104
5.4 SV with $T_{\rm wind} = 20,000\,{\rm K}$ 106
5.5 SV with $T_{\rm wind} = 40,000\,{\rm K}$ 106
5.6 SV with temperature structure 107
5.7 SV with temperature iterated 108
5.8 SV comparison large and small domain 109
5.9 SV comparison of Doppler and Stark 110
5.10 Hydro with $T_{\rm wind} = 20,000\,{\rm K}$ 111
5.11 Hydro with $T_{\rm wind} = 40,000\,{\rm K}$ 112
5.12 Hydro with temperature structure 113
5.13 Hydro with temperature iterated 113
5.14 Box number comparison 114
5.15 Hydro comparison of Doppler and Stark 115
5.16 AM CVn comparison with observation 118
5.17 AM CVn N V comparison 39° 119
5.18 AM CVn N V comparison 60° 120
5.19 SS Cyg calculated spectra 123
5.20 SS Cyg N V comparison with observation 124
5.21 Z Cam comparison with observation 127
5.22 Z Cam comparison with observation in N V 128
5.23 Z Cam comparison with observation in C IV 129

List of Tables

4.1 Standard parameter set for SV model 75
4.2 Standard parameter set for KWD model 80
4.3 Standard parameter set for hydro wind model 83
5.1 Abundances for standard models 102
5.2 Parameter set for AM CVn 117
5.3 Abundances for AM CVn 117
5.4 Parameter set for SS Cyg 121
5.5 Abundances for SS Cyg & Z Cam 122
5.6 Parameter set for Z Cam 126

Bibliography

Abbott, D. C. 1980, ApJ, 242, 1183 [ADS]

American Association of Variable Star Observers (AAVSO). 2007, www.AAVSO.org [LINK]

Balbus, S. A. & Hawley, J. F. 1991, ApJ, 376, 214 [ADS]

—. 1998, Reviews of Modern Physics, 70, 1 [ADS]

Baskill, D. S., Wheatley, P. J., & Osborne, J. P. 2001, MNRAS, 328, 71 [ADS]

Bath, G. T. 1975, MNRAS, 171, 311 [ADS]

Belle, K., Nguyen, Q., Fabian, D., Sion, E. M., & Huang, M. 1998, PASP, 110, 47 [ADS]

Cashwell, E. D. & Everett, C. J. 1959, A principal manual on the Monte Carlo method for random walk problems (Pergamon)

Cassinelli, J. P. 1979, ARA&A, 17, 275 [ADS]

Castor, J. I., Abbott, D. C., & Klein, R. I. 1975, ApJ, 195, 157 [ADS]

Castor, J. I. & Lamers, H. J. G. L. M. 1979, ApJS, 39, 481 [ADS]

Chandrasekhar, S. 1960, Radiative transfer (New York: Dover, 1960)

Cordova, F. A. & Mason, K. O. 1982, ApJ, 260, 716 [ADS]

Dhillon, V. S. & Rutten, R. G. M. 1995, MNRAS, 277, 777 [ADS]

Diaz, M. P., Wade, R. A., & Hubeny, I. 1996, ApJ, 459, 236 [ADS]

Downes, R., Webbink, R. F., & Shara, M. M. 1997, PASP, 109, 345

Drew, J. & Verbunt, F. 1985, MNRAS, 213, 191 [ADS]

Drew, J. E. 1987, MNRAS, 224, 595 [ADS]

Ercolano, B., Barlow, M. J., Storey, P. J., & Liu, X.-W. 2003, MNRAS, 340, 1136 [ADS]

Feldmeier, A. & Shlosman, I. 1999, ApJ, 526, 344 [ADS]

Feldmeier, A., Shlosman, I., & Vitello, P. 1999, ApJ, 526, 357 [ADS]

Frank, J., King, A. R., & Raine, D. J. 1985, Accretion power in astrophysics (Cambridge and New York, Cambridge University Press, 1985) [ADS]

Giovannelli, F. & Martinez-Pais, I. G. 1991, Space Science Reviews, 56, 313 [ADS]

Gräfener, G. 2007, priv. comm.

Gräfener, G. & Hamann, W.-R. 2005, A&A, 432, 633 [ADS]

Hammer, N. J. 2004, diploma thesis, University of Tübingen

Hartley, L. E., Long, K. S., Froning, C. S., & Drew, J. E. 2005, ApJ, 623, 425 [ADS]

Harvey, D. A., Skillman, D. R., Kemp, J., Patterson, J., Vanmunster, T., Fried, R. E., & Retter, A. 1998, ApJ, 493, L105+ [ADS]

Heap, S. R., Boggess, A., Holm, A., Klinglesmith, D. A., Sparks, W., West, D., Wu, C. C., Boksenberg, A., Willis, A., Wilson, R., Macchetto, F., Selvelli, P. O., Stickland, D., Greenstein, J. L., Hutchings, J. B., Underhill, A. B., Viotti, R., & Whelan, J. A. J. 1978, Nature, 275, 385 [ADS]

Hellier, C. 2001, Cataclysmic variable stars - How and why they vary (Springer Praxis)

Hessman, F. V., Robinson, E. L., Nather, R. E., & Zhang, E.-H. 1984, ApJ, 286, 747 [ADS]

Hillier, D. J., Lanz, T., Heap, S. R., Hubeny, I., Smith, L. J., Evans, C. J., Lennon, D. J., & Bouret, J. C. 2003, ApJ, 588, 1039 [ADS]

Hils, D. & Bender, P. L. 2000, ApJ, 537, 334 [ADS]

Honeycutt, R. K., Schlegel, E. M., & Kaitchuck, R. H. 1986, ApJ, 302, 388 [ADS]

Horne, K. & Marsh, T. R. 1986, MNRAS, 218, 761 [ADS]

Hubeny, I. 2003, in Astronomical Society of the Pacific Conference Series, Vol. 288, Stellar Atmosphere Modeling, ed. I. Hubeny; D. Mihalas & K. Werner, 17 [ADS]

Knigge, C., Long, K. S., Blair, W. P., & Wade, R. A. 1997, ApJ, 476, 291 [ADS]

Knigge, C., Woods, J. A., & Drew, E. 1995, MNRAS, 273, 225 [ADS]

Kromer, M., Nagel, T., & Werner, K. 2007, A&A, 475, 301 [ADS]

Kube, J. 2002, PhD thesis, University of Göttingen [LINK]

Kurosawa, R. & Hillier, D. J. 2001, A&A, 379, 336 [ADS]

Lamers, H. J. G. L. M. & Morton, D. C. 1976, ApJS, 32, 715 [ADS]

Landau, L. D. & Lifshitz, E. M. 1959, Fluid mechanics (Course of theoretical physics, Oxford: Pergamon Press, 1959) [ADS]

Langfeld, K. 2007, ArXiv e-prints, 711 [ADS]

Long, K. S. & Knigge, C. 2002, ApJ, 579, 725 [ADS]

Long, K. S., Mauche, C. W., Raymond, J. C., Szkody, P., & Mattei, J. A. 1996, ApJ, 469, 841 [ADS]

Long, K. S., Wade, R. A., Blair, W. P., Davidsen, A. F., & Hubeny, I. 1994, ApJ, 426, 704 [ADS]

Lucy, L. B. 1999a, A&A, 344, 282 [ADS]

—. 1999b, A&A, 345, 211 [ADS]

Marchuk, G. I., Mikhailov, G. A., & Nazaraliev, M. A. 1980, The Monte Carlo methods in atmospheric optics (Springer Series in Optical Sciences, Berlin: Springer, 1980) [ADS]

Mauche, C. W. & Raymond, J. C. 1987, ApJ, 323, 690 [ADS]

Mazzali, P. A. & Lucy, L. B. 1993, A&A, 279, 447 [ADS]

Metropolis, N. 1985, in Lecture Notes in Physics, Berlin Springer Verlag, Vol. 240, Monte-Carlo Methods and Applications in Neutronics, Photonics, and Statistical Physics, eds. Alcouffe, R.; Dautray, R.; Forster, A.; Ledonois, G.; & Mercier, B., 62

Metropolis, N. & Ulam, S. 1949, Journal of the American Statistical Association, 44, 335

Meyer, F. & Meyer-Hofmeister, E. 1981, A&A, 104, L10+ [ADS]

Mihalas, D. 1978, Stellar atmospheres 2nd edition (San Francisco, W. H. Freeman and Co., 1978.) [ADS]

Mineshige, S. & Osaki, Y. 1985, PASJ, 37, 1 [ADS]

Murray, N. & Chiang, J. 1996, Nature, 382, 789 [ADS]

Nagel, T., Dreizler, S., Rauch, T., & Werner, K. 2004, A&A, 428, 109 [ADS]

Nelemans, G. 2005, in Astronomical Society of the Pacific Conference Series, Vol. 330, The Astrophysics of Cataclysmic Variables and Related Objects, eds. J.-M. Hameury and J.-P. Lasota, 27 [ADS]

Niccolini, G., Woitke, P., & Lopez, B. 2003, A&A, 399, 703 [ADS]

Olson, G. L. & Kunasz, P. B. 1987, Journal of Quantitative Spectroscopy and Radiative Transfer, 38, 325 [ADS]

Osaki, Y. 1974, PASJ, 26, 429 [ADS]

Parker, E. N. 1958, ApJ, 128, 664 [ADS]

—. 1960, ApJ, 132, 821 [ADS]

Pereyra, N. A., Kallman, T. R., & Blondin, J. M. 1997, ApJ, 477, 368 [ADS]

Prendergast, K. H. 1960, ApJ, 132, 162 [ADS]

Pringle, J. E. 1981, ARA&A, 19, 137 [ADS]

Prinja, R. K., Knigge, C., Witherick, D. K., Long, K. S., & Brammer, G. 2004, MNRAS, 355, 137 [ADS]

Prinja, R. K., Long, K. S., Froning, C. S., Knigge, C., Witherick, D. K., Clark, J. S., & Ringwald, F. A. 2003, MNRAS, 340, 551 [ADS]

Prinja, R. K. & Rosen, R. 1995, MNRAS, 273, 461 [ADS]

Proga, D., Kallman, T. R., Drew, J. E., & Hartley, L. E. 2002, ApJ, 572, 382 [ADS]

Proga, D., Stone, J. M., & Drew, J. E. 1998, MNRAS, 295, 595 [ADS]

—. 1999, MNRAS, 310, 476 [ADS]

Puls, J., Kudritzki, R.-P., Herrero, A., Pauldrach, A. W. A., Haser, S. M., Lennon, D. J., Gabler, R., Voels, S. A., Vilchez, J. M., Wachter, S., & Feldmeier, A. 1996, A&A, 305, 171 [ADS]

Rauch, T. & Deetjen, J. L. 2003, in Astronomical Society of the Pacific Conference Series, Vol. 288, Stellar Atmosphere Modeling, ed. I. Hubeny; D. Mihalas & K. Werner, 103 [ADS]

Ringwald, F. A. & Naylor, T. 1998, AJ, 115, 286 [ADS]

Ritter, H. & Kolb, U. 1998, A&AS, 129, 83 [ADS]

Roelofs, G. H. A., Groot, P. J., Benedict, G. F., McArthur, B. E., Steeghs, D., Morales-Rueda, L., Marsh, T. R., & Nelemans, G. 2007, ApJ, 666, 1174 [ADS]

Rutten, R. G. M., Kuulkers, E., Vogt, N., & van Paradijs, J. 1992, A&A, 265, 159 [ADS]

Rybicki, G. B. & Hummer, D. G. 1978, ApJ, 219, 654 [ADS]

—. 1983, ApJ, 274, 380 [ADS]

Shakura, N. I. & Sunyaev, R. A. 1973, A&A, 24, 337 [ADS]

Shlosman, I. & Vitello, P. 1993, ApJ, 409, 372 [ADS]

Sim, S. A. 2007a, MNRAS, 375, 154 [ADS]

—. 2007b, priv. comm.: Python results for KWD and SV models

Smak, J. 1984, PASP, 96, 5 [ADS]

Smak, J. in , Lecture Notes in Physics, Berlin Springer Verlag, Vol. 563, Binary Stars: Selected Topics on Observations and Physical Processes, ed. F. C. LázaroM. J. Arévalo, 110–150 [ADS]

Sobolev, V. V. 1960, Moving envelopes of stars (Cambridge: Harvard University Press, 1960)

Stern, B. E., Begelman, M. C., Sikora, M., & Svensson, R. 1995, MNRAS, 272, 291 [ADS]

Tenzer, C., Kendziorra, E., Santangelo, A., Kuster, M., Ferrando, P., Laurent, P., Claret, A., & Chipaux, R. 2006, in SPIE Conference, Vol. 6266, Space Telescopes and Instrumentation II: Ultraviolet to Gamma Ray. Edited by Turner, Martin J. L.; Hasinger, Günther. Proceedings of the SPIE, Volume 6266, pp. 62662O (2006). [ADS]

Verbunt, F. 1982, Space Science Reviews, 32, 379 [ADS]

Vitello, P. A. J. & Shlosman, I. 1988, ApJ, 327, 680 [ADS]

Wade, R. A., Eracleous, M., & Flohic, H. M. L. G. 2007, AJ, 134, 1740 [ADS]

Warner, B. 1995, Cataclysmic variable stars (Cambridge Astrophysics Series, Cambridge, New York: Cambridge University Press, |c1995) [ADS]

Werner, K., Deetjen, J. L., Dreizler, S., Nagel, T., Rauch, T., & Schuh, S. L. 2003, in Astronomical Society of the Pacific Conference Series, Vol. 288, Stellar Atmosphere Modeling, ed. I. Hubeny; D. Mihalas & K. Werner, 31 [ADS]

Werner, K., Nagel, T., Rauch, T., Hammer, N. J., & Dreizler, S. 2006, A&A, 450, 725 [ADS]

Wichmann, B. & Hill, I. 1982, Appl. Statist., 31, 188

Witt, A. N. 1977, ApJS, 35, 1 [ADS]

Wolf, S., Henning, T., & Stecklum, B. 1999, A&A, 349, 839 [ADS]

Wood, J., Horne, K., Berriman, G., Wade, R., O'Donoghue, D., & Warner, B. 1986, MNRAS, 219, 629 [ADS]

Index

Abbott wave, 55
accretion column, 18
accretion disk
    temperature, 32
    vertical structure, 32
accretion rate, 14
accretion shock, 18
active galactic nuclei, 1
α
    disk, 33–35
    parametrisation, 33
AM CVn, 25–26, 116
AM Her, *see* polar
AR UMa, 19

binary
    contact, 12
    detached, 12
    semi-detached, 12
Boltzmann equation, 68
boundary layer, 17, 31
bright spot, 11

cataclysmic variable, 6–11
    evolution, 22
    magnetic, 18–22
Chandrasekhar limit, 7
circularisation radius, 14, 15
classical nova, 7
common-envelope phase, 22
common-envelope system, 13
critical point, 57
    CAK condition, 58

disk instability model, 41
DQ Her, *see* intermediate polar
dwarf nova, 7, 37
    outburst cycle, 45

emissivity, 67
energy density, 66
energy weight, *see* Monte Carlo, weight
Euler equation, 29, 54

flux
    astrophysical, 65
    Eddington, 65
FS model, *see* model,hydro

gravitational wave emission, 24
gravitational well, 12

Herbig-Haro object, 2
hot spot, *see* bright spot
hydro model, *see* model,hydro

intensity
    moments of, 64
    specific, 64
intermediate polar, 19
IX Vel, 50

Kepler's law, 8

KWD model, *see* model,KWD

Lagrange point, 11
limb darkening, 87
limit cycle, 45
line driving, 52
line force, 52
LTE, 69

magnetic breaking, 23
magneto-rotational instability, 34, 43
Markov chain, 86
mass transfer instability, 43
Messier 87, 3
model
    hydro, 81–82, 111
    KWD, 76–80, 114
    SV, 71–75, 105
Monte Carlo
    estimator, 92
    weight, 85

NN Ser, 12
non-LTE, 69
nova, 7
    classical, *see* classical nova
    dwarf, *see* dwarf nova
    recurrent, *see* recurrent nova
nova-like, 7
nozzle analogy, 55
nozzle function, 56–58

occupation number, 68
opacity, 67
orbital hump, 11
OY Car, 39

P Cygni profile, 48
period gap, 24
photon packet, 86
polar, 19
primary, 6
probability distribution, 84

radial drift timescale
    see viscous timescale, 31
recurrent nova, 7
red dwarf, 6, 10
rejection method, 85
resonance layer, 54
Roche lobe, 11
RXJ0806, 26

Saha equation, 68
secondary, 6
SHS disk, *see* α disk
Sobolev approximation, 69
Sobolev optical depth, 54
Sobolev zone, *see* resonance layer
SS Cyg, 36, 39, 121
standstill, 39, 125
SU UMa, 39
supernova progenitor, 8
supernova, type Ia, 7
surface density, 30
SV model, *see* model,SV

T Leo, 49
table-look up, 85
tidal radius, 14, 15
transition
    bound-bound, 67
    bound-free, 67
    free-free, 67

U Gem, 39

viscosity, 33
viscous timescale, 31

W UMa, 12
white dwarf, 6, 9

young stellar object, 1

Z Cam, 39, 50, 125
Z Cha, 8, 36

Acknowledgements

“Live as if you were to die tomorrow. Learn as if you were to live forever.”

[Mahatma Gandhi]

First of all, I’d like to thank my advisor Prof. Dr. Klaus Werner for providing me with the interesting and challenging topic of expanding the accretion disk-stellar atmosphere package to a third dimension, and being there with help, support and advise when needed. This work would not have been possible without the ever inspiring mentoring of Dr. Thorsten Nagel, his knowledge about accretion disks and long discussions with him about astronomical problems. Thank you, too, for the great time at the telescopes, whether it was CAHA or Tübingen. I’m also in great dept to Prof. Dr. Achim Feldmeier for the excellent cooperation in developing the hydro parts of this work and his help in obtaining a DFG grant for this work.

The time at the IAAT was a great one and I’d like to thank all members of the institute for that, but especially the Journal Club and Espresso gangs. Amongst others Michael for always being a helpful friend, Elke for proof-reading this work, Thorsten, Markus and Jens for being excellent office mates. And our stellar atmospheres working group, Klaus, Thomas, Thorsten, Valery, Jens, and Mark, for all the helpful discussions.

Stuart Sim I’d like to thank for answering the even most stupid questions about accretion disk winds and for providing me with comparison results from Python calculations.

Prof. Dr. Jörn Wilms for astronomical enthusiasm, which was one reason came to the “astro”, and for his help with random procedures and Monte Carlo, especially at the beginning of my work.

My visits in Potsdam were always inspiring and of great value for this work. I'd like to thank everyone who made this possible and everyone in the group of Prof. Dr. Wolf-Rainer Hamann and Prof. Dr. Achim Feldmeier for the warm welcome.

Much credit goes to the ZDV of the University of Tübingen for the access to both high-performance clusters and the, not always trouble-free, parallel-computer time provided. This work was supported by the DFG under grant We 1312/37-1.

Last but not least a "thank you" I cannot really put in words to my parents for their love and support throughout my life and especially during my studies. And of course a "thank you" that is as unspeakable to my wife Katrin for all her love and patience towards the "crazy astrophysicist", life with you is never boring.

Curriculum vitae

	30.01.1977	geboren in Stuttgart
Schule	1983-1987	Grundschule Stuttgart
	1987-1996	Leibniz-Gymnasium Stuttgart
	06.1996	Abitur
Zivildienst	09.1996-09.1997	Arbeiterwohlfahrt Stuttgart
Studium	10.1997-03.2004	Studium der Physik an der Eberhard-Karls-Universität Tübingen
	02.2001-12.2001	Projektarbeit und Studium der Physik an der University of Adelaide, Adelaide, Australien
	10.1996	Vordiplom, Nebenfach Chemie
		Diplomarbeit “Quarkproperties, Topology und Confinement from Lattice Gauge Theory” an der Universität Tübingen, Institut für Theoretische Physik unter der Anleitung von PD. Dr. K. Langfeld
	03.2004	Diplom, Wahlfach Astronomie und Astrophysik
	04.2004-02.2008	Anfertigung der Dissertation mit dem Titel “Monte Carlo Radiative Transfer in Accretion Disk Winds of Cataclysmic Variable Stars” an der Universität Tübingen, Institut für Astronomie und Astrophysik (IAA), Abt. Astronomie, unter Anleitung von Prof. Dr. K. Werner
Beruf	09.1999-12.2000	Systemadministrator, Tierphysiologie, Universität Tübingen
	04.2004-	wissenschaftlicher Angestellter am IAA Tübingen

Meine akademischen Lehrer waren die Professoren und Dozenten Dres.:
Angewandte Physik: O. Eibl, F. Hasselbach, D. Kern, E. Plies
Astronomie und Astrophysik: S. Dreizler, E. Haug, E. Kendziorra, W. Kley, H. Ruder, R. Staubert, K. Werner
Experimentalphysik: H. Clement, F. Gönnenwein, P. Grabmayr, W. Hartmann, R. Kleiner, O. Lutz, A. Schwenk, G. Wagner, C. Zimmermann
Chemie: J. Strähle
Mathematik: H. Fischer, H. Kaul, M. Wolff
Theoretische Physik: R. Alkofer, K. Langfeld, D. Leinweber, H. Müther, H. Pfister, H. Reinhardt, A. Williams